Miniaturized Antenna and Wave Propagation Studies Enabling Compact Low-Power Mobile Radio Networks at Low VHF

by

Jihun Choi

A dissertation submitted in partial fulfillment
of the requirements for the degree of
Doctor of Philosophy
(Electrical and Computer Engineering)
in The University of Michigan
2017

Doctoral Committee:

Professor Kamal Sarabandi, Chair
Professor Anthony Grbic
Professor Eric Michielssen
Professor Christopher S. Ruf

Jihun Choi

jihchoi@umich.edu

ORCID iD: 0000-0002-9105-9328

This dissertation is dedicated to my family and friends.

ACKNOWLEDGMENTS

It would not have been possible to complete this work without the help and support of the considerate people around me, to only some of whom it is possible to give particular mention here.

I would first like to sincerely thank my advisor, Prof. Kamal Sarabandi who has supported me throughout this dissertation with his guidance and encouragement. His persistence and enthusiasm for scientific research serve as a deep source of inspiration in my PhD life.

I would also like to take this opportunity to thank Prof. Anthony Grbic, Prof. Eric Michielssen, and Prof. Christopher S. Ruf for their support and advice while serving as my dissertation committee members. Special thanks are given to Dr. Brian M. Sadler and Dr. Fikadu T. Dagefu at the U.S. Army Research Laboratory for their collaboration and suggestions.

I would like to extend my gratitude to the former and current members of the Radiation Laboratory and all the other friends I have made at the University of Michigan for their constructive discussions and friendship. I thank Dr. Adib Nashashibi, Dr. Leland Pierce, Dr. Jungsuek Oh, Dr. Young Jun Song, Dr. Meysam Moallem, Dr. Sangjo Choi, Dr. Hamid Nejati, Dr. Jiangfeng Wu, Dr. Hatim Bukhari, Dr. Seungku Lee, Dr. Taehee Jang, Dr. Victor Lee, Dr. Seyit Sis, Dr. Gurkan Gok, Dr. Waleed Alomar, Dr. Yang Liu, Dr. Xiaoyu Wang, Dr. Brian Tierney, Dr. Inyong Kwon, Michael Benson, Mani Kashanianfard, Armin Jam, Amr Ibrahim, Morteza Sheikhsofla, Xiuzhang Cai, Seyed Amjadi, Behzad Yektakhah, Mostafa Zaky, Navid Barani, Michael Giallorenzo, Abdulrahman Alaqeel, Lisa Smith, Milad Zolfagharloo Koohi, Omar

Abdelatty, Fatemeh Akbar, Amanda Couch, Maryam Salim, Doowhan Jung, Hyeongseok Kim, Sunmin Jang, and Eunseong Moon.

I would like to acknowledge the financial support that I have received from the U.S. Army Research Laboratory through collaborative participation in the Microelectronics Center of Micro Autonomous Systems and Technology (MAST) Collaborative Technology Alliance (CTA), National Science Foundation (NSF), Saudi Aramco, and Oak Ridge Associated Universities (ORAU), which made my PhD experience productive and stimulating.

Lastly, and most importantly, I place on record, my sincere gratitude and appreciation to my family for their unconditional love, unceasing encouragement, and endless supports, all of which are always the central driving force of my life. To them, I dedicate this dissertation.

Jihun
Winter, 2017,
Ann Arbor.

TABLE OF CONTENTS

LIST OF FIGURES

Figure

LIST OF TABLES

Table

LIST OF APPENDICES

Appendix

ABSTRACT

Miniaturized Antenna and Wave Propagation Studies Enabling Compact Low-Power Mobile Radio Networks at Low VHF

by

Jihun Choi

Chair: Kamal Sarabandi

Reliable tactical mobile networking in cluttered infrastructure-poor environments at conventional microwave frequencies is a very challenging task, which requires innovative and unconventional networking capabilities, due to very high signal attenuation and small-scale fading. At lower frequencies, such effects are significantly reduced, which makes these frequencies more appropriate for robust moderate-rate communication over longer ranges with low transmit power. However, the prohibitively large size of conventional antennas and lack of efficient small antennas have been a major bottleneck in realizing compact systems for applications such as autonomous networking among small robotic platforms.

To enable compact, low-power, low frequency wireless mobile systems, empirical studies are first conducted to investigate the propagation characteristics of the low frequency channel among near-ground nodes. From rigorous studies via physics-based simulation and extensive

measurements in complex environments such as non-line-of-sight (NLOS) indoor and outdoor settings, the lower-VHF band (30 MHz – 60 MHz) is chosen due to its favorable propagation properties (high signal penetration through multiple layers of walls and very low signal and phase distortion and delay spread) compared to higher frequency bands (e.g., upper VHF and UHF bands).

The second key aspect of this thesis is the design of miniaturized antennas that enable the realization of compact low-VHF communication systems for mobile networking applications. Also, methods for its bandwidth enhancement and performance characterization are examined. A highly miniaturized ($0.013\lambda_0$ in lateral dimension and $0.02\lambda_0$ in height at 40 MHz) and lightweight (98 grams) antenna is designed. The antenna provides an impedance bandwidth of 0.35 % and a vertically polarized omnidirectional pattern with the maximum gain of -13 dBi, which is more than 10 dB higher than state-of-the-art antennas with comparable size. In order to further enhance its bandwidth, a new design approach for a non-Foster matching technique utilizing a negative impedance converter is presented. This approach enhances 3 dB power bandwidth with a power efficiency advantage more than twofold compared to that of the passive one. Furthermore, a very effective characterization method for low frequency antennas is developed. This method comprises two procedures: 1) non-intrusive very-near-field measurements using an electro-optical system dispensing with costly large anechoic chambers, and 2) near-field to far-field transformation to compute a far-field radiation based on the reciprocity theorem and full-wave numerical simulations.

In the third part of this thesis, a compact, low-power, low-VHF radio employing off-the-shelf ZigBee technology and an optimally designed bi-directional frequency converter (UHF ↔ low VHF) is introduced, in conjunction with the antenna described above, to investigate performance of such systems. The experimental studies show a highly reliable mobile ad-hoc

network with a radio coverage of more than 280 m at low power (< 10 mW) in complex propagation scenarios. This work also facilitates multi-node mobile networking at low VHF applied to networking of autonomous vehicles carrying out collaborative tasks such as autonomous exploration and mapping.

CHAPTER I
Introduction

1.1 Motivation

Establishing reliable mobile ad-hoc networks with wireless devices operating at conventional microwave frequency bands (e.g., Wi-Fi and cellular frequency bands) is very challenging due to high signal attenuation and fading, caused by a multitude of scatterers that exist in complex propagation scenarios such as indoor and urban settings, as well as signal interference generated by neighboring devices [1]-[4]. As a remedy to such complexities, various networking methodologies have been developed over the past few decades. For instance, cooperative multi-hop routing enables reliable extended signal coverage by relaying transmission information via multiple nodes in an ad-hoc network [5]. Multi-input and multi-output (MIMO) techniques using multiple transmit and receive antennas increase link reliability and range by taking advantage of multipath propagation effects [6]. Furthermore, other diversity schemes utilizing two or more antennas effectively provide a robust wireless communication link over fading channels [7]-[9].

Besides complexity and cost, such systems often require high power that is undesirable for most wireless ad hoc networks. In this regard, we consider low frequency wireless communications that can significantly reduce the effect of multipath and signal attenuation in complex environments. Recently, signal propagation characteristics at lower frequency bands have been investigated through physics-based simulation and extensive measurements in various non-line-

of-sight (NLOS) scenarios [10]-[12]. These studies show that High Frequency (HF) and the lower end of the Very High Frequency (VHF) bands (30-60 MHz) have superiority over higher frequencies in terms of the reliability of wireless links in complex indoor and outdoor environments, resulting from much less multipath fading, attenuation, phase distortion, and delay spread. These characteristics provide competitive advantages in applications in Global Positioning System (GPS)-denied environments, such as high-resolution direction finding, situational awareness services for soldiers and first responders, and multi-robot autonomous networking with seamless wide-area coverage.

Despite these advantages, practical applications of low-frequency wireless mobile system are limited mainly because of large antenna sizes or high-power requirement if small antennas with poor radiation efficiency are to be used. Since there inherently exists a trade-off between antenna size and performance, antenna dimensions are usually specified, depending upon the particular applications. For example, tactical long-range VHF communications for a range of military vehicles typically use large-size vehicular antennas (e.g., VHF3088EF/50: height = 2.6 m & gain = 3.19 dBi at 40 MHz) [13]. On the other hand, relatively smaller VHF antennas (e.g., OMNI-A0180: height = 0.84 m & gain = -23 dBi at 40 MHz) [14] are used for manpack networking radios, considering mobility and quick deployment for ad-hoc short-range communications (see Fig. 1.1). This clearly indicates that antenna size can be a major bottleneck for reducing the size of low-frequency wireless mobile systems.

Low-power operation is critically important for tactical mobile radios. Unfortunately, very small antennas with high radiation efficiencies in the desired band do not exist. The research presented here starts from how such a technical barrier at HF/low-VHF bands can be overcome.

(a) (b)

Figure 1.1: (a) Military vehicle antenna and (b) manpack radio antenna at VHF band.

1.2 Research Contributions

Rigorous studies on wave propagation properties in complex propagation environments are of paramount importance to understand effectiveness of low-frequency bands for reliable, mobile low-power radios. While a number of radio propagation models at microwave frequency bands for satellite and telecommunication systems in indoor and urban scenarios have been developed theoretically or empirically [15]-[18], there has been a lack of similar information about the propagation characteristics at HF/low-VHF bands for such scenarios. The first contribution of this research is the development of an empirical near-ground propagation model based on large data collections in various complex scenarios (indoor, indoor-to-outdoor, and NLOS outdoor settings) [10]. The data collections are carried out with an in-house-designed, extremely miniaturized antenna (see Fig. 1.2(a)) [19] at low VHF, facilitating a very compact, mobile system for near-ground communication.

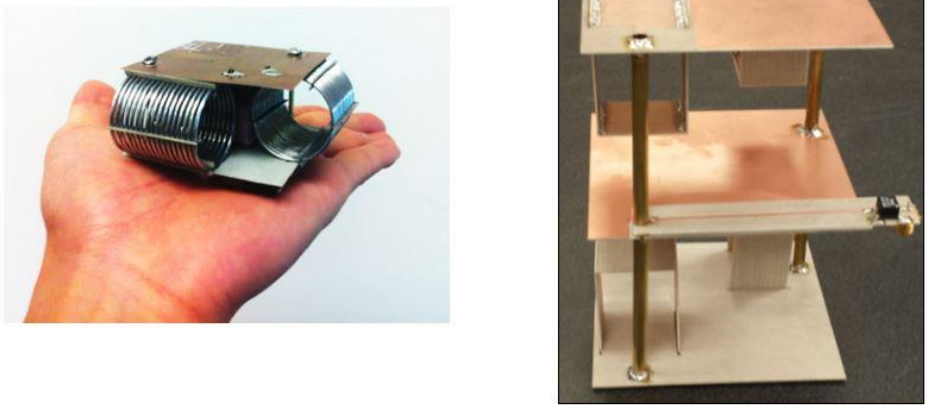

(a) (b)

Figure 1.2: Recent advances in highly miniaturized low-VHF antenna design: (a) a palm-sized miniature antenna ($0.008\lambda_0 \times 0.008\lambda_0 \times 0.004\lambda_0$ at 40 MHz) and a short folded dipole ($0.013\lambda_0 \times 0.013\lambda_0 \times 0.02\lambda_0$ at 40 MHz).

The second contribution of the research pertains to the design of an efficient small-form-factor antenna (see Fig. 1.2(b)) [20], and a technique enhancing its bandwidth at low-VHF band. The antenna specifications (size, gain, and bandwidth) for design are determined in view of the mean path-loss advantages (Low-VHF vs. Wi-Fi bands) obtained from the aforementioned data collection. Applications of the antenna are specified by a high degree of miniaturization and corresponding bandwidth (e.g., compact, low-data-rate, mobile ad-hoc networking). The antenna is designed with particular attention to enhancement of its radiation efficiency as well as compactness ($0.02\lambda_0$ in length at 40 MHz). To enhance the bandwidth (0.35 % for a voltage standing wave ratio of 2:1) of this efficient small antenna at the cost of a considerable size reduction, a non-Foster matching technique employing active devices, called a negative impedance converter, is also proposed. The non-Foster matched antenna provides a wider bandwidth that is

more than twice compared to that of the passive antenna while having an overall power efficiency advantage [21], [22].

A very effective and time-efficient method for accurate characterization of VHF antennas is also developed using very-near-field measurements over arbitrary closed surfaces with an electro-optical (EO) system and a novel near-field to far-field (NFFF) transformation formulation [23]. Performance characterization for VHF antennas is challenging due to a number of factors: For indoor measurements, prohibitively large anechoic chambers and absorbers are required; for outdoor measurements, a large open space and cumbersome antenna setup are required, and the effect of ground must be examined. Employing the proposed very-near-field scanning approach, performance of these antennas can effectively be characterized in a small indoor space without costly large anechoic chamber facilities and expensive computation and truncation errors from the NFFF transformation.

Compact, low-power mobile radio networking at low VHF for challenging complex environments is demonstrated utilizing the miniature antenna fully characterized by the afore-stated method [24]-[25]. As an enabler for the technology demonstration, the off-the-shelf ZigBee technology, developed for low-data-rate, short-range wireless networking, is leveraged. A bi-directional frequency converter is designed to translate signals occupying the ZigBee frequency bands (UHF) to low-VHF band and vice versa. The ZigBee-based compact low-VHF radio system comprising the off-the-shelf ZigBee module and frequency converter along with the miniature antenna constitutes a compact, low-cost, low-power radio. It is shown that this radio achieves highly reliable and persistent communications in complex propagation environments, far superior to its microwave counterparts.

1.3 Dissertation Overview

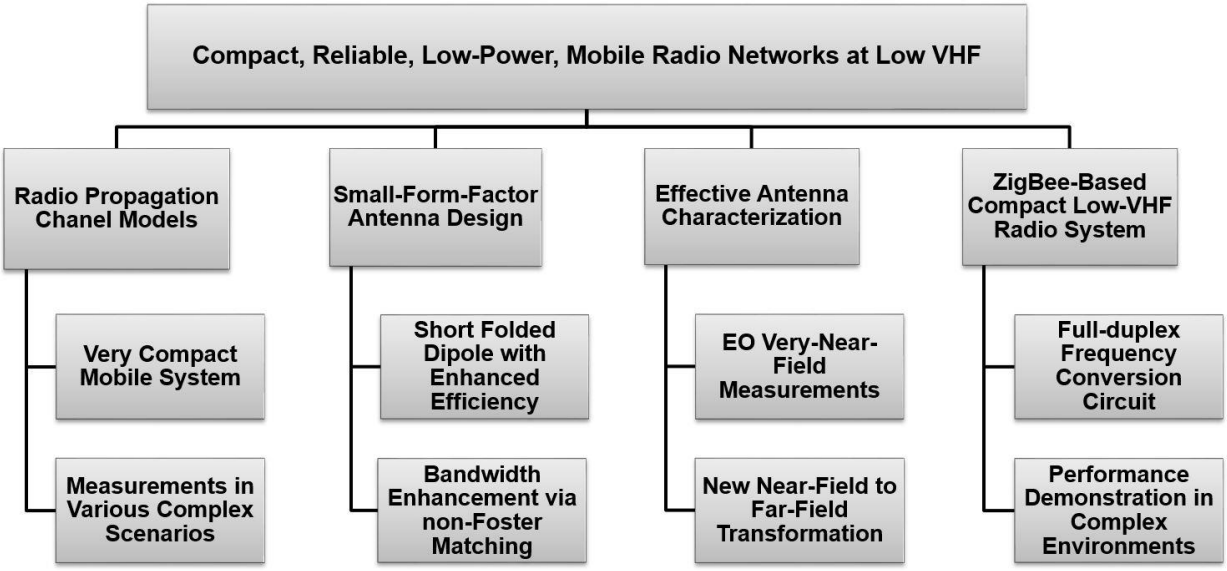

Figure 1.3: Dissertation overview.

CHAPTER II: Empirical Characterization of Near-Ground Radio Channels in Complex Environments at Low-VHF Band

The focus of this research is to characterize near-ground wave propagation in low-VHF band and to assess the advantages of this frequency band for reliable short-range low-data rate communications and geolocation applications in highly cluttered environments, as compared to conventional systems in the microwave range. Propagation measurements at the lower VHF band are conducted by using the miniature antenna (see Fig. 1.2(a)) to appraise the potentials of a compact, mobile, low-frequency system for near-ground communication. Quantitative comparison and analysis on the excess path-loss and small-scale fading between low-VHF (40 MHz) and Wi-Fi bands (2.4 GHz) are carried out based on short-range measurements in various multipath-rich

scenarios. For each measurement scenario considered, the path-loss and small-scale fading statistics are characterized after calibrating the differences in the systems (antenna gain, transmit power, etc.) used for measurements at different frequencies.

CHAPTER III: Development of a Highly Miniaturized, Lightweight Low-VHF Antenna

This research presents a highly miniaturized, lightweight antenna operating at low-VHF band as a key component that enables compact mobile radio systems. Earlier studies on an extremely short HF monopole antenna consisting of two in-phase vertical elements face an inevitable issue regarding an unbalanced coaxial cable feed due to the very small ground plane [19]. To resolve this problem, as well as to achieve higher bandwidth, an electrically small folded dipole version of the same antenna having a fully balanced structure is introduced. The overall dimension and total mass of the proposed antenna are 10 cm × 10 cm × 15 cm ($0.013\lambda_0 \times 0.013\lambda_0 \times 0.02\lambda_0$ at 40 MHz) and 98 grams, respectively. The gain and pattern of the fabricated antenna are measured in an elevated range that is in nearly free space conditions. Measurements are shown to be in agreement with the design predictions from the simulation.

CHAPTER IV: Bandwidth Enhancement of the Miniature Low-VHF Antenna

Bandwidth enhancement of a highly miniaturized low-VHF antenna via a non-Foster matching technique is demonstrated for low-power, short-range, wireless transmission systems. The miniature passive antenna introduced in Chapter III limits the extent of mobile applications due to its narrow bandwidth. In order to relax this constraint, a non-Foster matching network realized by a negative impedance converter is introduced. We address challenging issues associated with applying the matching network to the miniature antenna, such as antenna

impedance modeling and stability against system sensitivity. With an optimally designed matching network via circuit simulation, the non-Foster matched antenna is fabricated and tested. The results show an effective power bandwidth with a power efficiency advantage is 2.15 % with the non-Foster matched antenna, which is more than twofold broader than that of the passive matched one.

CHAPTER V: An Effective Technique for Performance Characterization of VHF Antennas

An effective method to characterize pattern and gain of VHF antennas is presented. This method can offset disadvantages of low-frequency antenna characterization that involve requirement of very large anechoic chambers (e.g., the PSU/ARL facility supporting VHF antenna testing: 30 m long × 12 m wide × 12 m tall) and large-size absorbers (e.g., pyramidal absorber (AEP-96): 2.4 m in length for absorption of 15 dB at 30 MHz at normal incidence) for indoor measurements and rather cumbersome setup for outdoor measurements. The proposed approach is based on measuring the tangential components of electric field over arbitrary closed surfaces that enclose the antenna under test (AUT) very close to the antenna boundary using an electro-optical system. Far-field radiation is computed from a new near-field to far-field transformation formulation using the tangential electric field measured over the closed surfaces. This procedure employs reciprocity theorem and the excited electric current on the surface of a PEC enclosure having the same geometry as the scanned surface and illuminated by a plane wave. In this way, a full spherical radiation pattern and gain of the AUT are easily computed without expensive computation and truncation errors. Applying this approach, the aforementioned miniaturized low-VHF antenna is characterized. The far-field results from this method are shown to be in agreement with those obtained from full-wave simulation and direct far-field measurement performed in an elevated outdoor range.

CHAPTER VI: Compact, Low-Power, Low-VHF Mobile Radio Networking in Complex Propagation Environments

This research is centered on a demonstration of a compact, low-power, mobile radio networking at low-VHF band for challenging complex environments. Existing commercial radios at this band are typically bulky, operate at high power levels that are at least a few watts, or require large-size high-performance antennas to facilitate long-range communications. To circumvent these difficulties, we demonstrate application of an off-the-shelf microwave ZigBee radio operating seamlessly in low-VHF band. A bi-directional frequency converter is designed to translate ZigBee signals into low-VHF carriers and optimized to simultaneously minimize power consumption and maximize system gain and sensitivity. The miniaturized antenna mentioned previously (see Fig. 1.2(b)) is further modified to broaden its bandwidth in consideration of proximity effects resulting in a shift in resonant frequency due to a large number of surrounding objects in complex environments. This antenna enables the compact radio system to operate at lower power as well as integrate onto small autonomous agents desirable for military or rescue missions. The performance is evaluated in various complex scenarios, along with a comparison test using a ZigBee module operating at 2.4 GHz, through the signal coverage maps together with the average receiver signal strength indicator (RSSI) value and packet error rate as a function of distance. The results demonstrate that the low-power, low-VHF radio can provide highly reliable and persistent communications in complex propagation environments.

CHAPTER II

Near-Ground Wave Propagation in Complex Environments

2.1 Introduction

Reliable wireless communication is vital for many civilian and military applications. In complex propagation scenarios such as caves, complex terrain, and indoor and urban environments, signal attenuation and multipath impose stringent conditions on power and signal processing. This is especially true at frequency bands where conventional communication systems operate (i.e., microwave frequency bands). One application of interest is achieving a reliable communication link among an ensemble of small aerial and/or ground robotic platforms deployed in such environments to enhance tactical situational awareness. Radio communication presents complex challenges for the small robotic platforms because important wireless infrastructures, such as base stations with predetermined positions, are typically absent and high transmit power is not available. Much effort has been devoted over many decades to design modulation schemes appropriate for different communication bands to overcome challenges introduced by the communication channel and factors such as noise and interference.

In general, it is understood that channel complexity is far less at lower frequencies for two reasons. First, significant signal penetration through/over obstacles is possible. Second, reflection, scattering, and diffraction phenomenon is less significant than what is encountered at UHF and higher bands. The severe signal fluctuations and intermittent signal dropoff that are unavoidable

at higher frequencies are significantly reduced at the HF and lower VHF bands due to reduced reflection and scattering. It should be mentioned, however, that the multipath effect is the main source of connectivity between a transmitter and a receiver in a complex environment at higher frequencies, where the direct path signal is extremely weak. On the other hand, at lower frequencies, the size of conventional antennas is very large, making application of such systems limited to stationary nodes or, in the case of mobile nodes, the transmit power has to be high enough to compensate for the poor efficiency of the small antennas.

With the advent of miniaturized HF and lower VHF antennas having a moderate gain [19], [26], interest in low-power HF and VHF communication links is increasing. In order to quantitatively study the advantages of an ad-hoc wireless system at the lower VHF band for short-range communications and geolocation applications in cluttered environments, accurate field coverage, path loss, and small-scale fading measurements in representative complex propagation scenarios are needed. Although there has been significant work done to study propagation at different frequency bands including microwave and VHF bands [12], [27]-[35], quantitative studies of the short-range low-power wireless channel in lower frequency bands (e.g., HF/lower VHF bands) are not available.

In this work, propagation measurements in complex indoor/outdoor scenarios are utilized to quantitatively study the advantages of a radio link in the lower VHF band as compared to conventional higher frequencies (e.g., 2.4 GHz). In Section 2.2, we describe the measurement system including the design and characterization of an extremely small antenna operating in the lower VHF band, which is integrated with the measurement system. The measurement scenarios

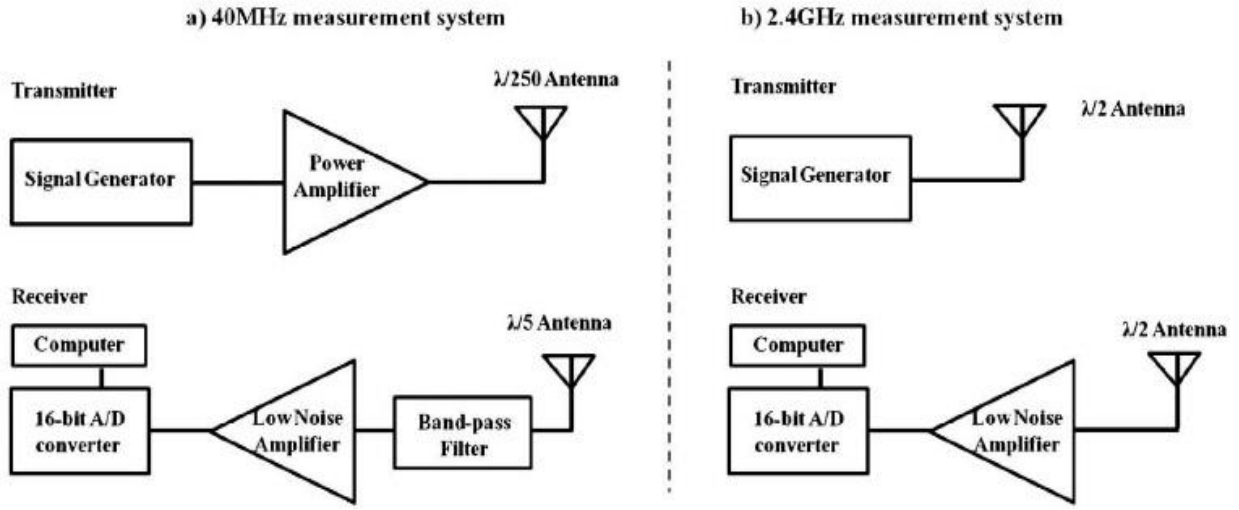

(a) (b)

Figure 2.1: Transmit and receive system diagram for (a) 40 MHz measurements and (b) 2.4 GHz measurements.

are presented in Section 2.3. In Section 2.4, the propagation measurement results are discussed. Path loss and small-scale fading comparison at 40 MHz and 2.4 GHz for various non-line-of-sight (NLOS) scenarios are also presented.

2.2 Measurement System

2.2.1 40 MHz Receiver Hardware

A highly sensitive receive circuit was designed and fabricated to accurately measure propagation at the HF and lower VHF band. The receiver system (see Appendix A) consists of a low-power 16 bit, two-channel analog to digital (A/D) converter which also has a wide dynamic range. The A/D converter has a maximum available sampling rate of 80 mega-samples/sec. A narrow-band, low-insertion loss band-pass filter along with a 40 dB low-noise amplifier is also

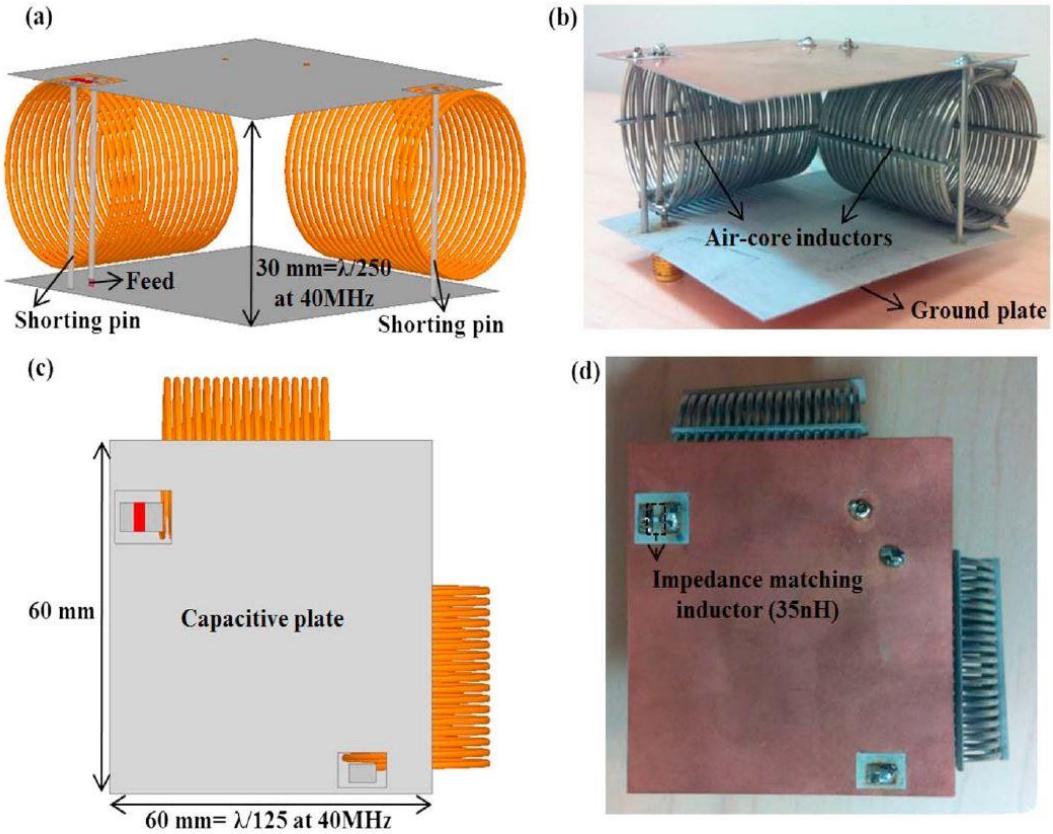

Figure 2.2: (a) and (c): the optimized dimensions of the extremely miniaturized antenna incorporating air-core inductors are shown. (b) and (d): side and top view of the fabricated antenna are shown.

used to enhance/suppress the out of band noise and improve the signal of interest. It should be noted that all components used in the receive system are carefully characterized by measuring the losses introduced by each component. This will ensure a fair comparison between measurements across different frequency bands.

The antennas utilized for these measurements include short dipoles ($\lambda_0/5$) and a highly miniaturized antenna ($\lambda_0/250$), all of which are designed to operate at the lower VHF band. In order to tune the $\lambda_0/5$ short dipole to the desired center frequency of 40 MHz and enhance its gain, two high-quality factor (Q) coils are utilized on either arm of the short dipole. The system diagram of the 40 MHz measurement is given in Fig. 2.1(a).

2.2.2 Highly Miniaturized Antenna at 40 MHz

A key consideration for establishing a compact, mobile communication system in the lower VHF band is the large size of the antenna owing to the long electrical wavelength at this frequency band. While different types of miniaturized antennas for VHF applications have been reported in the literature [36]-[37], such antennas are bulky and not appropriate for compact, mobile platforms. In order to enable the mentioned applications as well as to facilitate the ease of wave propagation measurements at the lower VHF band, a highly miniaturized, lightweight antenna was designed and fabricated. The lateral dimension and height of the antenna including the ground plane are 60 mm (λ_0/125) and 30 mm (λ_0/250) at 40 MHz, respectively. The design approach is based on employing two closely spaced short vertical elements producing in-phase radiated fields to significantly improve the radiation efficiency. The two in-phase vertical elements radiate in such a way that the effective height of the antenna is increased without increasing the physical height of the antenna. This gives rise to the enhanced gain of the monopole-based miniaturized antenna compared to a short monopole with the same height.

To achieve the in-phase radiated fields from electric currents flowing on the two vertical elements while minimizing the size of the antenna, a T-type 180° phase shifter with a capacitive impedance inverter is used [19]. However, a lumped capacitor in the phase shifter cannot be used as it causes an out-of-phase conduction current in the capacitor branch which would result in radiation cancelation. For the sake of avoiding this cancelation and achieving the desired 180◦ phase shift at the same time, the conventional T-type 180◦ phase shifter can be modified by replacing the lumped capacitor with an open stub whose capacitance value is determined by the

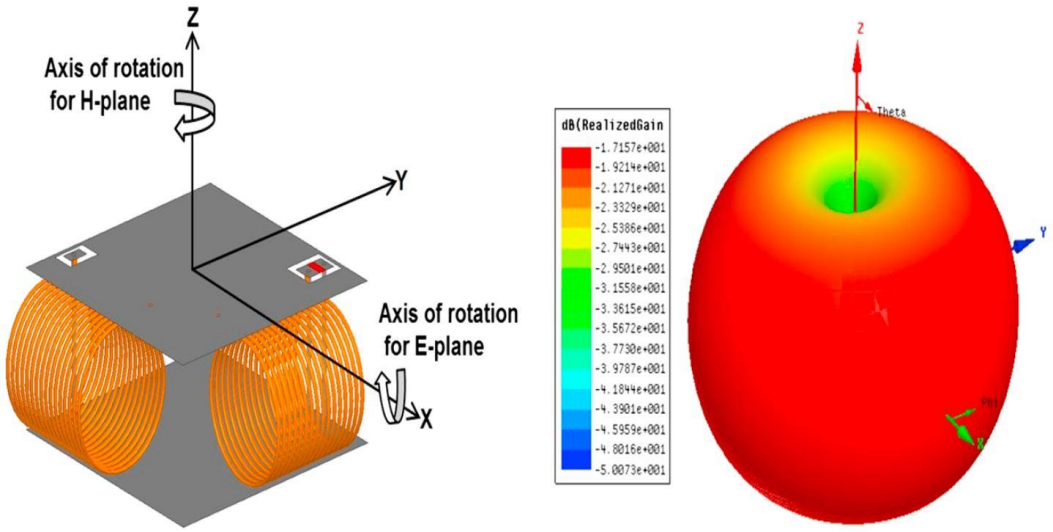

Figure 2.3: Three-dimensional radiation pattern (E_θ) of the extremely miniaturized low-VHF antenna.

area of the capacitive loading. The antenna geometry applying the modified *T*-type 180◦ phase shifter is shown in Fig 2.2. Optimized high *Q* air core inductors (> 1000) are utilized in the phase shifter to minimize power loss from the antenna and integrated between the top and ground plates so as not to increase the overall vertical profile of the antenna. Furthermore, the weight of the antenna is minimized by the use of aluminum wire for construction of the air core inductors and vertical pins. The total measured weight of the fabricated antenna is 18.54 grams, which enables integration with small mobile platforms.

Fig. 2.3 shows the 3-D radiation pattern of the antenna tuned to 39.1 MHz. The antenna is vertically polarized and has an omnidirectional radiation pattern as shown in Fig. 2.3. Therefore, it is suitable for near-ground operation since path loss between two near-ground antennas with vertical polarization is far lower than any other polarization [38]. Fig. 2.4 depicts the normalized power received by the $\lambda_0/5$ dipole antenna, when the miniaturized antenna and an identical $\lambda_0/5$ dipole antenna are used for transmitter (Tx). The two antennas are tuned to the same operating

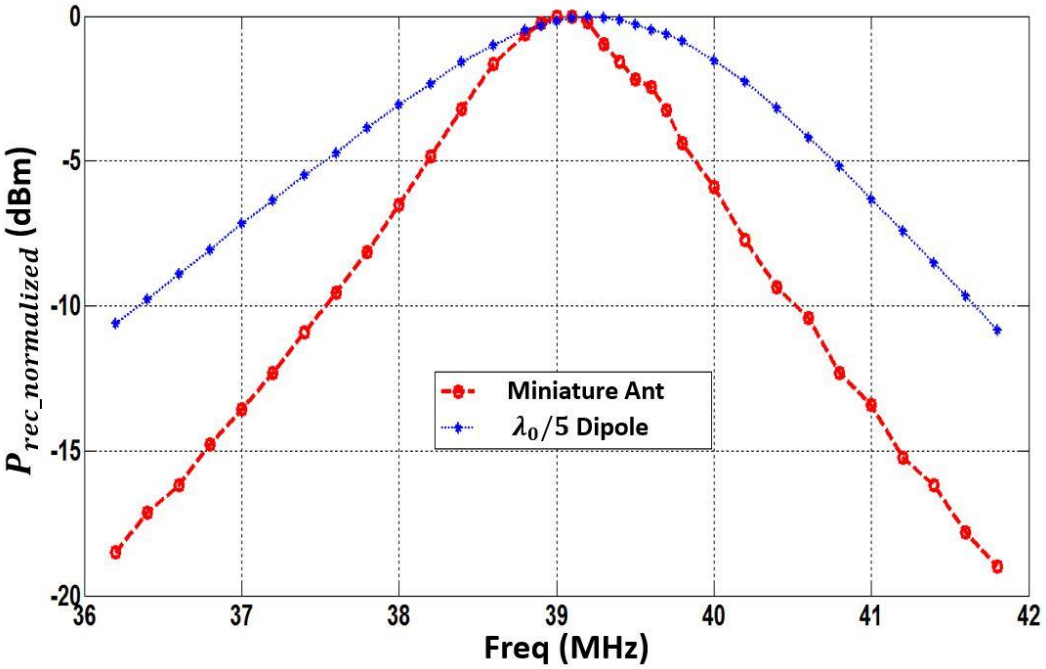

Figure 2.4: Normalized receive power versus frequency, for two different transmit antennas (dashed: miniaturized antenna; solid: $\lambda_0/5$ dipole). The $\lambda_0/5$ dipole was used on a receiver for both cases.

frequency of 39.1 MHz. The bandwidth of the miniaturized antenna is narrower than that of the $\lambda_0/5$ dipole antenna due to a high degree of miniaturization with the use of the high-quality factor of the air core inductors. For this reason, objects that are in close proximity to the antenna ($< \lambda_0/2\pi$) could affect the performance of the antenna because of a shift in resonance frequency. This effect has been investigated based on measurements, and it has been shown that the resonance frequency is stable in the presence of nearby objects in indoor environments where the distance between the antenna and the object is within the near-field reactive region of the antenna [19].

2.2.3 2.4 GHz Measurement System

As alluded to earlier, we carry out path loss and small-scale fading measurements at 2.4 GHz in the same scenarios for comparison against the 40 MHz results. A signal generator is used

Table 2.1
Comparison of parameters used for 40 MHz and 2.4 GHz propagation measurements carried out in the three scenarios described in section 2.3

Parameter	40 MHz	2.4 GHz
P_t (GG Brown)	35 dBm	15 dBm
P_t (EECS)	15 dBm	10 dBm
P_t (ERB)	5 dBm	15 dBm
T_X antenna	Miniature antenna	λ_0/2 dipole
R_X antenna	λ_0/5 dipole	λ_0/2 dipole
G_{T_X}	-21 dBi	2.15 dBi
G_{R_X}	-0.96 dBi	2.15 dBi
h_{T_X}	1.22 m ($0.16\lambda_0$)	3.2 cm ($0.26\lambda_0$)
h_{R_X}	1.62 m ($0.22\lambda_0$)	3.2 cm ($0.26\lambda_0$)
T_X R_X polarization	V, V	V, V
R_X amp gain	40 dB	30 dB
Impedance mismatch loss	1.5 dB	-
Filter losses	1.5 dB	-
Cable losses	0.3 dB	2.8 dB
Near-ground path loss compensation [32]	-	3.1 dB

to transmit a 2.4 GHz tone at a power level of 10 dBm. On the receive end, a spectrum analyzer connected to a low-noise amplifier is used to acquire the received signal strength at various locations. Half-wave dipoles are utilized at both transmitter and receiver for measurements at 2.4 GHz. Relevant parameters of the measurement system are listed in Table 2.1. Also, a diagram of the measurement system used for the 2.4 GHz measurements is given in Figure 2.1(b).

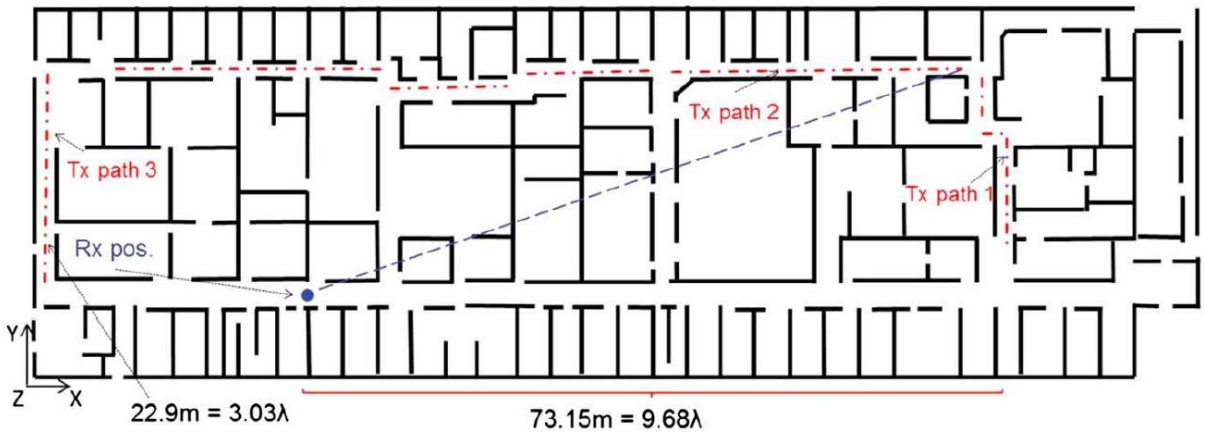

Figure 2.5: The floor plan of the second floor of the GG Brown building at the University of Michigan. The transmitter paths (T_X paths 1, 2, and 3) are also shown. The receive antenna was positioned at a fixed location (R_X pos.). The dotted diagonal line represents the signal path that penetrates through multiple layers of walls from the upper right corner of the hallway to the receive antennas.

Table 2.2
Various scenarios for propagation measurements

	Building	T_X Location	R_X Location	Floor	Setup
Scenario 1	GG Brown	Indoor	Indoor	Second	NLOS
Scenario 2	EECS	Outdoor, Indoor	Indoor	First, Third	NLOS
Scenario 3	ERB	Outdoor	Outdoor	First	NLOS

2.3 Measurement Scenarios

The measurements were collected in three different environments. For all the buildings, the wall thickness varied from 20 cm to 30 cm. The floormap of the first building where the measurements were carried out is shown in Fig 2.5. This is a large office building with interior walls made of cinder blocks with metallic reinforcements on the ceiling and floors. It should be noted that many of the rooms in this building contain furniture, including metallic cabinets, tables,

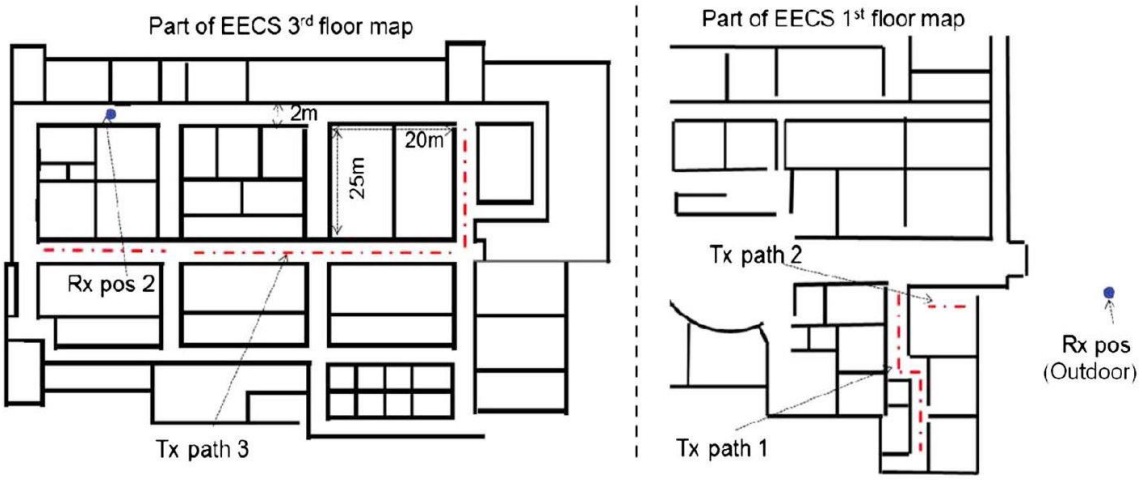

Figure 2.6: The floor plans of the first and third floors of the Electrical Engineering building at the University of Michigan. The transmitter paths (T_X paths 1, 2, and 3) are also shown. The receive antenna was positioned at two locations (R_X pos. 1 and R_X pos. 2).

and chairs. The transmit and receive antenna arrangements for the measurements obtained in this building are shown in Table 2.2.

The second building is shown in Fig. 2.6 and has interior walls that are built from bricks, covered by drywalls and metallic studs. The floor and ceilings also include metallic mesh with spacing well below the wavelength in the lower VHF band. It should be noted that the presence of periodic metallic studs in the walls, floors, and ceilings can cause significant attenuation of low-frequency signals including in the lower VHF. This attenuation is even more pronounced for vertical polarization because a significant fraction of the transmitted signal will be reflected by the vertical metallic studs (see Appendix A). This building was chosen to study lower VHF propagation and quantify path loss in challenging scenarios with significant metallic barriers. Both outdoor-to-indoor and indoor-to-indoor links are studied based on measurements carried out in this building.

In a third scenario, outdoor measurements were conducted adjacent to the building shown in Fig 2.7. This building is also built from bricks and includes significant metallic reinforcement,

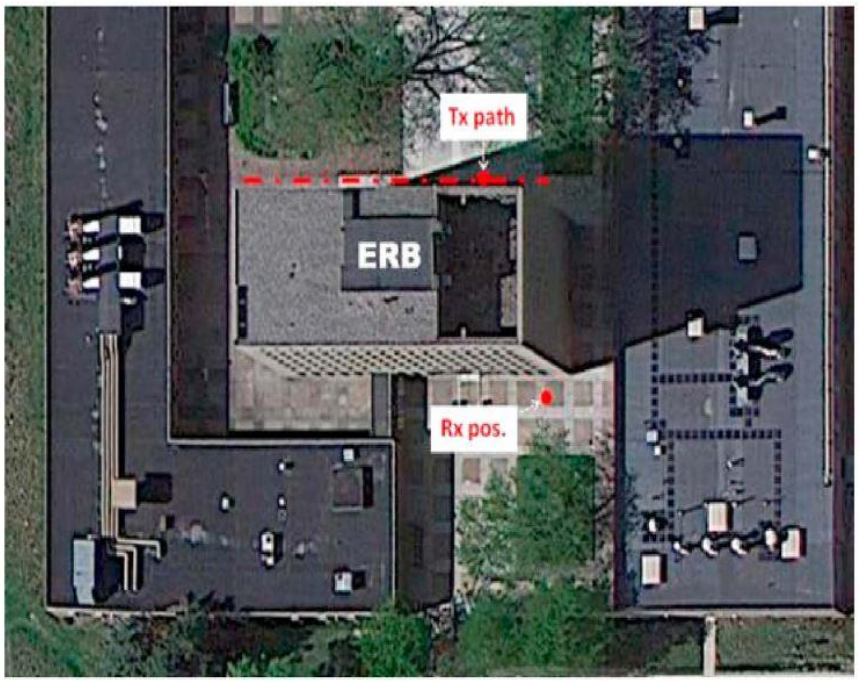

Figure 2.7: The top view of the Engineering Research Building (ERB) at the University of Michigan. The receive antenna was positioned at R_X pos., and T_X antenna is moved along the T_X path as indicated.

Table 2.3
Summary of measurements in three different buildings

	Building	T_X Path	Maximum T_X-R_X Distance	Number of Walls between T_X and R_X	Path Loss Difference (2.4 GHz vs. 40 MHz)
Case 1	1	1	76 m ($10.1\lambda_0$)	≤ 14	~35
Case 2	1	2	75 m ($10\lambda_0$)	≤ 14	~35
Case 3	2	1	33 m ($4.4\lambda_0$)	≤ 4	~40
Case 4	2	2	23 m ($3.1\lambda_0$)	≤ 4	~45
Case 5	3	1	36 m ($4.8\lambda_0$)	≤ 7	~55

and the interior contains office furniture and a variety of metallic objects. This set of measurements is utilized to investigate the path loss in outdoor-to-outdoor NLOS links. By placing the Tx and

Rx antennas on opposite sides of the building, penetration through the building in the presence of several layers of walls and other scatterers is measured at 40 MHz and 2.4 GHz. A summary of the measurements carried out in three different building environments is given in Table 2.3.

2.4 Analysis and Results

In this section, path loss results based on the various measurements are discussed. Specifically, the propagation mechanisms at the lower VHF band and at the 2.4 GHz band are compared. It should be noted that the goal here is not to study path loss in open environments where it is well established that path loss increases with frequency. Instead, propagation measurements and analysis for LOS and NLOS scenarios are performed to compare the penetration loss through layers of building walls and to compare the level of small-scale fading at the two frequency bands. These effects are critical for short-range penetration and communications in the densely cluttered environments under study. The variations in antenna performance and near-ground propagation effects that vary with frequency are taken into account to accurately characterize the propagation characteristics as a function of frequency [12]. For each frequency band, the transmit power and the gains of the amplifiers are adjusted as needed to compensate for differences in antenna gain and other system losses including filter and cable loss. Furthermore, the Tx and Rx antennas are positioned so that they have similar heights in terms of electrical length. The reason for this is to make sure the near-ground propagation effects, which are dominant when the height of the antennas are less than a wavelength, are similar at the two frequency bands [11], [32]. Discussion of path loss calculations from the measured data and the results for various types of channels are presented in the rest of this section.

2.4.1 Path Loss Calculations

In order to compare the channel path loss, all system parameters at the two frequency bands are carefully taken into account. The path loss PL in decibels can be calculated as a function of frequency as

$$PL\,(f) = P_t(f) - P_r(f) + G_t(f) + G_r(f) + G_{Sys}(f), \tag{2.1}$$

where $P_t(f)$ and $P_r(f)$ are the transmit and receive power in decibels, respectively. Here $G_t(f)$ and $G_r(f)$ are the gains of the Tx and Rx antennas, and $G_{Sys}(f)$ is the sum of all other system gains and losses including amplifier gain, filter, and cable losses. It should be noted that variations in antenna performance along with other effects (e.g., differences in cable losses) are carefully measured at the two frequencies so that the channel path loss can be isolated and compared. This is done by making sure that the sum of all gains and the transmit power at each frequency is the same. Appropriate transmit power and amplifier gains are chosen to compensate for differences in antenna gain and other system losses. Table 2.1 shows a summary of various parameters used for the measurements. It should be noted that the path loss definition given above enables the comparison of signal attenuation and spatial variation induced by the channel based on measured results at the two frequency bands of interest.

2.4.2 Indoor-to-Indoor Channels

In this section, indoor measurements carried out near 40 MHz and 2.4 GHz are used to quantitatively study the advantages of the lower frequency band for reliable short-range

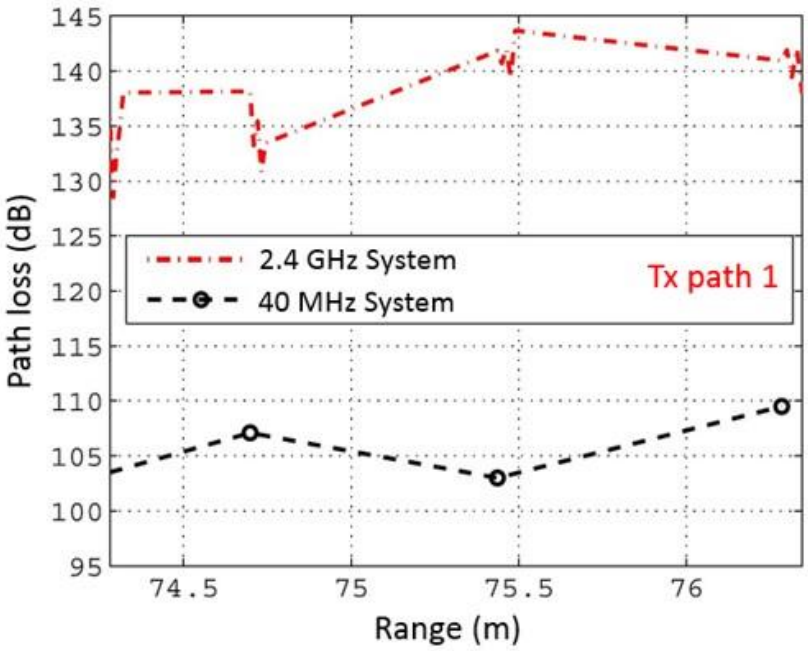

Figure 2.8: Comparison of path loss at 40 MHz and 2.4 GHz for Case 1 (T_X path 1 and receiver fixed at R_X pos.) of the GG Brown building shown in Fig. 2.5.

communication in complex propagation scenarios. We are particularly interested in characterizing the NLOS propagation in the lower VHF band where there are many layers of walls and other indoor obstacles between the Tx and Rx antenna. For this scenario, the farthest range between the Tx and Rx antennas is more than 76 m where 14 layers of walls and a multitude of scatterers are located between the Tx and Rx antennas. The received signal in this case consists mainly of the signal that penetrates through the walls, and other diffracted components are much smaller in amplitude. It should be noted that unless the measured point is near a hallway junction, the contribution from diffracted components is quite small.

In order to study path loss in this particular environment, three different NLOS paths are chosen and the measurement results at the lower VHF band (40 MHz) are compared with those obtained from the microwave range (2.4 GHz). The Rx antenna for the measurements is fixed, and the transmitter is moved along different paths (see Fig. 2.5). In both cases, the distance between

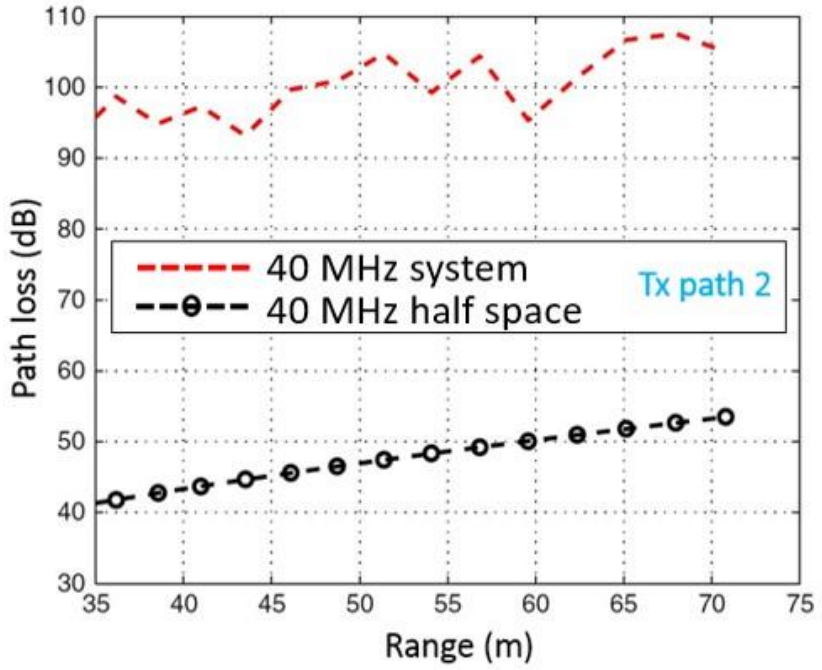

Figure 2.9: Path loss at 40 MHz for Case 2 (T_X path 2 and receiver fixed at R_X pos.) of the GG Brown building shown in Fig. 2.5.

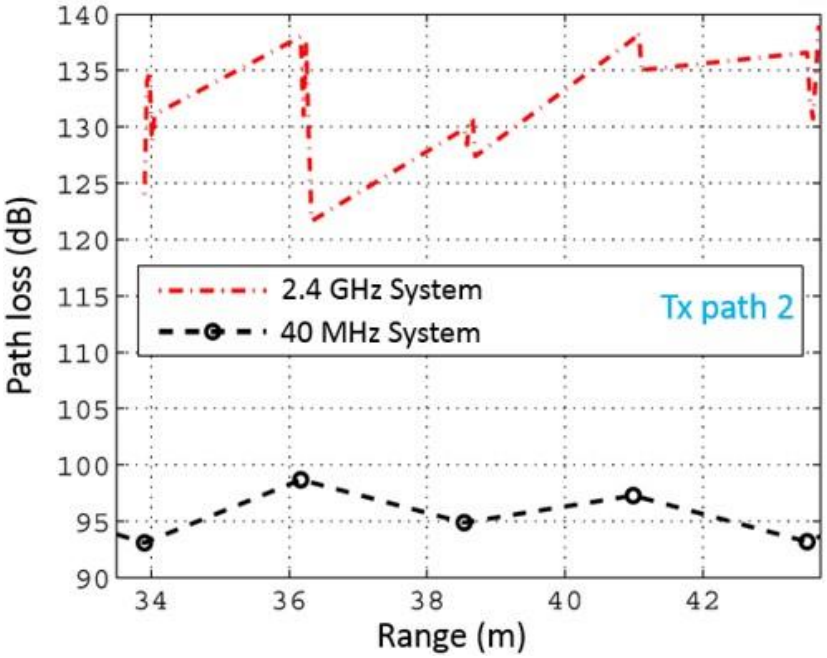

Figure 2.10: Comparison of path loss at 40 MHz and 2.4 GHz for Case 2 (T_X path 2 and receiver fixed at R_X pos.) of the GG Brown building shown in Fig. 2.5.

adjacent transmitter positions is chosen to be less than $\lambda_0/2$. Comparison between the path loss at

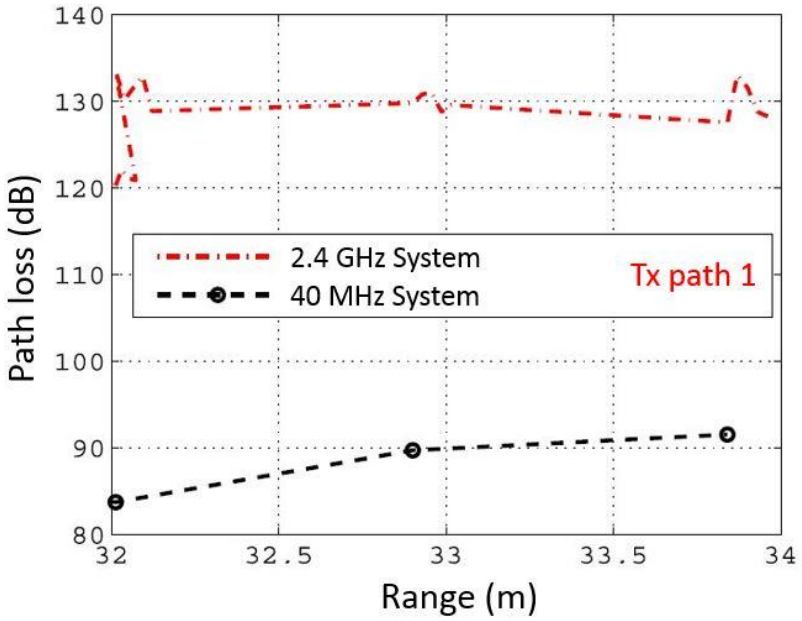

Figure 2.11: Comparison of path loss at 40 MHz and 2.4 GHz for Case 3 (T_X path 1 and receiver fixed at R_X pos.) of the EECS building given in Fig. 2.6.

the two frequencies of interest for a case where the Tx antenna was moved along Tx path 1 is shown in Fig. 2.8. In Fig. 2.9, the path loss for this indoor scenario is compared against that of the half-space dielectric medium to quantify the loss due to penetration through layers of building walls.

The path loss comparison for Tx path 2 is given in Fig. 2.10. We note two important points from these results. First, there is significant difference in path loss at 40 MHz and 2.4 GHz. This is because at 40 MHz (λ_0 = 7.5 m), the thickness of each wall is only a very small fraction of the wavelength, and thus, the signal penetration is significantly better compared to 2.4 GHz (λ_0 = 0.125 m), where the wall thicknesses are comparable to the wavelength. The second point is the fact that the signal coverage is much smoother at 40 MHz compared to 2.4 GHz where the signal fluctuates quite significantly. This is due to the fact that at the lower VHF band the signal coverage is dominated by the penetrated signal as opposed to reflected and diffracted components that are dominant at 2.4 GHz.

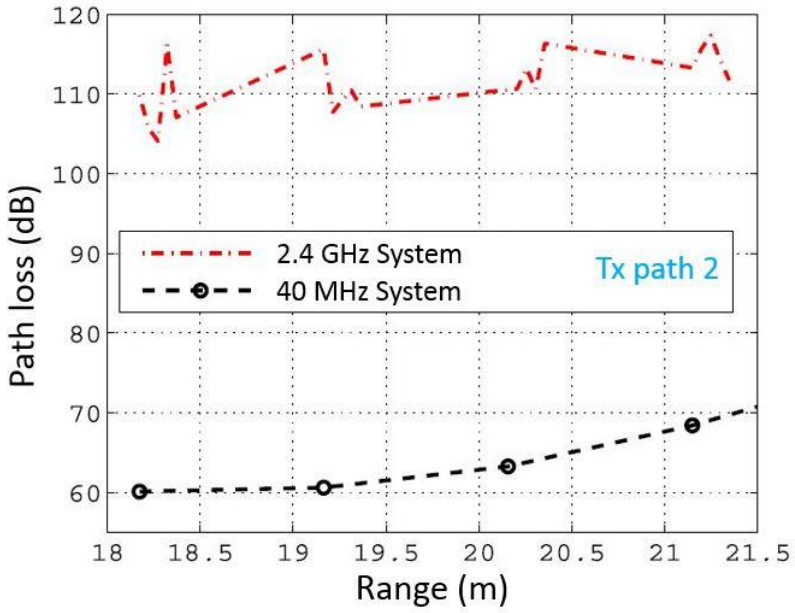

Figure 2.12: Comparison of path loss at 40 MHz and 2.4 GHz for Case 4 (T_X path 2 and receiver fixed at R_X pos.) of the EECS building given in Fig. 2.6.

2.4.3 Outdoor-to-Indoor and Non-Line-of-Sight Outdoor Channels

Next, we consider scenarios where at least one of the antennas is positioned outdoors. The scenarios are shown in Fig. 2.6 where the Rx antenna is positioned outside a building (EECS building at the University of Michigan) and the Tx antenna is moved within the building following different paths. The interior walls of this building have a lot more metallic reinforcement compared to the first building discussed in the previous section. The walls, ceiling, and floor have densely spaced metallic scatterers. We also consider an outdoor-to-outdoor NLOS channel where the two antennas are positioned on either side of a building as depicted in Fig. 2.7. Similar to the previous measurement, the path loss comparison in EECS building for Case 3 (Tx path 1 and Rx at fixed position) and Case 4 (Tx path 2 and Rx at fixed position) are given in Fig. 2.11 and 2.12, respectively. The path loss comparison for the outdoor-to-outdoor measurement is shown in Fig. 2.13. In each case, there is an average of more than 45 dB improvement at 40 MHz compared to

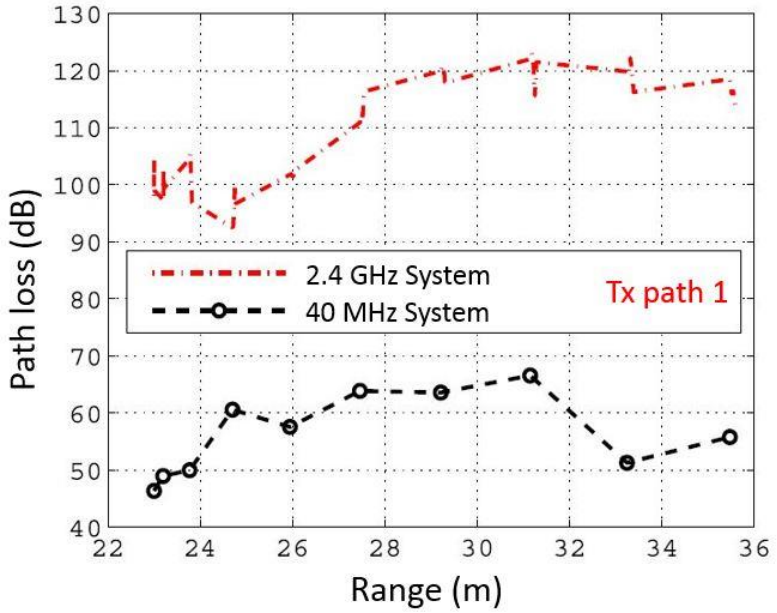

Figure 2.13: Comparison of path loss at 40 MHz and 2.4 GHz for outdoor-to-outdoor measurements (Engineering Research Building (ERB) at the University of Michigan given in Fig. 2.7) is shown. The parameters for this measurement are listed in Table 2.1.

2.4 GHz. Furthermore, the small-scale signal variation is significantly higher at 2.4 GHz which complicates the receiver processing and greatly enhances the probability of intermittent signal dropoff. These effects are minimal at 40 MHz. It should also be noted that the result shown in Fig. 2.13 (outdoor-to-outdoor) shows more signal variation since diffracted components make a more substantial contribution. This is true especially close to the beginning and the end of the Tx path (see Fig. 2.7).

2.5 Summary

In this chapter, measurement-based characterization of propagation in the VHF range in cluttered environments is presented. A quantitative path loss comparison between the lower VHF band and the microwave frequency range utilized in conventional systems is carried out. The

results point to potential short-range low-power applications of low VHF including reliable short-range communications in highly cluttered environments. In all the measurements at the lower VHF band, a short $\lambda_0/5$ dipole as well as an extremely small 40 MHz antenna (6 cm × 6 cm × 3 cm) were utilized. A brief discussion of the design and fabrication of the miniaturized antenna was given. Path loss and small-scale fading effects in and around three complex buildings were presented. Propagation scenarios including indoor-to-indoor, outdoor-to-indoor, and NLOS outdoor scenarios are considered, and path loss measurements and signal fading are studied at the lower VHF band (40 MHz) and the microwave band (2.4 GHz). For all scenarios, it is shown that the path loss at 40 MHz is on average 40 dB less than that of the 2.4 GHz case. As discussed earlier, when comparing the path loss results, all other variations at the two frequency bands caused by differences in antenna gain, Tx power, and amplifier gains have been accounted for. This was achieved by making sure that the sum of all system attributes affecting the received powers at the two bands (other than the propagation channel) were kept the same.

We emphasize that the goal is not to confirm the well-known fact that path loss increases with frequency as in the free space case. The main point of this research, demonstrated with the measurement results, is that even in highly cluttered environments (in the presence of dielectric and metallic obstacles), the propagation mechanisms at lower VHF and 2.4 GHz are very different. Significant penetration through several layers of building walls is possible at the lower VHF band because of the small electrical size of typical scatterers. On the other hand, at microwave frequencies signal penetration through building walls is small and multipath levels are much more significant. The implication is that the lower VHF band is more suitable for reliable and persistent low-power low-data rate communication in highly cluttered environments.

CHAPTER III

A Highly Miniaturized, Lightweight Low-VHF Antenna

3.1 Introduction

In complex propagation and highly cluttered environments such as caves and tunnels as well as indoor and urban scenarios, reliable wireless communication is very challenging. This is attributed to signal attenuation, distortion, and fading caused by dense scatterers in such scenarios. This has motivated recent studies of HF and VHF for short-range, low-power operation [10]-[11]. Key issues include multipath fading, attenuation, scattering, phase distortion, and delay spread, all of which are much less significant in the HF-VHF bands than those observed at higher frequencies (e.g., UHF) as addressed in Chapter II. Despite these advantages at these frequency bands, the realization of a compact system is challenging mostly owing to the large desired antenna size, or high power operation due to the poor efficiency of existing small antennas. Hence, the design of reasonably efficient miniature antennas is critical to enable compact, low-power communication applications at low-VHF band. While different types of miniaturized VHF antennas have been reported in the literature [40]-[41], these antennas are large in terms of their lateral dimensions or height and also heavy such that they are not appropriate for small platforms. Furthermore, slot antennas are miniaturized down to $0.03\lambda_0 \times 0.03\lambda_0$, but they need a relatively large ground plane which makes the overall antenna size large [42]-[43].

In this chapter, a miniaturized, lightweight antenna with a moderate gain is introduced. Two electrically short metallic posts in the antenna structure produce vertically polarized fields that are in phase at resonance. In this respect, the effective height of the radiator is increased without physically increasing the antenna height, which gives rise to enhanced gain. The in-phase radiated fields from electric currents flowing on the vertical elements are achieved by employing 180-degree phase shifters. To minimize the overall antenna loss and mass, optimized rectangular air-core inductors with high quality factors (Q) are used in the phase shifters. In Section 3.2 we present the fundamental design approach based on circuit analysis. The simulation modeling and fabrication of the proposed antenna are shown in Section 3.3. A particular measurement set-up for the antenna characterization and the results are discussed in Section 3.4.

3.2 Motivation and Design Approach

A previous study [19] explains how to produce in-phase vertically polarized fields from two very short, vertical conducting wires utilizing a modified T-type 180-degree phase shifter that replaces a capacitive impedance inverter with an open stub. Using this method, an extremely small HF antenna was designed. However, this design has a drawback because the electrically small size of the antenna ground plane ($0.0115\lambda_0 \times 0.0115\lambda_0$ at 23 MHz) causes undesirable performances due to near-field coupling to the feed line when a coaxial cable is used to feed the antenna which can shift the resonant frequency of the antenna and distort the radiation pattern. In addition, an added matching network consisting of another shorting post and a chip inductor is necessary to attain impedance matching to a 50-ohm feed, which takes up more space and reduces the overall

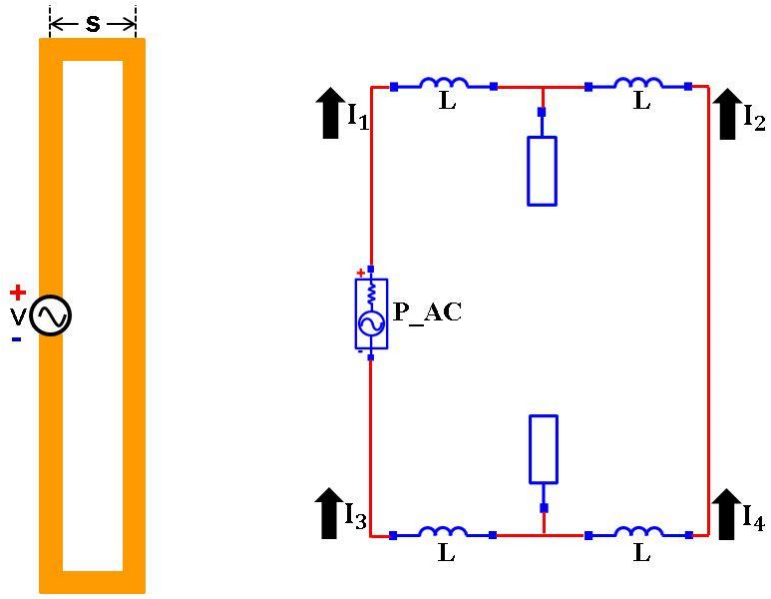

(a) (b)

Figure 3.1. (a) Geometry of a conventional folded dipole antenna and (b) circuit diagram for 180-degree phase shifters.

antenna efficiency. The very narrow fractional bandwidth (FBW $<$ 0.15 percent) also restricts the utility of the antenna to a limited number of applications.

To remedy the shortcomings mentioned above, we consider the concept of a folded dipole version of the antenna. Fig. 3.1(a) shows a conventional folded dipole that is composed of a basic dipole with an additional conductor connected at both ends to form a rectangular loop. A folded dipole, as its intrinsic property, provides an increase in the radiation impedance level. The spacing ($s \ll \lambda_0$) between the two vertical elements acts as a step-up impedance transformer of the single dipole impedance. Furthermore, it has a wider bandwidth than a single dipole with the same dimensions due to the fact that its geometrical arrangement serves as a short parallel stub line which results in partial reactance cancellation of the single dipole at a frequency away from resonance [44]. The proposed antenna is designed to exploit both properties of the folded dipole mentioned above and the 180-degree phase shifters resulting in a fully balanced system. The phase shifter is composed of two inductors and an open stub instead of a grounded lumped capacitor to

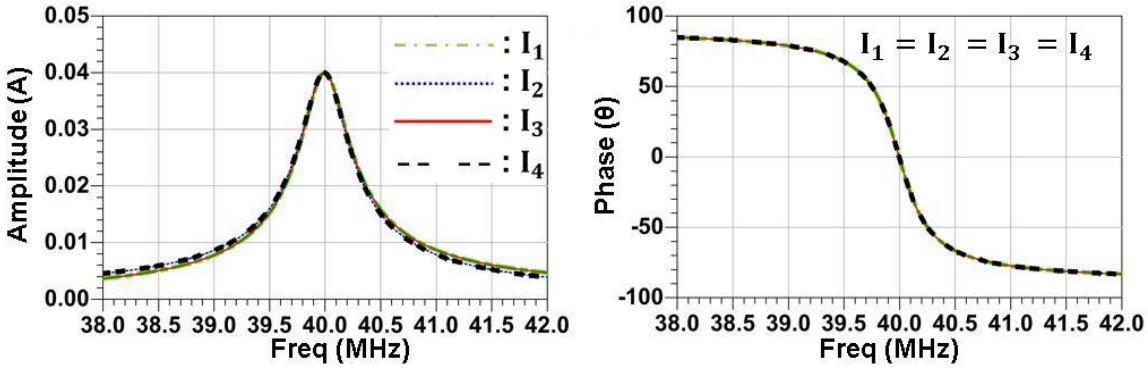

(a) (b)

Figure 3.2: (a) Simulated magnitudes and (b) phases of I_1, I_2, I_3, and I_4 shown in Fig. 3.1.

avoid radiation cancellation resulting from the conduction current flowing through the capacitor. Fig. 3.1(b) depicts a simplified circuit model of the antenna indicating the relative directions of the currents through each vertical wire. As can be seen in Fig. 3.2, at 40 MHz I_2 and I_4 flowing on the non-feed wire have the same phase as well as the same magnitude compared to I_1 and I_3 flowing on the feed wire, resulting from the inserted phase shifter in between. This leads to in-phase radiation occurring from the two vertical wires at the resonant frequency. For the circuit simulation, parameter values for inductors and open stubs are properly chosen to produce the 180-degree phase shift at the operating frequency.

3.3 Simulation and Implementation

3.3.1 Design of Rectangular Air-Core Inductors Employed in the Phase Shifter

Air-core coils can be used in the phase shifter, replacing lumped inductors with low-Q ferromagnetic cores. The Q of an air-core inductor depends on its geometrical and electrical parameters that impact the RF losses, such as metal conductivity, helical pitch and diameter, etc.

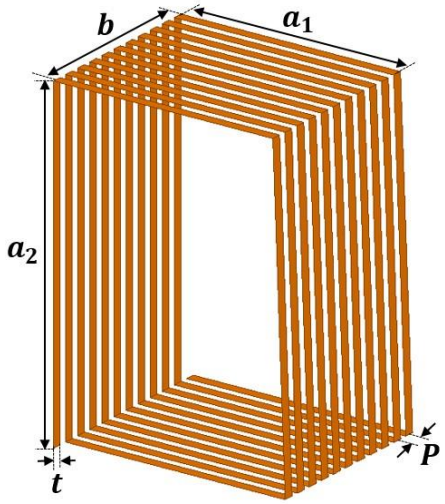

Figure 3.3: Design parameters of the rectangular air-core inductor.

Accurate analytical predictions of inductance and AC resistance of the coils have been reported [45]-[46]. Another important practical issue is the repeatable fabrication of relatively large coils. For ease of fabrication with high reliability, air-core coils with rectangular cross section are utilized. Fig. 3.3 shows design parameters of the rectangular coil parameterized by width a_1, length b, height a_2, thickness of the metallic strip t, and coil pitch P. The inductance of a rectangular air-core inductor is given by

$$L\ (\mu H) = 0.004\pi N^2 \frac{a_1 a_2}{b} F', \tag{3.1}$$

where N is the number of turns, $F'=\beta_1\gamma + \beta_1{}'\gamma log_e\frac{1}{\gamma} + \beta_2\gamma^2 + \beta_3\gamma^3 - \beta_5\gamma^5 + \cdots$, where $\gamma = b/a_2$, and the corresponding coefficients are obtained from Table II in [45]. The dimensions of the air-core coils with an inductance of 4.6 μH determined by the circuit analysis are optimized using the following steps. First, the height a_2 of the coil is predetermined considering a limited space from the metallic upper or bottom plate to the center plate where the coils will be positioned.

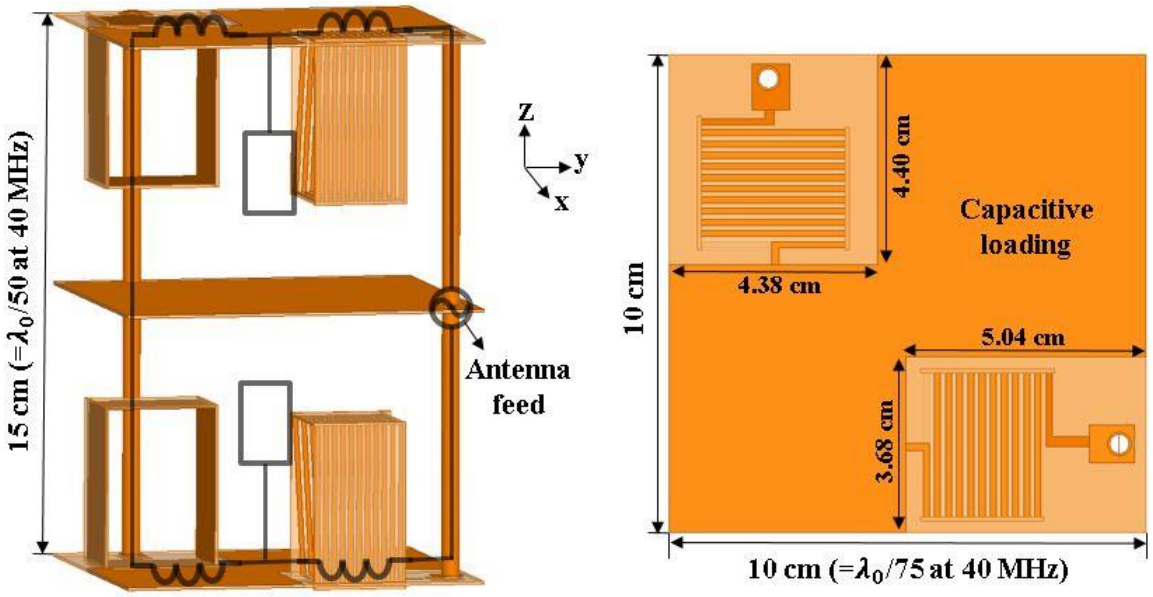

(a) (b)

Figure 3.4: (a) Side and (b) top view of the antenna design based on its equivalent circuit model. The circuit model is superimposed on the side view.

Second, with the coil length fixed, the width a_1 and length b of the coil which are also constrained by the antenna volume are adjusted allowing for the minimization of mutual coupling among the inductors. In [46] the variation of the average ratio of AC to DC resistance is shown as a function of the length b, width a_1, and the thickness t of the metallic strip of a rectangular coil. The proximity effect increases as the length of the coil decreases, while the other parameter values remain the same, which results in increasing the corresponding AC resistance. Hence, the length b, and consequently the number of turns N and the coil pitch P, are appropriately assigned to minimize the AC resistance from the proximity effect while achieving the targeted inductance of the coil. Optimizing the values of $a_1,\ a_2,\ b,\ t,\ N,$ and P we obtain 30.1 mm, 44.1 mm, 25.74 mm, 1.3 mm, 11, and 2.34 mm, respectively.

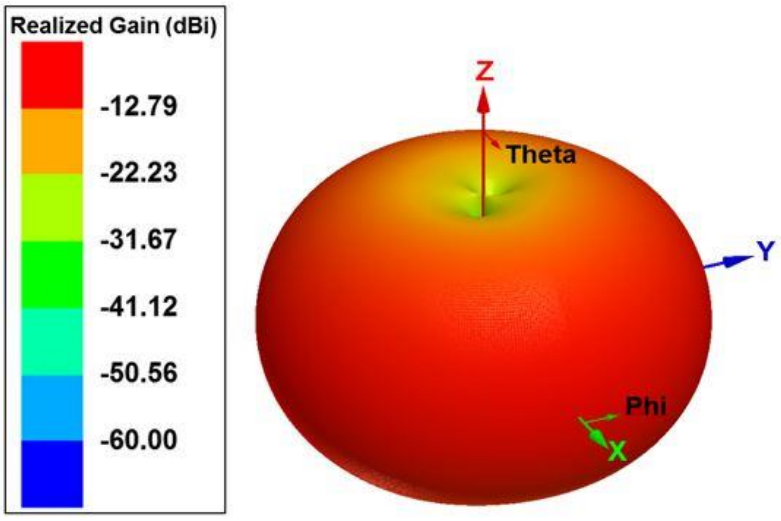

Figure 3.5: Simulated 3D radiation pattern of the proposed antenna.

3.3.2 Antenna Design Optimization and Fabrication

The 180-degree phase shifters, utilizing the optimized rectangular air-core inductors, are applied to a design of the highly miniaturized folded dipole-based antenna at low-VHF band. Fig. 3.4 illustrates the side and top view of the proposed antenna with its equivalent circuit model superimposed over the side view. The lateral dimension and height of the antenna are 10 cm ($0.013\lambda_0$) and 15 cm ($0.02\lambda_0$), respectively. To eliminate dielectric loss from the antenna structure as well as to minimize the antenna's total mass, the open stub is formed by stacking the metallic plates (Rogers RO 4003C substrate with 0.812 mm thickness) without dielectric materials in between. Fig. 3.5 shows the simulated 3D radiation pattern of the proposed antenna with the peak gain of -12.79 dBi at the resonant frequency of 40.01 MHz. The antenna is well matched at resonance when the simulated port impedance of the antenna feed is set to 32 ohms. This impedance matching is achieved by controlling the distance between the vertical posts as the step-

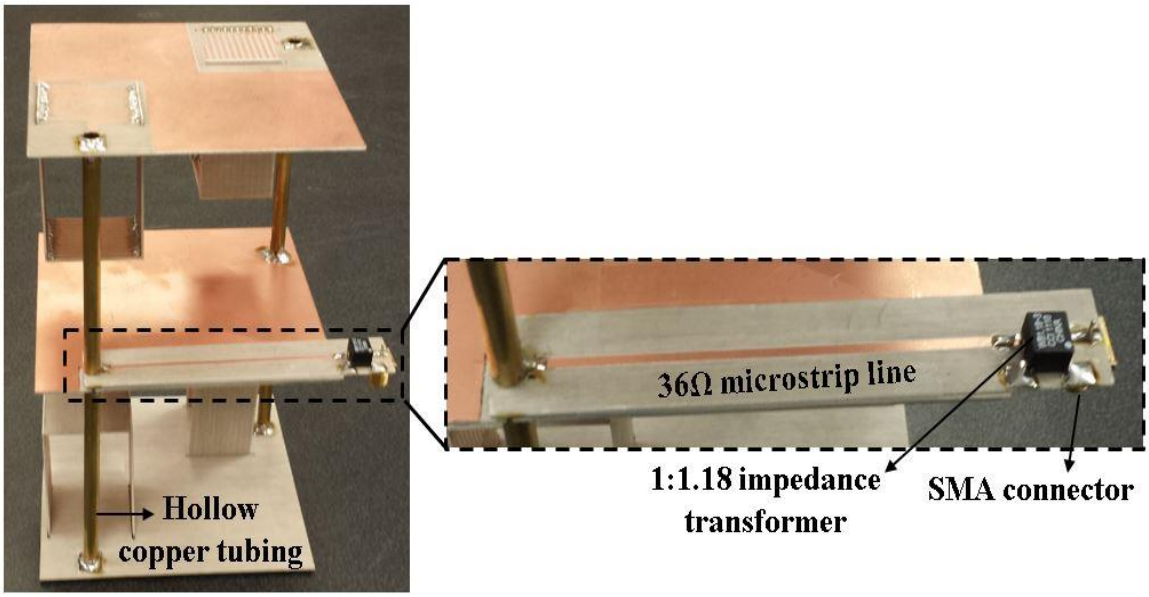

Figure 3.6: The fabricated antenna integrated with the feeding network.

up impedance transformer mentioned earlier and the mutual coupling between each post and air-core inductor. The design also shows a nearly ideal omnidirectional pattern.

Based on the design simulation, an antenna is fabricated and shown in Fig. 3.6. Each side of the rectangular air-core inductor is fabricated on thin substrates and soldered together to integrate the inductor with the antenna. To minimize weight, hollow copper tubing with 5.19 mm diameter is used for the vertical posts. The total mass of the fabricated antenna is 98 grams. An antenna feeding network consisting of a pair of 36-ohm microstrip lines, an impedance transformer (1:1.18) having a maximum insertion loss of 0.5 dB, and a 50-ohm RF coaxial connector is also shown in Fig. 3.6. The 36-ohm lines are placed at a null surface in the middle of the dipole structure, so as not to affect the antenna characteristics, and connected to each feeding post for differential operation. The impedance matching transformer is employed to convert the unbalanced signal provided by the coax to a balanced symmetrical signal for the antenna.

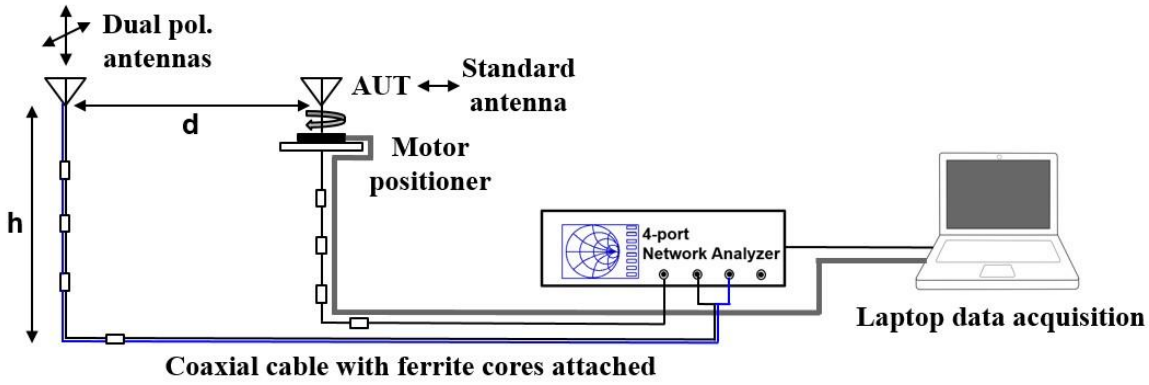

Figure 3.7: Measurement system layout for the antenna characterization.

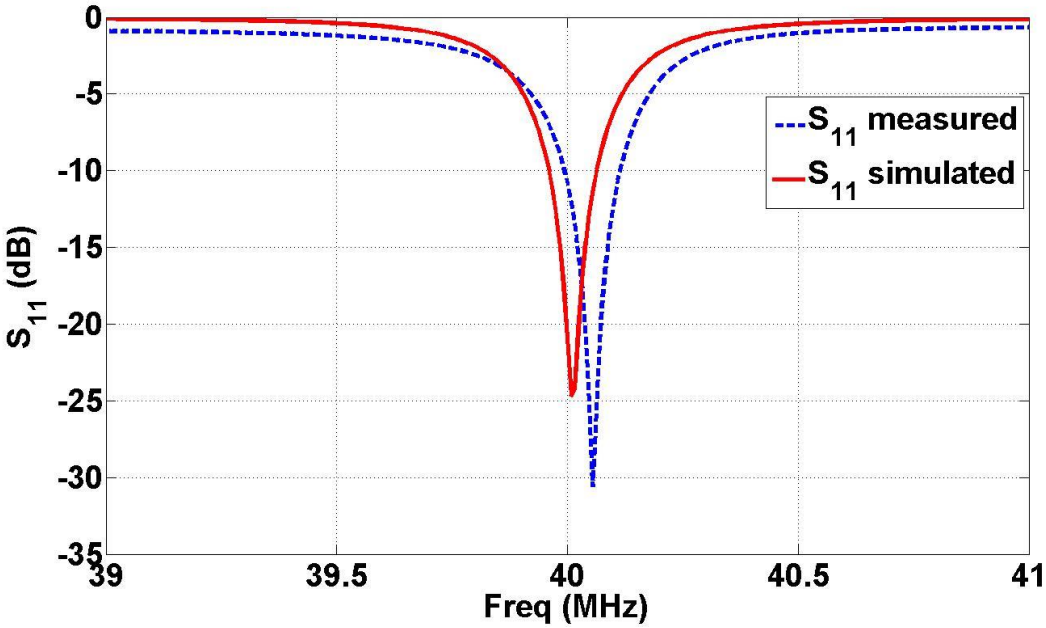

Figure 3.8: Comparison of measured and simulated antenna impedance.

3.4 Measurement and Characterization

To handle the long center frequency wavelength (λ_0=7.5 m at 40 MHz), a measurement setup that can provide nearly free-space conditions in the far-field region is required for accurate antenna characterization. Fig. 3.7 illustrates the measurement system employed. The gain measurement of the antenna under test (AUT) is performed by applying the substitution method using a known

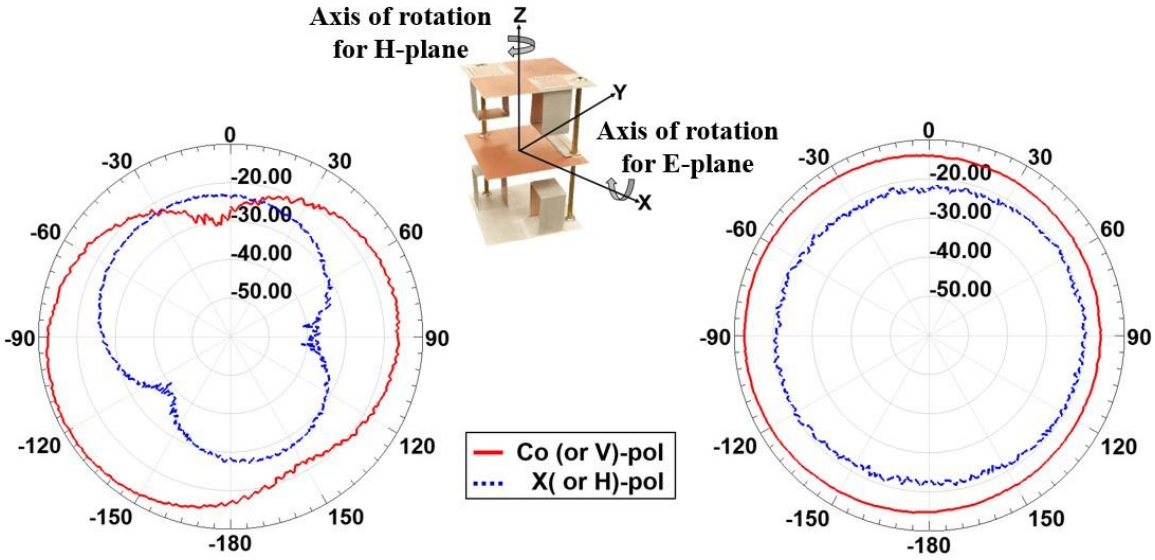

(a) (b)

Figure 3.9: Measured antenna radiation patterns in (a) E-plane and (b) H-plane when a coaxial cable is used to feed the AUT.

standard antenna to obtain calibration data from a vector network analyzer [47]-[48]. Dual biconical antennas for the polarization pattern measurement on the AUT are used as a receive (Rx) antenna and a half-wavelength dipole is used as the standard antenna. Both transmit (Tx) and Rx antennas are positioned on top of the 12-meter (h =1.6λ_0 at 40 MHz) fiberglass tower to minimize the contribution of ground reflection (see Appendix B). Due to the difficulty of stably mounting both antennas far away from each other on the tower, the pattern measurement is carried out in the Fresnel region, which is the radiative near-field, from $\lambda_0/2\pi$ out to one full wavelength. The separation d between Tx and Rx antennas is fixed at $\lambda_0/2$ at 40 MHz.

The input reflection coefficient S_{11} of the antenna is measured separately with a calibrated network analyzer, shown in Fig. 3.8. The resonant frequency of the AUT is measured to be 40.06 MHz which is in agreement with simulation (unlike the previously designed HF antenna that showed the undesirable change in its input impedance from the same method of the measurement [19]). Pattern measurements are conducted for two scenarios: 1) a long (> 12 m) coaxial cable is

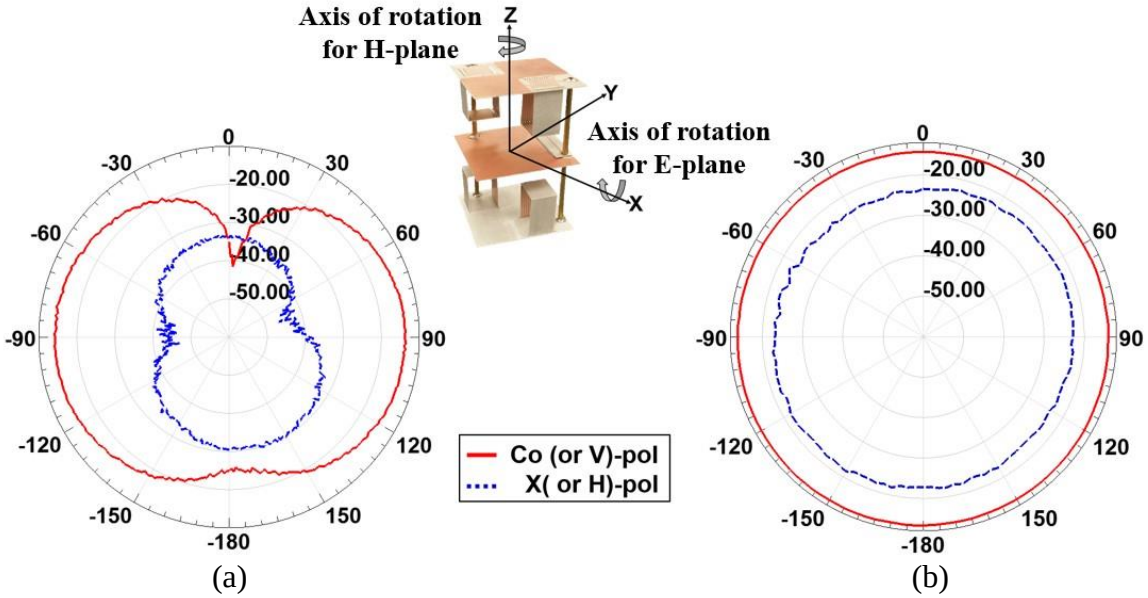

Figure 3.10: Measured antenna radiation patterns in (a) E-plane and (b) H-plane when a small source module is used to feed the AUT.

used to feed the AUT, and 2) a small source module is used for the antenna feed. The two cases are used to investigate the effect of nearby conducting materials such as the feed cable. Fig. 3.9 shows the vertically (co-) and horizontally (cross-) polarized radiation patterns in the E-plane and H-plane with one degree resolution when the coaxial cable is used to feed the AUT. As can be seen in Fig. 3.9, the radiation pattern does not show a fully symmetric dipole-like pattern in the E-plane. Despite the use of ferrite cores attached to the feed for suppressing radiation, small effects of the feed cable are observed in the radiation pattern. To circumvent this problem caused by partial near-field coupling to the feed cable that can excite currents on it which in turn can radiate, a small source module is fabricated, which consists of a voltage controlled crystal oscillator (VCXO), voltage regulator, and battery that can generate an output power of 11 dBm at 40 MHz (see Appendix B). Using this fabricated module for the antenna feed, the radiation pattern of the proposed antenna is remeasured while keeping the other conditions the same. Fig. 3.10 shows the measured radiation pattern in two orthogonal principal planes (E-plane and H-plane). This pattern

Table 3.1
Comparison of antenna performance

	Simulation	With cable	With source module
Center freq.	40.01 MHz	40.06 MHz	40.00 MHz
Peak gain	-12.79 dBi	-12.5 dBi	-13.3 dBi
FBW	0.28 %	0.35 %	·

closely resembles that of a short dipole. The co-polarized radiation pattern is a rotationally symmetric omnidirectional pattern with the maximum gain occurring at $\theta=90°$. While this maximum gain is -13.3 dBi, the gain of the cross-polarized radiation at the same angle is less than -38 dBi. Table 3.1 shows a comparison of antenna performance obtained from simulation and measurements at each operating frequency for each case.

3.5 Summary

A novel, electrically small folded dipole antenna for operation at HF or low-VHF is designed and tested. This design is needed for compact, low-power, mobile wireless applications in highly cluttered environments. The antenna, having dimensions ($0.013\lambda_0 \times 0.013\lambda_0 \times 0.02\lambda_0$ at 40 MHz), is lightweight and provides moderate gain performance in a small form factor. The antenna miniaturization with enhanced radiation efficiency is realized by introducing 180-degree phase shifters bridged between two short dipoles. Employing optimized high-Q rectangular air-core inductors in the phase shifter, the power losses from the antenna are minimized. The antenna was fabricated and measurements validated the design. While the feed cable introduces some small undesired radiation pattern distortion, it has no effect on the antenna resonant frequency. The

proposed antenna is used in practice for low data-rate, low-power communication systems, on small robotic platforms.

CHAPTER IV

Bandwidth Enhancement of Miniature Low-VHF Antennas

4.1 Introduction

Recent studies have shown that low frequencies can be exploited for reliable and persistent communications in complex Army-relevant environments [10]-[11], [24], [28]. To achieve compact, low-power, wireless mobile networking at the lower end of the Very High Frequency (VHF) band, highly miniaturized antennas [19]-[20] have been developed recently. As shown in Fig. 4.1, however, the performances of these miniature antennas are very close to Chu's fundamental limit [49], which means that there is no further gain in terms of bandwidth that one can get with conventional passive matching techniques. In principle, performance of electrically small passive antennas is limited by a gain-bandwidth product [49]-[50]. In order to broaden bandwidth without modifying the antenna dimension while maintaining radiation performance, a non-Foster matching (or active matching) technique can be pursued. Over the past decade, studies on the active matching technique for bandwidth enhancement have been reported in the literature [51]-[52]. In these studies, the technique is applied to unmatched antenna and the antenna performance improvement with the active matching is compared with that of the unmatched and/or the passive matched version of the antenna.

In this chapter, we take a different approach and apply an optimally designed, stable non-Foster matching network directly to the aforementioned passive matched antenna for increasing the

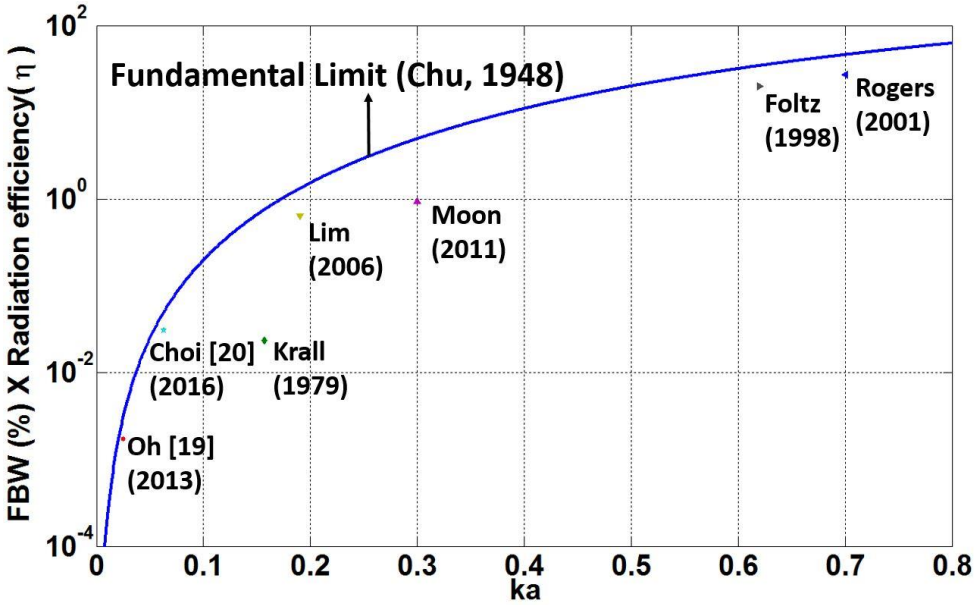

Figure 4.1: Performance comparison of small antennas with respect to their electrical sizes.

effective bandwidth around the resonant frequency of the antenna. A performance comparison of the passive and active versions of the antenna in terms of bandwidth and power efficiency is presented. The proposed active matching technique and its rigorous analysis from circuit simulation are described in Section 4.2. The fabrication of the non-Foster matched antenna and the measurement results are discussed in Section 4.3.

4.2 Proposed Approach and Analysis

4.2.1 Proposed Approach

In [51]-[53], the non-Foster matching techniques are applied to unmatched small monopole or loop antennas. These techniques are implemented with a single negative capacitor and/or a single

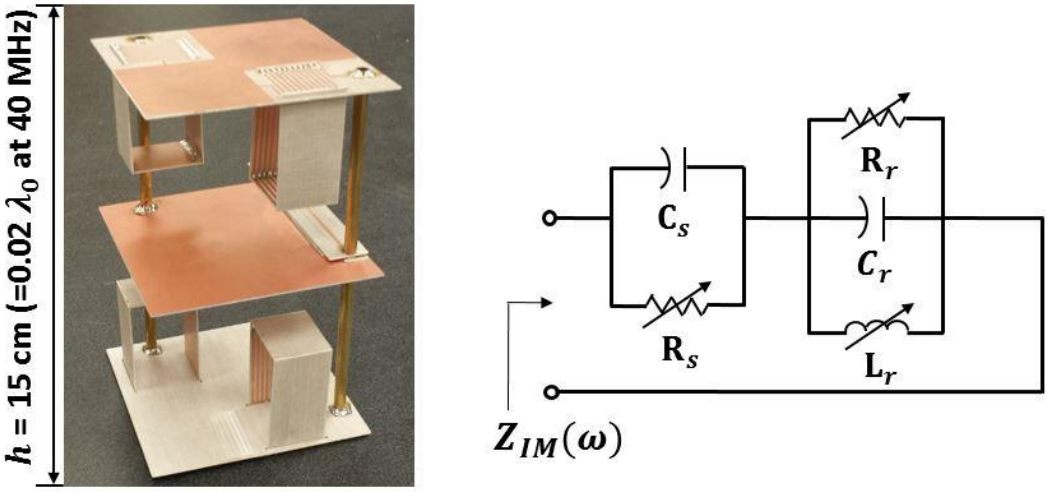

(a) (b)

Figure 4.2: A picture of a short folded dipole and its impedance model $Z_{IM}(\omega)$.

negative inductor produced by a negative impedance converter(NIC) [54] to cancel out the highly reactive components of the antennas over wide frequency range. For the short folded dipole under consideration shown in Fig. 4.2(a) to be matched with non-Foster elements, however, the reactance cancellation cannot be simply performed in the same way since the impedance variation around the resonant frequency makes the design of non-Foster matching network challenging. As mentioned earlier, the aim of our study is to broaden bandwidth of the passive matched small antenna around its resonant frequency. Since the antenna structure is designed to resonate at the low-VHF band (40 MHz) and comprises an impedance transformer as a Balun for differential feeding along with additional impedance matching, its impedance variation with frequency is different from that of unmatched passive antenna. This gives rise to challenging issues in the antenna impedance model and system stability for successful realization of the non-Foster matching network. One of the advantages of this approach is that a single NIC instead of a pair shown in [51] can be used by applying it directly to the antenna Balun, which results in enhanced overall power efficiency.

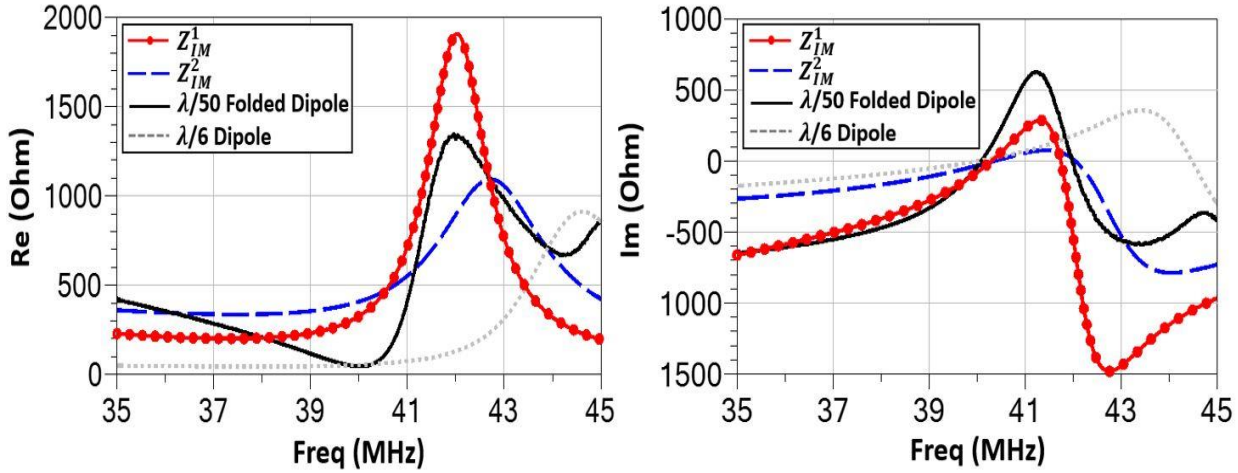

(a) (b)

Figure 4.3: (a) Real and (b) imaginary parts of $Z_{IM}(\omega)$ together with those of the short folded dipole. Impedance of the $\lambda_0/6$ dipole is also plotted for a comparison purpose.

4.2.2 Antenna Impedance Model

The extent of bandwidth enhancement via the proposed non-Foster matching technique critically depends on the design of the antenna impedance model to be inverted over the NIC ameliorating the variation of the antenna impedance around resonance. The short folded dipole ($0.02\lambda_0$ in length at 40 MHz) in Fig. 4.2(a) has a steep variation in the input impedance due to its narrow bandwidth (0.35 % for the voltage standing wave ratio of 2:1). Of course, modeling of such steep variation is not possible with only a single capacitor or inductor. For this reason, the impedance model $Z_{IM}(\omega)$ shown in Fig. 4.2(b) corresponding to the antenna impedance is designed with the following expression:

$$Z_{IM}(\omega) = R_r \parallel j\omega L_r \parallel \frac{1}{j\omega C_r} + R_s \parallel \frac{1}{j\omega C_s}, \tag{4.1}$$

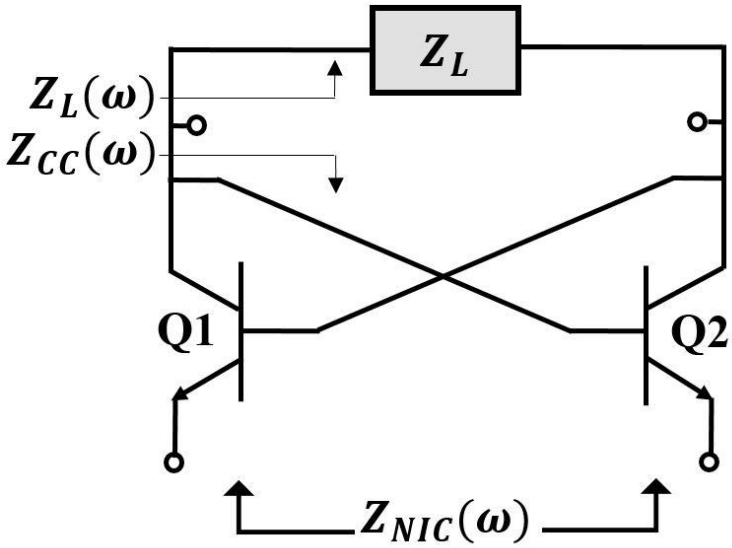

Figure 4.4: Circuit configuration of a Bipolar Junction Transistor (BJT) cross-coupled pair.

where $j = \sqrt{-1}$ and ω is the angular frequency. Fig. 4.3 illustrates the real and imaginary part of Z_{IM} (Z_{IM}^1: $C_S = 8.5\,pF, R_s = 3500\,k\Omega,\ R_r = 1800\,k\Omega, L_r = 239\,nH, C_r = 60\,pF$ & Z_{IM}^2: $C_S = 10\,pF, R_s = 810\,\Omega$, $R_r = 880\,\Omega, L_r = 204\,nH, C_r = 68\,pF$) , together with the measured antenna impedance. The impedance of a larger-sized passive matched antenna ($0.167\lambda_0$ in length at 40 MHz) having smoother variation [55] is also plotted for comparison (see Appendix C). Obviously, the impedance modeling for smaller-sized antennas is more challenging to realize. It should also be mentioned that there is a trade-off between the system stability and the degree of the bandwidth enhancement, and this can be controlled by passive components in (4.1), which will be reviewed in the following section.

4.2.3 Stability Analysis Based on System Sensitivity

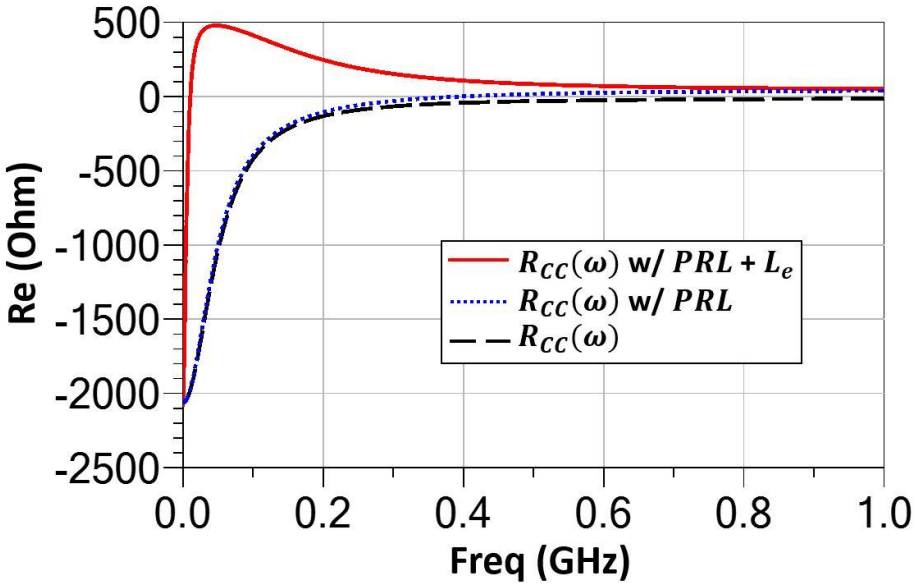

Figure 4.5: Real part of the cross-coupled pair depending on the PRL along the cross-coupled path and L_e in series with an emitter resistor.

The Metal-Oxide-Semiconductor Field-Effect Transistor (MOSFET) or Bipolar Junction Transistor (BJT) cross-coupled pair (see Fig. 4.4) are widely employed for a negative resistance in the design of oscillators or the NIC [54]-[55]. Due to the internal positive feedback of the pair, however, a careful stability analysis for applications of non-Foster matched antenna with the NIC is required to avoid a potential oscillation. A first step toward the analysis is to characterize the impedance of the cross-coupled pair $Z_{CC}(\omega)\left(= R_{CC}(\omega) + jX_{CC}(\omega)\right)$ with a DC biasing circuit as a function of frequency in the small-signal regime. Since the cross-coupled pair generates a negative resistance, $R_{CC}(\omega) < 0$ as shown Fig. 4.5. According to the oscillation conditions for a one-port negative-resistance network [56] when a passive load impedance, represented by $Z_L(\omega) = R_L(\omega) + jX_L(\omega)$, is connected, the net resistance of the network must be positive for the network to be stable:

$$Re[Z_{CC}(\omega) + Z_L(\omega)] > 0 \; or \; |R_{CC}(\omega)| < R_L(\omega). \tag{4.2}$$

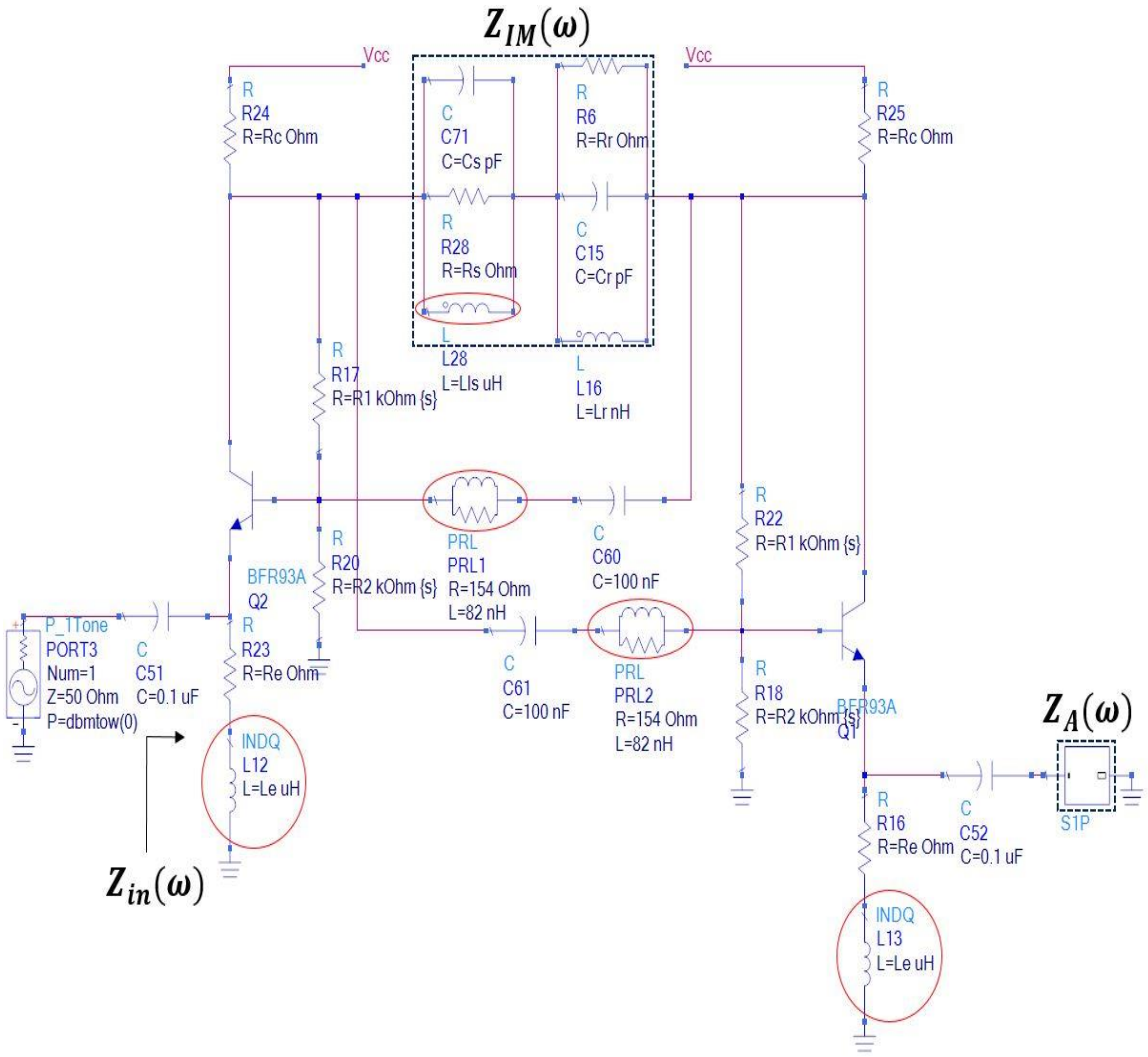

Figure 4.6: A simplified schematic of the non-Foster matching network for a large-signal model analysis.

For our applications, since frequencies of interest are within the low-VHF band (30 MHz – 60 MHz) and $Z_L(\omega)$ corresponds to the aforementioned $Z_{IM}(\omega)$, extra effort is required to satisfy (4.2) over the entire frequency range, which is done as follows. To make $R_{CC}(\omega)$ positive at higher frequencies, the feedback factor along each cross-coupled path is adjusted by adding a parallel inductor-resistor PRL in series with a feedback capacitor. An inductor L_e in series with an emitter resistor is also added at each BJT for the same purpose. With the added components, $R_{CC}(\omega)$ is

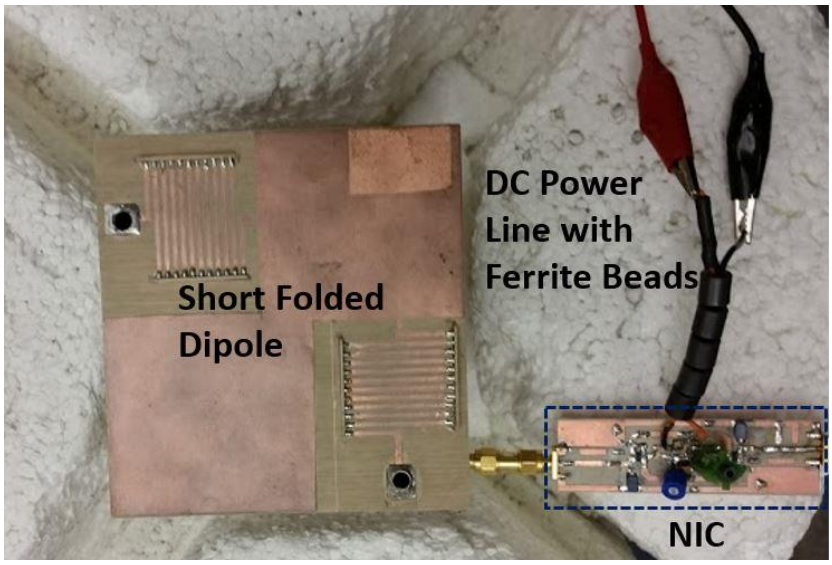

Figure 4.7: A fabricated non-Foster matched antenna on a Styrofoam mount. The single NIC is connected directly to the Balun of the short folded dipole.

now positive above 12 MHz as shown in Fig. 4.5. In order to satisfy (4.2) at lower frequencies, $Z_{IM}(\omega)$ is modified by adding an inductor L_{ls} in parallel with a parallel R_s-C_s in (4.1) to produce high impedance below 12 MHz (see circled components in Fig. 4.6). Under this condition, the stability of the network is determined through the Nyquist stability test in circuit simulation (Keysight ADS 2016). This stability analysis provides a way to take into account tolerances and select the appropriate passive components to avoid circuit oscillations.

The above analysis assumes that the operating point of the BJT in the NIC does not change in the small-signal regime. However, for practical applications of the non-Foster matched antenna, a large-signal analysis should be performed to take into account nonlinear effects of the BJT with respect to large AC signals and variations in power supply values. Fig. 4.6 illustrates a simplified schematic of the non-Foster matching network for the large-signal S-parameter simulation. Here, $Z_{in}(\omega)$ represents a sum of the impedance of the floating NIC, $Z_{NIC}(\omega)$ (see Fig. 4.4), and the measured antenna impedance, $Z_A(\omega)(= R_A(\omega) + jX_A(\omega))$. The total loop resistance in this setup

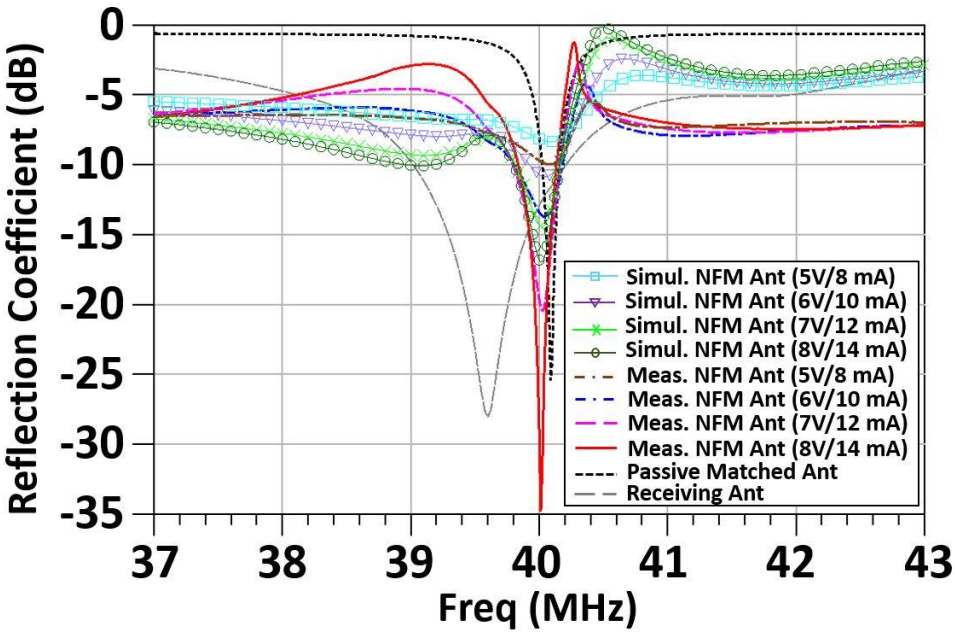

Figure 4.8: Measured reflection coefficients as a function of power supply value. The simulation results are also plotted together.

must also be positive in order to avoid oscillations. Simulated results along with measured data will be discussed in the next section.

4.3 Implementation and Discussion

Based on the simulation analysis, a non-Foster matching network is designed and fabricated. Considering system sensitivity due to component tolerance, mechanically tunable elements for the antenna impedance model $Z_{IM}(\omega)$ are utilized in the NIC. The fabricated NIC is connected directly to the antenna Balun along the null plane bisecting the antenna structure (see Fig. 4.2). This ensures that introducing the NIC does not affect the characteristics of the passive antenna such as the input impedance and radiation pattern [20]. Furthermore, multiple ferrite beads are used in series with a DC power line for high frequency noise and parasitic suppressions and a

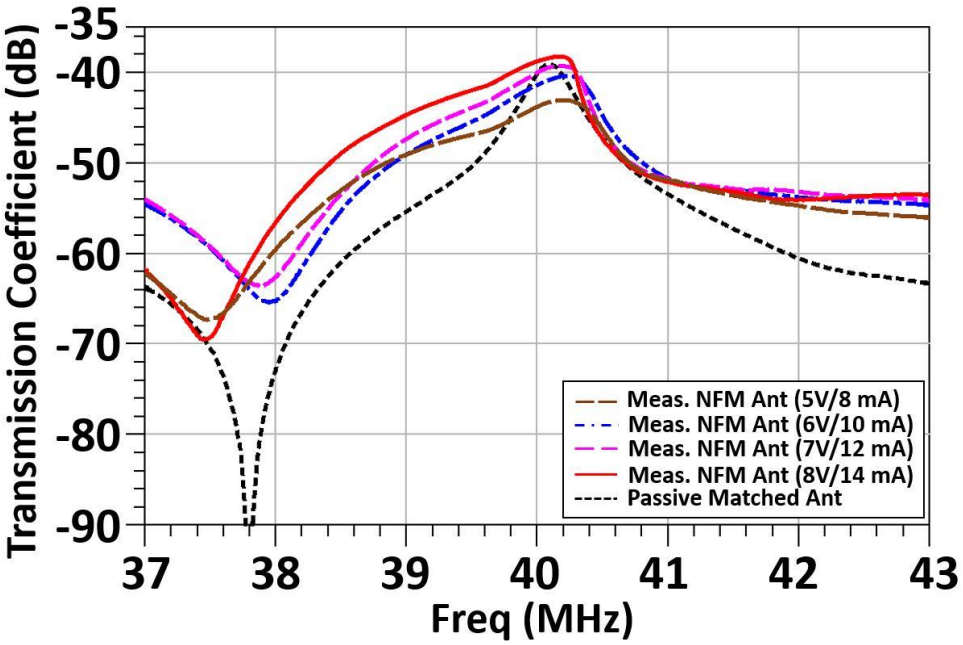

Figure 4.9: Measured transmission coefficients as a function of power supply value. A fabricated $\lambda_0/5$ dipole is used as a receiving antenna.

coaxial feed cable for suppressing common mode current flowing on the outer conductor of the coax.

The fabricated non-Foster matched antenna is characterized using a vector network analyzer in a laboratory setting. As alluded to earlier, large-signal measurements as a function of input power and power supply voltage are performed allowing for nonlinear behaviors of the BJTs in the NIC. Given that the applications of interest for the non-Foster matched antenna is low-Power, compact, wireless transmission systems, we first set the input power level at 7 dBm which corresponds to a transmit power of the low-VHF radio in [24]. By sweeping a power supply voltage with the fixed input power, reflection coefficients of the non-Foster matched antenna are measured and compared with the simulated ones as shown in Fig. 4.8. A transmission coefficient corresponding to each reflection coefficient with the given power supply voltage is also measured (see Fig. 4.9). For this measurement, a fabricated dipole having a length of $0.2\lambda_0$ at 40 MHz is

Table 4.1
Comparison of antenna performance (passive vs. active)

Antenna Size	Matching Type	3 dB Power BW	η_{adv} (in the BW)
10 cm × 10 cm × 15 cm	Passive	0.87 %	1.3 to 5.9
	Active	2.15 %	·

used as a receiving antenna. Furthermore, as stated before, the nonlinear effects of the BJTs in the NIC on the non-Foster matching is considered since the cross-coupled pair properly operates as a NIC in the small-signal regime where the input AC signal is small compared to the DC bias. By measuring the input impedance of the non-Foster matched antenna as a function of input power with a fixed DC bias (not shown here), the nonlinear effects are also examined. In view of the results, the impedance of the cross-coupled pair is altered due to the nonlinearity of the open-loop gain of the BJTs, which results in the variations in the input impedance of the overall system with DC bias or input power sweep.

Since the non-Foster matched antenna requires DC power to operate the NIC, overall power efficiency should be considered to evaluate effectiveness of the proposed approach against the passive matched one in actual applications. Assuming the measurement conditions do not change aside from the antenna matching type, we define a power efficiency advantage η_{adv} as

$$\eta_{adv} = \frac{|S_{21(AM)}|^2}{|S_{21(PM)}|^2} \cdot \frac{P_{DC(PM)}}{P_{DC(AM)}}, \tag{4.3}$$

where $S_{21(AM)}$ and $S_{21(PM)}$ are measured transmission coefficients with the active and passive matching, respectively, $P_{DC(AM)}$ is the DC power required for a transmitter and NIC for the active matching, and $P_{DC(PM)}$ is the DC power required for a transmitter for the passive matching. In consideration of the transmitting system shown in [24], P_{DC} for the transmitter is set to be 3.3 V/ 240 mA. P_{DC} for the NIC is chosen to be 8 V/ 14 mA. Under these conditions, effective power bandwidth with $\eta_{adv} > 1$ is 2.15 % with the active matching. The performance comparison between passive and active matching is summarized in Table 4.1.

4.4 Summary

An electrically small non-Foster matched folded dipole at low VHF is designed and tested. A single NIC instead of a pair to enhance overall power efficiency is applied to the passive matched version for the active matching. Stability analysis of the NIC with a designed impedance model of the antenna is conducted through circuit simulation. The non-Foster matched antenna is fabricated and its performance is measured and compared with that of the passive antenna. The results show 3 dB power bandwidth with a power efficiency advantage is improved by more than a factor of two with the active matching. Thus, the non-Foster matched antenna with the enhanced bandwidth is effective for lower-power, short-range low-VHF transmission systems with higher channel capacity while maintaining their compactness.

CHAPTER V

An Effective Characterization Technique for Low-VHF Antennas

5.1 Introduction

Accurate measurement of fundamental antenna parameters such as input impedance, bandwidth, radiation pattern, and gain is very important for all applications. Knowledge of the actual antenna performance plays an important role in designing real-world wireless communication or radar systems. The simplest way to characterize antennas is of course the direct far-field measurement that can be accomplished in outdoor ranges or in anechoic chambers [20], [43], [47]. The use of such techniques with low frequency antennas operating at HF or low VHF bands is limited by a number of factors. At these frequencies, the sizes of anechoic chambers and the absorbers become prohibitively large. Outdoor ranges require a vast space and tall towers, and the effect of ground must be carefully examined for accurate measurements. Special approaches to measure HF and VHF antennas have been reported in [57]-[62]. These involve scale modeling, utilization of aircraft-towed transmitters in antenna measurements, design of ground-reflection ranges to minimize the contribution of reflection from the ground, and near-field scanning. All of these require substantial time and effort to perform the measurements as well as a specially designed very-large, expensive anechoic chamber in the case of indoor measurements.

In order to circumvent these difficulties, a non-intrusive near-field measurement system [63] using an all-dielectric and very small electro-optical probe is presented in this chapter. The advantage of the EO probe is that it can be placed very close to the antenna surface where the near field is very strong. For a non-metallic room that is sufficiently larger than the antenna and for the antenna sufficiently away from obstacles in the room, the use of absorbers is not critical. The criteria for setting object distances from the antenna is established by monitoring the reactive part of the antenna input impedance as antenna height above ground is changed and nearby obstacles are pushed away from the antenna surrounding. Once a stable condition for the reactive part of the input impedance is observed, it is assured that the field distribution over the surface of antenna is dominated by the direct signal. Also at low frequencies, reflection and scattering from dielectric walls and objects are rather low. Hence, the contribution from multi-path signal on the probe is significantly smaller than the very strong near field of the antenna. Conventional probes, such as loops, short diploes, or open-ended waveguides, which make use of metallic structures together with their connected transmission lines, can significantly perturb the current distribution on the antenna if they are brought to very close proximity of the antenna. This is particularly the case if the AUT is electrically small whose dimensions are comparable to those conventional probes. Unlike the conventional metallic probes, the EO probe with a very small tip of less than $1mm^3$ connected to very thin fiber optics does not perturb the excited currents on the antenna. The EO probe used here is also very broadband and can be applied for all frequencies of interest up to and beyond millimeter-wave band. Furthermore, the computationally complicated probe compensation process [64]-[65] is not required since the EO probe measurement is non-radiative.

In [66]-[67], near-field to far-field transformation for arbitrary enclosing near-field surfaces have been proposed. These approaches, however, provide only an approximate solution under the

assumption that the radii of curvature of the surface at every point is much larger than the wavelength. Similar to our approach, they place a perfect electric conductor (PEC) over the aperture of the antenna with a surface magnetic current proportional to the measured tangential electric field. Then they apply image theory that is only valid for infinite ground plane to remove the PEC and double the surface magnetic current. This is only a good approximation if the local radii of curvature over the arbitrary surface is very large compared to the wavelength. If cubic surfaces are used the edges do not satisfy this condition. In fact, there is significant edge current on the PEC, which cannot be ignored. It is noted here that the dimension of the box for the problem at hand is only a fraction of the wavelength and image theory cannot be applied here. In this chapter, a novel exact near-field to far-field transformation for all types of antennas without truncation errors regardless of the size of the scanned area is presented. For this approach, only the tangential components of the electric field over an arbitrary closed surface encompassing the AUT are required. The reciprocity theorem in conjunction with the induced surface current excited by a plane wave on a metallic surface in place of the scanned enclosing surface is used. The induced surface electric current density illuminated by an incident plane wave in a desired direction over the metallic surface is calculated using a full-wave numerical simulation. Using the reaction theorem, the radiated field in a desired direction is computed as will be shown later. The validity of this antenna characterization technique is demonstrated utilizing a recently developed miniaturized folded dipole antenna at low-VHF band [19]-[20]. The computed antenna parameters from the proposed technique are compared with those obtained from direct far-field measurement in a special elevated range and full-wave electromagnetic (EM) simulation. In Section 5.2, the EO-based near-field approach is presented. In Section 5.3, a new formulation for near-field to far-field

transformation applicable for arbitrary shape scanned surface is provided. Section 5.4 presents the measurement calibration and validation of the proposed approach.

5.2 Electro-Optical Near-Field Measurement

Non-intrusive, high-resolution, near-field measurement is of interest for number of applications including RF circuit diagnostics, EMC/EMI testing and antenna characterization. Despite the existence of many near-field radiation pattern characterization methods, as will be shown here, there are a number of important advantages for non-intrusive and high-resolution near-field sampling that EO measurements can provide [68]-[69]. One such advantage pertains to the measurement of antennas at low frequencies. For applications such as source tracking [12] and reliable communication in complex environments [10]-[11], an extremely small and lightweight antenna operating at low-VHF band has been developed as shown in the previous chapter. For this antenna, pattern and gain measurements were carried out in an outdoor elevated range with non-metallic towers. A standard far-field measurement setup, in which both the transmitting and the receiving antenna are mounted on top of a tall fiberglass tower ($>$12 m), was used to create nearly free-space conditions in the far-field region. For this measurement, considerable efforts are needed because of the cumbersome antenna setup and scanning. The height of AUT above ground must also be chosen to be much larger than the transmit and receive antennas separation to minimize the effect of ground reflection. Uncontrollable environmental conditions such as rain, wind, and temperature variations also add to the complexity of the elevated-range measurement. Furthermore, for small antennas the effect of the feed cables on the antenna impedance and radiation pattern is a major issue and was observed during the measurement. A small, battery-operated source module had to be designed and connected directly

to the antenna in the elevated range to avoid the effects of the long cables. The complexity in such measurements necessitates development of an alternative approach that is more accurate and time- and cost-effective.

Near-field scanning systems are developed as an alternative to the cumbersome outdoor far-field range or costly anechoic chamber facilities. However, conventional near-field scanning systems have substantial disadvantages at low frequencies. These systems are traditionally designed for antennas operating at microwave frequencies and higher with large apertures to circumvent the challenges associated with satisfying the far-field requirement. As alluded to before the standard probes for near-field systems are small metallic antennas or apertures for picking up the near fields of the AUT. Such metallic probes and the associated transmission lines connected to them cannot be placed very close to the AUT, as they can significantly modify the current distribution on the antenna and thereby would distort the measured near field distribution. These probes are also band limited and have a relatively large physical dimension at low frequency. For conventional near-field systems, the minimum distance between the probe and the AUT is the far-field distance of the small probes. This minimum distance oftentimes is larger or comparable to the wavelength. For a short dipole, for example, requiring the ratio of the radiating term to the largest non-radiating term to be larger or equal to 10, the far-field distance is computed to be $1.6\lambda_0$. Even if we were to relax the radiating to non-radiating terms ratio to be larger than three the minimum distance must still be larger than $0.6\lambda_0$. Obviously, for an AUT that operates at low-VHF band or lower, this distance amounts to many meters. In [62], for instance, a spherical near-field system in VHF range in a large rectangular anechoic chamber with pyramidal absorber is introduced. The probing distance in the system is large (2 meters) due to the use of conventional metallic probe consisting of two resistively loaded crossed dipoles, each 40 cm in length. For the

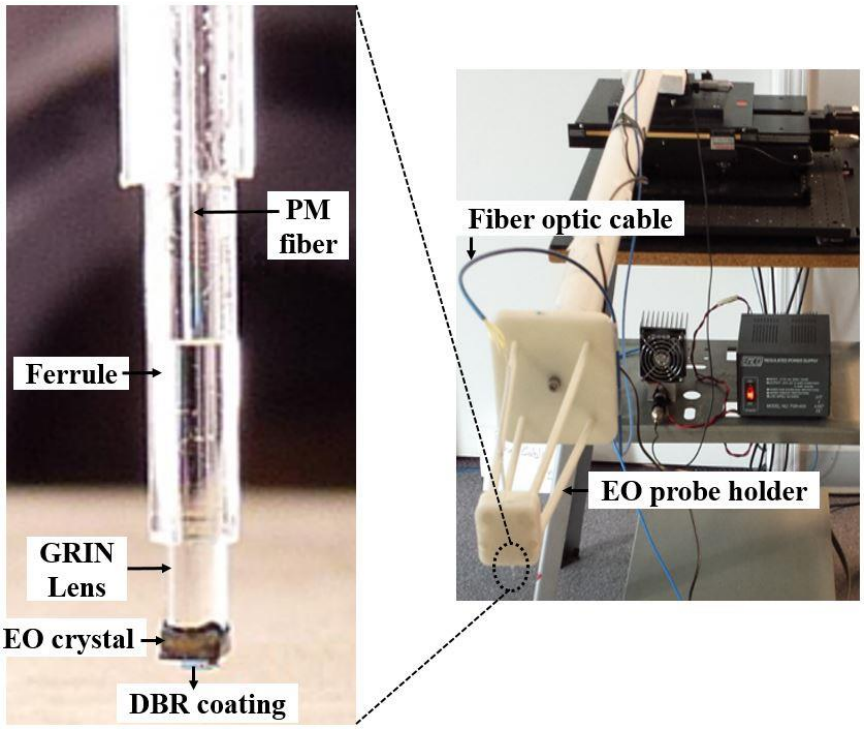

Figure 5.1: A fiber-based electro-optic probe structure used in our measurement system.

general near-field antenna measurement applications of EO probes, in addition to the non-intrusive nature of EO probes, it should be mentioned that probe compensation process is not required [68], [70].

The system employed for this research is a commercial measurement system, called NeoScan, developed by EMAG Technologies. It provides significantly superior performance to the conventional near-field scanning systems as described before. This system operates based on Pockels effect, which measures the phase retardance of an optical beam through a small crystal immersed within an RF electric field [71]. This EO effect provides a means for modulating the polarization of the optical beam, which makes it possible to detect the presence of an electric field impinging on a very small crystal ($1\ mm \times 1\ mm \times 1\ mm$) of the EO probe in the system. The EO field probe is all dielectric with no metallic components and can be used to measure the electric

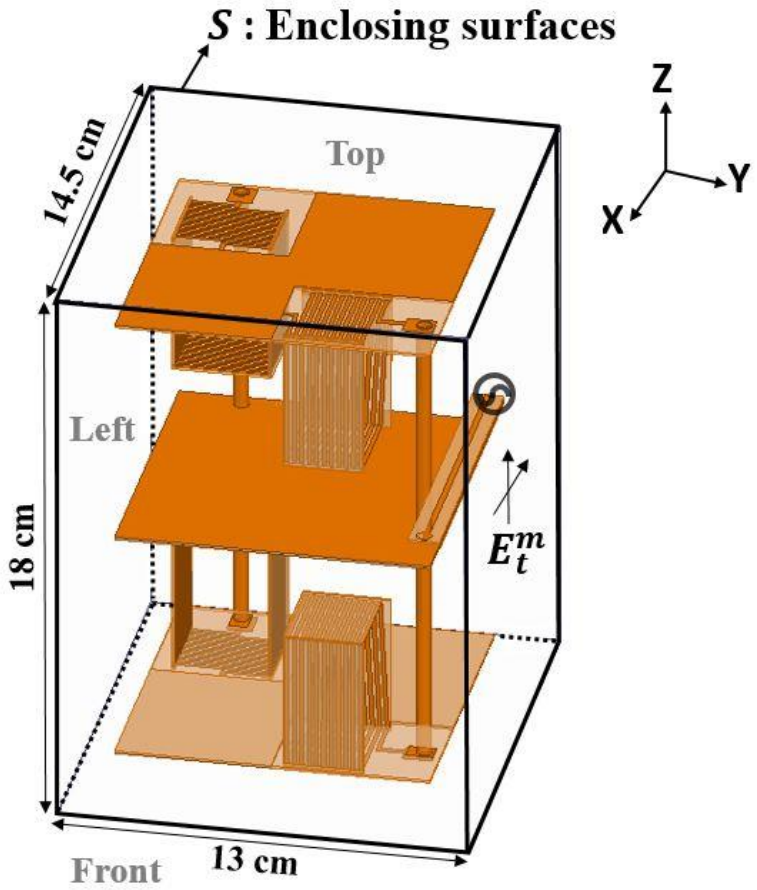

Figure 5.2: An imaginary rectangular box composing six scanned surfaces is centered at the origin of a Cartesian coordinate system whose axes are parallel to the edges of the box.

fields with extremely small spatial resolution (minimum sampled space $< 10\ \mu m$ corresponding to the focused laser beam within the EO crystal). These probes can be brought to the very-near-field region of the antenna where the fields are very strong. Another advantage of the EO probe is an extremely wide bandwidth (3 MHz – 100 GHz or higher). The probe can be calibrated to measure the absolute magnitude and relative phase of electric fields over a wide dynamic range (0.1 V/m – 1 MV/m). Fig. 5.1 shows the picture of the EO probe used in our measurements.

5.3 3-D Near-Field to Far-Field Transformation

Based on uniqueness theorem, the fields outside a region enclosing the sources of the electromagnetic field can be uniquely determined if the tangential electric or magnetic field over the enclosing surface is known. Suppose that the tangential electric field of an AUT over an arbitrary surface enclosing the antenna is measured by the EO probe of NeoScan. Far-field quantities can then be calculated employing the radiometrically calibrated values of the measured near fields. The geometry of a small antenna enclosed by surface S is shown in Fig. 5.2. For this problem the measured tangential electric field is represented by $\boldsymbol{E}_t^m(\boldsymbol{r})$. To calculate the field outside S using just the tangential electric field, the field equivalence principle can be invoked [72]. In this approach we assume the fields inside S are zero and introduce instead fictitious surface electric and magnetic currents proportional to the tangential magnetic and electric fields. Since the tangential magnetic field components are not available, the surface S may be replaced by a PEC, over which the surface magnetic current is placed. Thus, the problem is reduced to finding the total field radiated from the magnetic current in the presence of the PEC box having the same surface as *S*. The magnetic current is given by:

$$\boldsymbol{J}_m^m = -\hat{n} \times \boldsymbol{E}_t^m, \tag{5.1}$$

where $\hat{n}$ is a unit vector directed normally outward from S, and $\boldsymbol{E}_t^m$ is the electric field generated by the AUT over S.

Of course, for such problems and arbitrary *S*, an exact analytical solution does not exist. For a rectangular box, for example, one may resort to an approximate analytical solution using image

theory. That is, assuming the PEC box consists of electrically large flat sides, the image theory can be applied by doubling the magnetic current on the sides of the enclosing rectangular box and then computing the radiating field in the absence of the box using the planar near-field to far-field transformation [73] for all six surfaces. This approach ignores the truncation effects and can introduce significant error when the dimensions of the box are small or comparable with the wavelength. To resolve this issue, an alternative method based on numerical simulations and the reciprocity theorem is introduced.

Consider the rectangular cuboid as the enclosing surface S centered at the origin of a Cartesian coordinate system whose axes are parallel to the edges of the cuboid. Using the source equivalence principle, the rectangular cuboid surface is made into a PEC surface. Now let us suppose that the metallic cuboid is being illuminated by the fields of an infinitesimal magnetic dipole located at the observation point in the far-field region at a distance r_0 from the origin and at an orientation denoted by θ and ϕ. The volumetric magnetic current distribution for this source can be written as

$$\boldsymbol{J}_{\mathrm{m}}^{\mathrm{b}} = \hat{p}\,\delta(\mathbf{r}-\mathbf{r}_0), \tag{5.2}$$

where $\hat{p}$ is a unit vector along the dipole, r is the radial distance from the origin, and $\delta(\mathbf{r}-\mathbf{r}_0)$ is a delta function. The far-field expression for the radiated field from the infinitesimal dipole at a point around the origin can be found from

$$\boldsymbol{E}_i^{\mathrm{b}} = \frac{ik}{4\pi}\frac{e^{ikR}}{R}\hat{p}\times\hat{R}, \tag{5.3}$$

where k is the angular wavenumber given by $k = 2\pi/\lambda_0$ and

$$R = |\boldsymbol{r} - \boldsymbol{r}_0| \approx r_0 - \boldsymbol{r} \cdot \hat{r}_0 \tag{5.4a}$$

$$\hat{R} = \frac{\boldsymbol{r}-\boldsymbol{r}_0}{|\boldsymbol{r}-\boldsymbol{r}_0|} \approx -\hat{r}_0 \tag{5.4b}$$

$$\hat{r}_0 = sin\theta cos\phi\hat{x} + sin\theta sin\phi\hat{y} + cos\theta\hat{z}. \tag{5.4c}$$

Upon inserting (5.4a) and (5.4b) into (5.3), we have

$$\boldsymbol{E}_i^{\mathrm{b}} = \frac{-ik}{4\pi}\frac{e^{ikr_0}}{r_0} e^{-ik\hat{r}_0\cdot\boldsymbol{r}} \hat{p} \times \hat{r}_0. \tag{5.5}$$

In a similar manner, it can be shown that

$$\boldsymbol{H}_i^{\mathrm{b}} = \frac{-ik}{4\pi\eta_0}\frac{e^{ikr_0}}{r_0} e^{-ik\hat{r}_0\cdot\boldsymbol{r}} (\hat{p} \times \hat{r}_0) \times \hat{r}_0, \tag{5.6}$$

where $\eta_0 = \sqrt{\mu/\varepsilon}$ is the free space characteristic impedance. Applying the reaction theorem [74] to the surface and volumetric magnetic currents given by (5.1) and (5.2) leads to

$$\iint_S \boldsymbol{H}^b(\boldsymbol{r}) \cdot \boldsymbol{J}_m^m(\boldsymbol{r}) d\boldsymbol{s} = \iiint \boldsymbol{H}(\boldsymbol{r}) \cdot \boldsymbol{J}_m^b(\boldsymbol{r}) dv, \tag{5.7}$$

where $\boldsymbol{H}^b(\boldsymbol{r})$ is the total magnetic field (incident plus scattered) generated by the infinitesimal magnetic current source on the surface of the enclosing PEC box. Also, $\boldsymbol{H}(\boldsymbol{r})$ is the radiated field from the AUT. Here we have used the fact that the tangential component of the total electric field

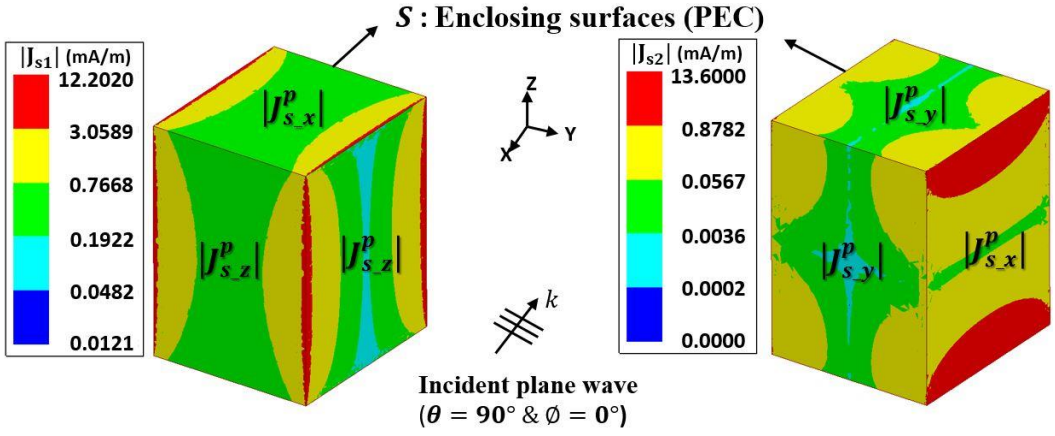

(a) (b)

Figure 5.3: Magnitudes of the induced surface electric currents on the PEC enclosure S, illuminated by an incident plane wave at a given direction ($\theta = 90° \,\&\, \emptyset = 0°$).

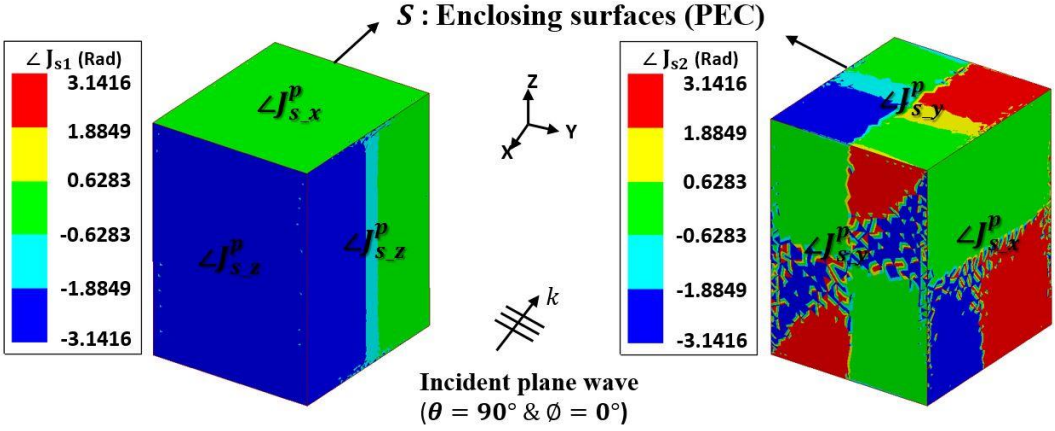

(a) (b)

Figure 5.4: Phases of the induced surface electric currents on the PEC enclosure S, illuminated by an incident plane wave at a given direction ($\theta = 90° \,\&\, \emptyset = 0°$).

$\hat{n} \times \boldsymbol{E}^b(\boldsymbol{r})$ is equal to zero on the surface according to the boundary condition over PEC surfaces such that the surface integral of its term over the box disappears.

Using (5.1) and (5.2) in (5.7), the radiated magnetic field from the AUT can be calculated from

$$\hat{p} \cdot \boldsymbol{H}(\boldsymbol{r}_0) = -\iint_S \boldsymbol{H}^b(\boldsymbol{r}) \cdot \hat{n} \times \boldsymbol{E}^m(\boldsymbol{r}) d\boldsymbol{s}. \tag{5.8}$$

Noting that $\hat{n} \times \boldsymbol{H}^b = \boldsymbol{J}_S^b(\boldsymbol{r})$ is the induced electric current on the surface of the PEC enclosure,

$$\hat{p} \cdot \boldsymbol{H}(\boldsymbol{r}_0) = \iint_S \boldsymbol{E}_t^m(\boldsymbol{r}) \cdot \boldsymbol{J}_s^b(\boldsymbol{r}) d\boldsymbol{s}. \tag{5.9}$$

Hence, the radiated magnetic field in the direction of $\boldsymbol{r}_0$ can easily be attained from the measured tangential electric field and the calculated induced surface electric current density over the PEC box. To further simplify calculation of $\boldsymbol{J}_S^b(\boldsymbol{r})$, plane wave excitation instead of the magnetic dipole source may be considered. This can be done since the infinitesimal magnetic dipole is in the far-field region of the AUT. Accordingly, the incident electric field given by (5.5) can be locally regarded as a plane wave. Denoting the induced surface current on the PEC enclosure from an incident plane wave with intensity 1 V/m and polarization $\hat{p} \times \hat{r}_0$ propagating along $-\hat{r}_0$ by $\boldsymbol{J}_S^p(\boldsymbol{r})$, (5.9) can be written as

$$\hat{p} \cdot \boldsymbol{H}(\boldsymbol{r_0}) = \frac{-ik}{4\pi} \frac{e^{ikr_0}}{r_0} \iint_S \boldsymbol{E}_t^m(\boldsymbol{r}) \cdot \boldsymbol{J}_s^p(\boldsymbol{r}) d\boldsymbol{s}. \tag{5.10}$$

It is noted that $\boldsymbol{J}_S^p(\boldsymbol{r})$ can be computed analytically for canonical enclosures such as spheres and cylinders or numerically for the others using a standard full-wave approach. Fig. 5.3 and 5.4 show an example of the computed induced surface electric current density over the PEC enclosure in terms of magnitudes and phases when a plane wave with intensity of 1 V/m at $\theta = 90^\circ$ and $\emptyset = 0^\circ$ is incident on S. Similarly, by computing all the induced surface currents as a function of θ and ϕ, and then applying them into (5.10) with the measured very-near fields, the radiated electric field

($\boldsymbol{E} = \eta_0 \boldsymbol{H} \times \hat{r}_0$) from the AUT are calculated. Here, numerical calculation of the integrals in (5.10) is performed based on trapezoidal method of integration [75].

The antenna gain can be computed since the value of the electric field and the input power P_{in} to the AUT are available. First, the radiation intensity $U(\theta, \emptyset)$, defined as the power radiated from an antenna per unit solid angle, is evaluated from the calculated far field. Defining electric-field intensity $\boldsymbol{E}(r)$ of the AUT at the far-field region as

$$\boldsymbol{E}(r) = \frac{e^{-jkr}}{r}\left[F_\theta(\theta, \phi)\hat{\theta} + F_\phi(\theta, \phi)\hat{\phi}\right], \tag{5.11}$$

where $F_\theta(\theta, \phi)$ and $F_\phi(\theta, \phi)$ are the radiated electric field strength from the AUT in the (θ, ϕ) direction, the antenna gain G can then be expressed as [44]

$$G = \frac{4\pi U(\theta,\emptyset)}{P_{in}}, \tag{5.12}$$

where $U(\theta, \emptyset) = \frac{1}{2\eta_0}\left[|F_\theta(\theta, \phi)|^2 + \left|F_\phi(\theta, \phi)\right|^2\right]$.

5.4 Measurement Calibration and Validation

In order to maintain the accuracy and reliability of very-near-field antenna measurements, the field probe system must remain stable over the entire measurement period. Stabilization of the EO probe in our system is consistently monitored by a Managing Program developed with a system design software (National Instruments LabVIEW 2011) while the probe scans near fields of the

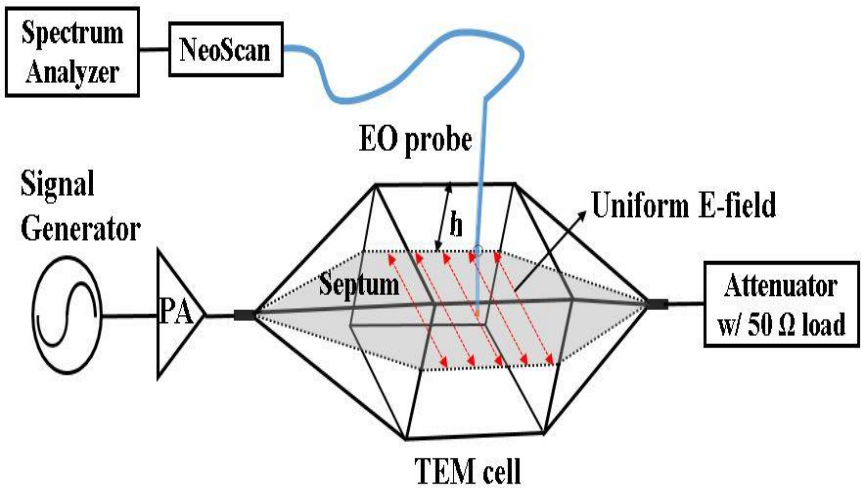

Figure 5.5: Experimental schematic of the EO probe calibration system utilizing a standard TEM cell.

AUT. In order to achieve the maximum EO signal at a given condition for the best probe sensitivity, a system optimization procedure is also conducted (see Appendix D). This involves determining a stable optimal bias point applied to a polarization controller consisting of four dynamic retardation plates in NeoScan, which is utilized to control a polarization state of the optical beam in the fiber.

The EO system directly measures the intensity of modulated optical beams due to the variation of the RF electric field signals. To obtain the absolute value of the electric field, the probe has to be calibrated against a known field. In other words, the probe calibration is used to find the linear relationship between the measured signal power from the system output and the electric field intensity at the probe tip. This calibration can be performed using a standard transverse electromagnetic (TEM) cell in which a known and uniform electric field is established [76]-[77]. In the cell, since the field strength is related to the net input power produced by an RF source, the electric field in terms of the input power can be calculated [78]. Thus, the EO probe can be calibrated by sensing the known fields for a certain RF input power. As shown in Fig. 5.5, in our

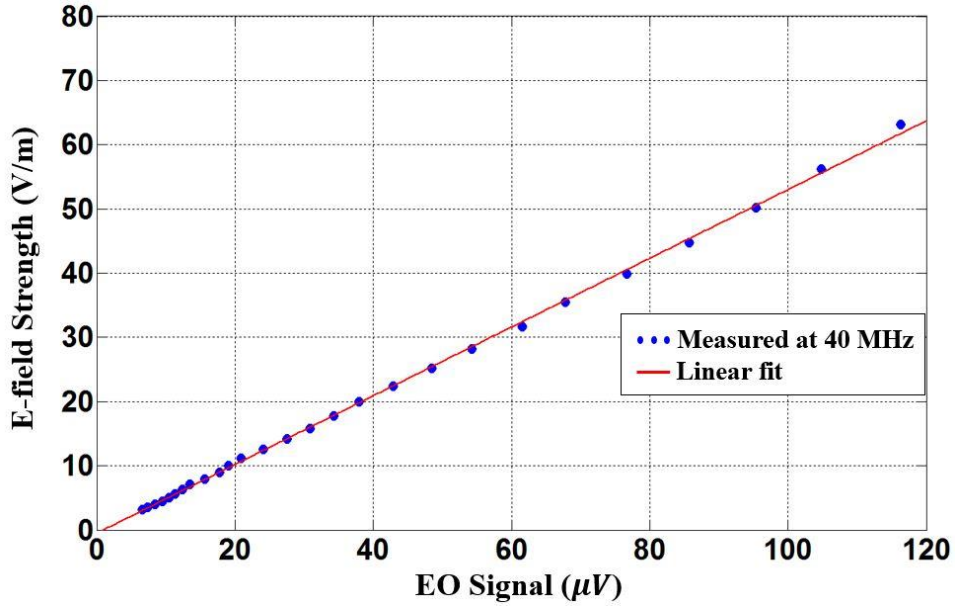

Figure 5.6: Actual electric field strength corresponding to its EO signal captured by the EO field probe. This graph shows a linear relationship between them.

calibration setting a uniform electric field is linearly polarized in a direction parallel to the septum in the TEM cell. Therefore, by aligning the axis of the EO crystal at the tip of the probe so as to sense horizontally polarized fields and then by placing the probe in the center of the test region through a small hole in the top wall of the cell, the probe is calibrated for the correct polarization. A power amplifier (PA), which can provide a continuous-wave output power up to 20 Watts, is utilized to characterize the EO probe over a wide dynamic range. The EO signals measured using a spectrum analyzer versus the calculated electric field strength corresponding to the net power in the cell at 40 MHz (the center frequency of AUT) are presented in Fig. 5.6. The calibration slope shows a good linear relation between the EO signal in μV and the electric field intensity in V/m. This linearity can be denoted by $E = \alpha V$, where α is the calibration coefficient.

To demonstrate the unique capability of the EO-based near-field measurement, the aforementioned miniaturized antenna operating near 40 MHz (see Chapter III) is used as AUT. In addition, as mentioned earlier, the surface of rectangular cuboid enclosing the AUT is considered

Table 5.1
Very-near-field measurement parameters

Freq. (MHz)	d_p (mm)	Δs (mm)	N_i (i=x,y,z)	Probed area (cm × cm)
40	15 30 (Back)	5	N_x: 30 N_y: 27 N_z: 37	Top & Bottom: 13×14.5 Front & Back: 13×18 Left & Right: 14.5×18

as the probed surface. This allows for utilization of planar near-field scanning that requires a simple X-Y translation unit. The planar near-field scanning is performed over six surfaces of the rectangular cuboid as shown in Fig. 5.2. Spatial resolution of the scanned grid and probe distance from the aperture of the AUT are also important parameters of the measurement setup. According to the sampling theorem [79], the spacing between sampled points must be at least $\lambda_o/2$ so as not to introduce reconstruction errors known as aliasing. Moreover, the spatial resolution is related to probe distance in the sense that choosing one would determine the other. For large aperture antennas, the higher is the sampling interval, the faster and more efficient is the measurement. The common relationship used between the sampling interval and probe distance is given by [73]

$$\Delta s = \frac{\lambda_0}{2\sqrt{1+(\frac{\lambda_0}{d_p})^2}} \tag{5.13}$$

where Δs is the sampling interval and d_p is the probe distance. For small antennas that are proportional or smaller than a wavelength the sampling interval should be even smaller than what

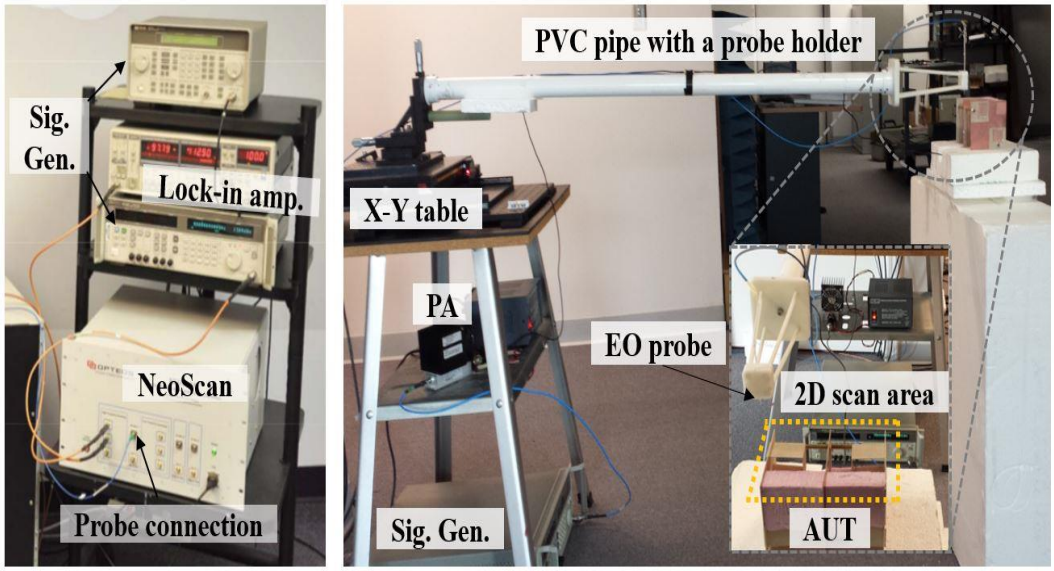

Figure 5.7: Actual measurement setup for very-near-field measurements of the AUT. The measurements were performed in a small indoor space.

is given by (5.13). As mentioned before, for small antennas at low frequencies, measurements should be performed very near to the smallest antenna-enclosing surface. This ensures the dominant component of the measured field is the direct antenna field and not the multipath. In addition, since the fields are strongest there the highest signal-to-noise ratio is achieved for a given input power. The rectangular cuboid probed area S is chosen to be as small as possible so as not to increase the number of sampled points N_i(i=x, y, and z), and consequently measurement time. The measurement parameters used are shown in Table 5.1.

The very-near-field measurements of the miniaturized low-VHF antenna were conducted in a small indoor space as depicted in Fig. 5.7. To avoid unwanted electromagnetic coupling effects between the radiating element and the surrounding objects, the antenna is placed away from nearby objects so that the scatterers are not within the antenna near-field reactive region. The RF field probe system consists of a fiber-coupled EO probe, power amplifier, signal generators, lock-in amplifier, and NeoScan including EO modulators and demodulators and sensitive RF components.

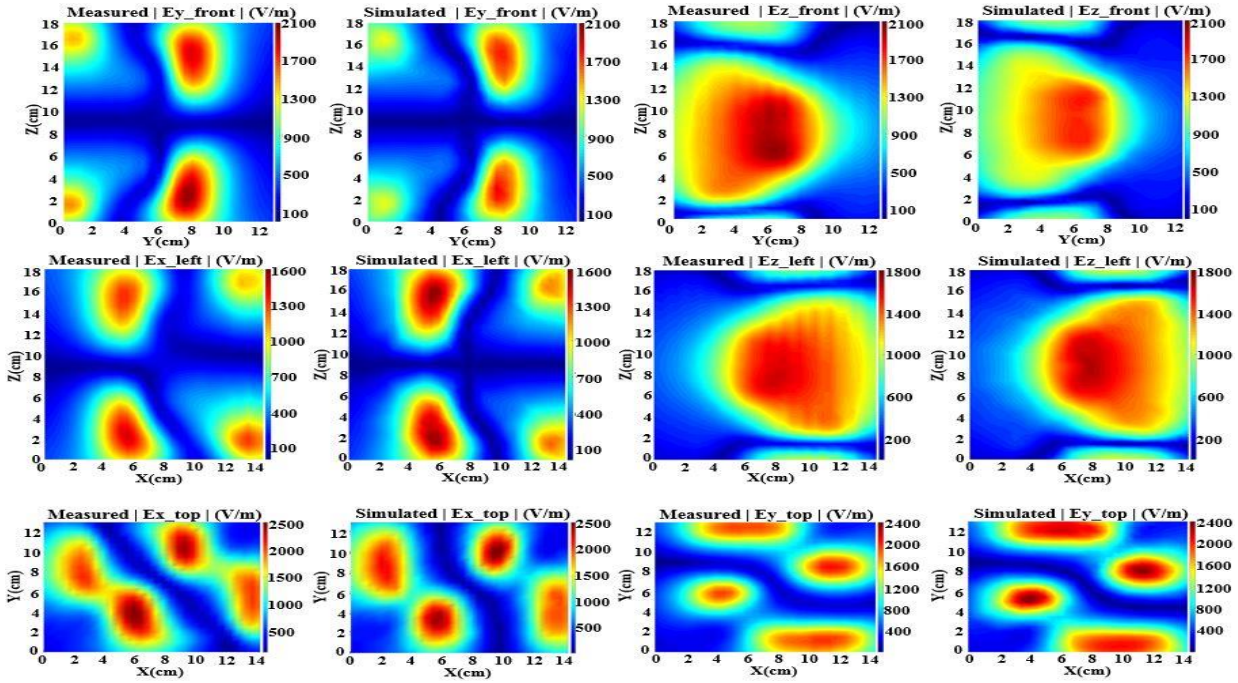

Figure 5.8: Simulated (40. 01 MHz) and measured (40.06 MHz) very-near-field maps showing the tangential components (magnitudes) of the electric fields on the front, left, and top surface of the imaginary box illustrated in Fig. 5.2.

The system is also equipped with a high precision two axes motor controlled X-Y table, which can move across an area of up to 25.4 cm × 25.4 cm, to position and move the probe. In this experiment, the EO probe is mounted via a lightweight PVC pipe connected to the X-Y table. The pipe provides a separation between all the supporting instruments and the AUT as shown in Fig. 5.7. The surfaces of the rectangular box enclosing the AUT are scanned separately and the measured data are utilized for far-field prediction from post processing.

The raw data from the scan are multiplied by the calculated calibration coefficient α to obtain the absolute value of the tangential electric fields. Fig. 5.8 and 5.9 show the simulated and measured two-dimensional magnitude and phase distributions of the tangential electric field on the front, left, and top faces of the rectangular box (results on the other faces of the box are shown in Appendix D). To compare the absolute value of the measured field with simulations, the available

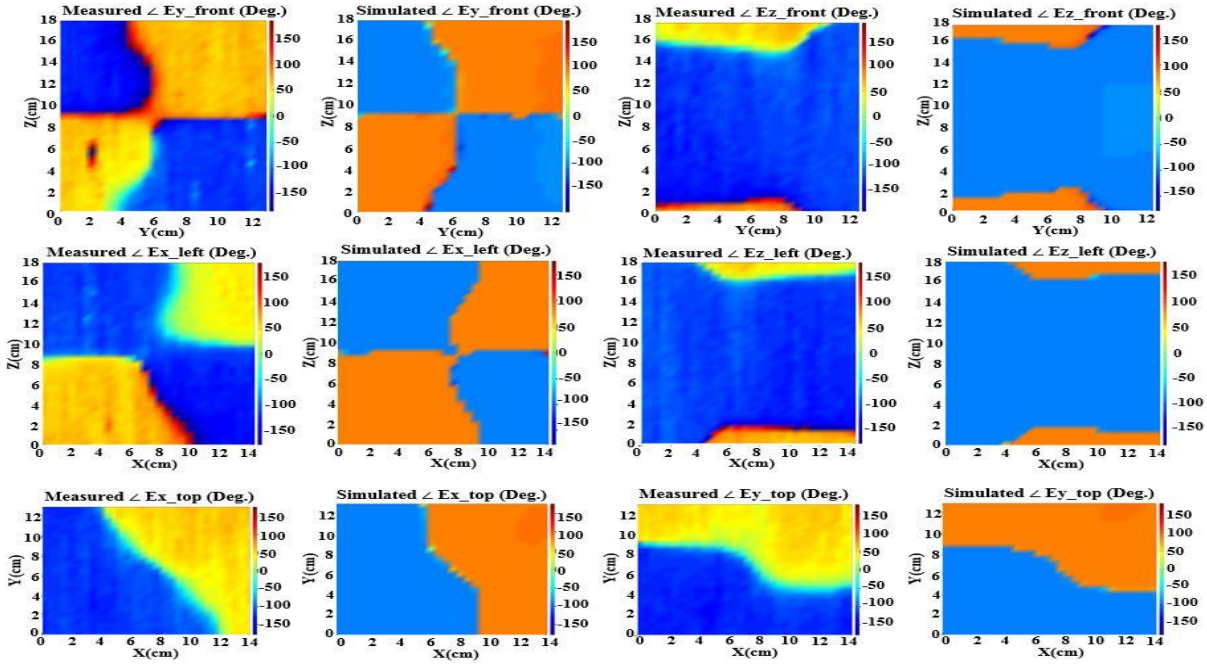

Figure 5.9: Simulated (40.01 MHz) and measured (40.06 MHz) very-near-field maps showing the tangential components (phases) of the electric fields on the front, left, and top surface of the imaginary box illustrated in Fig. 5.2.

input power to the AUT delivered by the RF source employed for measurements is used to calculate the voltage at the antenna input terminals. The comparison between the measurement and simulation of near fields shows an excellent agreement between the magnitude of the measured and simulated results. Note that here the data comparison is absolute and not relative. There is a constant 30 degrees phase difference between the measured and simulated results. The reason for this is that NeoScan system cannot measure the absolute phase, as the phase of the local oscillator in the system cannot be determined. Such a difference, however, does not affect the accuracy in the far-field characterization of the AUT, since the relative phase distribution is important. It should also be noted that the absolute phase for each surface is adjusted to that of an adjacent surface by making sure the measured values at one common edge agree.

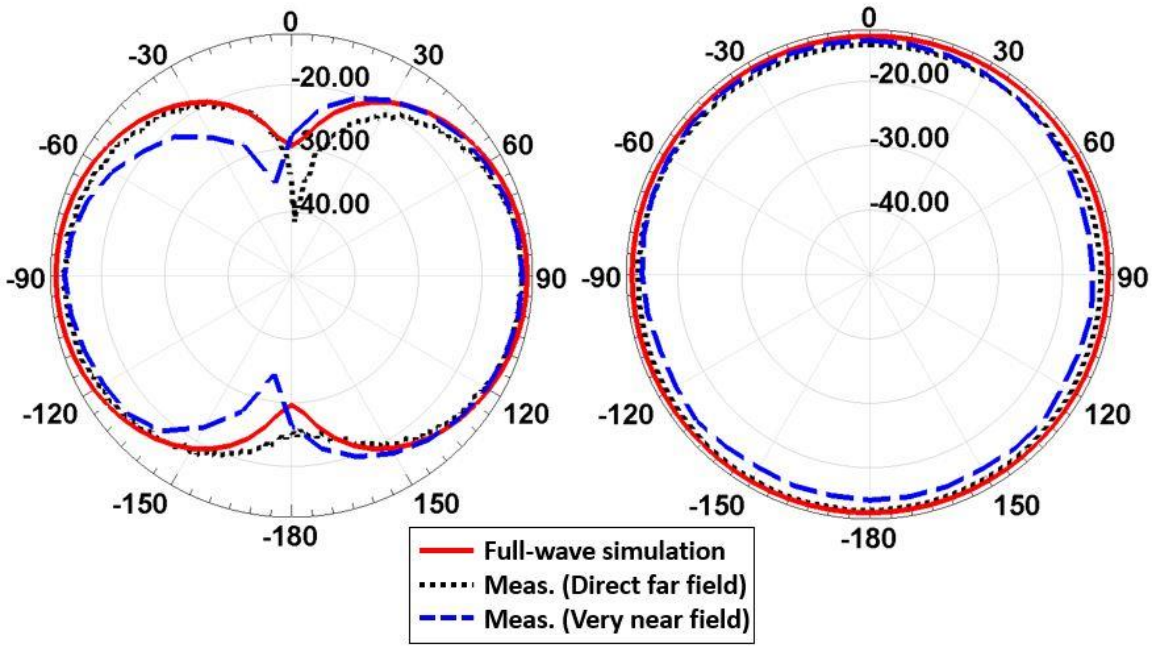

(a) (b)

Figure 5.10: Antenna radiation patterns (vertical polarization) in (a) E-plane (xz plane) and (b) H-plane (xy plane), computed by different approaches (The scale in the plot is ranging from -50 dBi to -10 dBi).

With this data, the far-field pattern and gain are evaluated using the procedure outlined in Section 5.3. Fig. 5.10 shows the far-field radiation patterns in two orthogonal principal planes (E-plane and H-plane), together with simulated and measured results taken from the far-field measurements in the elevated range (using a small source module for feeding the AUT) discussed earlier. The patterns also closely resemble that of a short electric dipole with the maximum gain occurring at $\theta = 90^{\circ}$. It should be mentioned that the difference of the radiation pattern is mainly due to a small difference in the antenna feed configurations in the simulation and the actual setup. In the actual setup for the very-near-field measurement, a coaxial cable was connected for feeding the AUT. The antenna excites a current over the surface of the outer layer of the coaxial feed line, which in turn changes the near field on the surface of the scanned area adjacent to the coaxial feed. This undesired effect can be eliminated by using a small source module as reported in [20]. Table

Table 5.2
Antenna gain comparison obtained from different approaches

Process	Simulation	Direct-far-field	Very-near-field
Center freq.	40.01 MHz	40.00 MHz	40.06 MHz
Peak gain	-12.8 dBi	-13.3 dBi	-13.6 dBi

5.2 presents a comparison of the antenna gain at resonance obtained from the proposed very-near-field method, simulation, and the elevated range far-field method.

5.5 Summary

A novel near-field measurement method for characterization of 3D radiation pattern and gain of antennas is presented. The approach is based on measuring the tangential components of electric field over arbitrary closed surfaces that enclose the AUT very close to the antenna boundary using a very small non-intrusive, all-dielectric, and broadband electro-optical probe. This approach is shown to be a very effective and time-efficient method for accurate characterization of HF/VHF antennas for which anechoic chambers cannot be built and the far-field methods cannot provide accurate results due to different factors such as the presence of the ground plane and proximity of feeding cables and measurement instruments. A new formulation based on the field equivalence principle and reaction theorem is developed to perform the near-field to far-field transformation without any approximations. To examine the validity of the

proposed approach, an electrically small VHF (40 MHz) antenna is used. The measurements are performed indoor in a laboratory setting with objects removed from the near-field region of the antenna. The gain and radiation pattern are compared with simulation results and an elevated far-field measured results, and excellent agreement is demonstrated.

CHAPTER VI

Compact, Low-Power, Low-VHF Mobile Radio Networking

6.1 Introduction

Establishing reliable wireless communications in complex scenarios such as tunnels, indoor and urban environments at conventional microwave frequency bands is very challenging [1]-[3]. This is principally due to interference generated by other neighboring devices and signal attenuation and fading caused by a multitude of scatterers in such environments. To alleviate these difficulties, various networking technologies have been developed such as cooperative multi-hop routing, multi-input and multi-output (MIMO) techniques, and other diversity schemes [5]-[7]. Besides complexity and cost, such systems often require high power that is undesirable for most wireless ad hoc networks. Low frequency wireless communications can be exploited to tackle the aforementioned challenges by significantly reducing the effect of multipath and attenuation.

Recently, we investigated wave propagation properties at lower frequency bands through physics-based simulation and extensive measurements in various scenarios [10]-[11] (see Chapter II). These studies show that the reliability of wireless links in complex indoor and outdoor scenarios is significantly better at HF and low-VHF bands compared to higher frequencies, owing to much less multipath fading, attenuation, phase distortion, and delay spread. Despite these advantages, large antenna sizes or high power operation due to the poor efficiency of existing small antennas poses a challenge to the realization of a compact, low-power communication system. In

Chapter III, we introduced an efficient, miniature low-VHF antenna whose overall dimensions are 10 cm × 10 cm × 15 cm ($0.013\lambda_0 \times 0.013\lambda_0 \times 0.02\lambda_0$) with weight of about 98 grams. For the system and experiments presented in this chapter, the antenna is further modified to broaden its bandwidth in consideration of proximity effects due to a large number of surrounding objects in complex environments, and its performance is analyzed and demonstrated.

To demonstrate low power communications using the modified antenna ($0.04\lambda_0$ in height), we consider the ZigBee standard that defines a suite of communication protocols intended for low-data-rate, short-range wireless networking [80]. Integrating the ZigBee radio with an optimally designed bi-directional frequency converter and miniature antenna, a compact, low-power, low-cost, low-VHF radio system that enables longer-range wireless ad hoc networks can be realized. The frequency converter, which is used to translate signals occupying the ZigBee frequency band to low-VHF band and vice versa, is carefully designed to have optimal performance parameters including conversion gain, sensitivity, and power consumption. In Section 6.2, the design and analysis of the frequency conversion system is described. Section 6.3 includes a brief description of the miniaturized low-VHF antenna and the radio system integration with a small mobile platform for various communications and geolocation applications [81]. Performance characterization of the proposed radio system based on measurements carried out in complex environments are discussed in Section 6.4.

6.2 Frequency Conversion Circuit Design and Analysis

An important component is the bi-directional frequency conversion circuit that enables simultaneous transmission and reception of signals produced by a ZigBee module without loss of

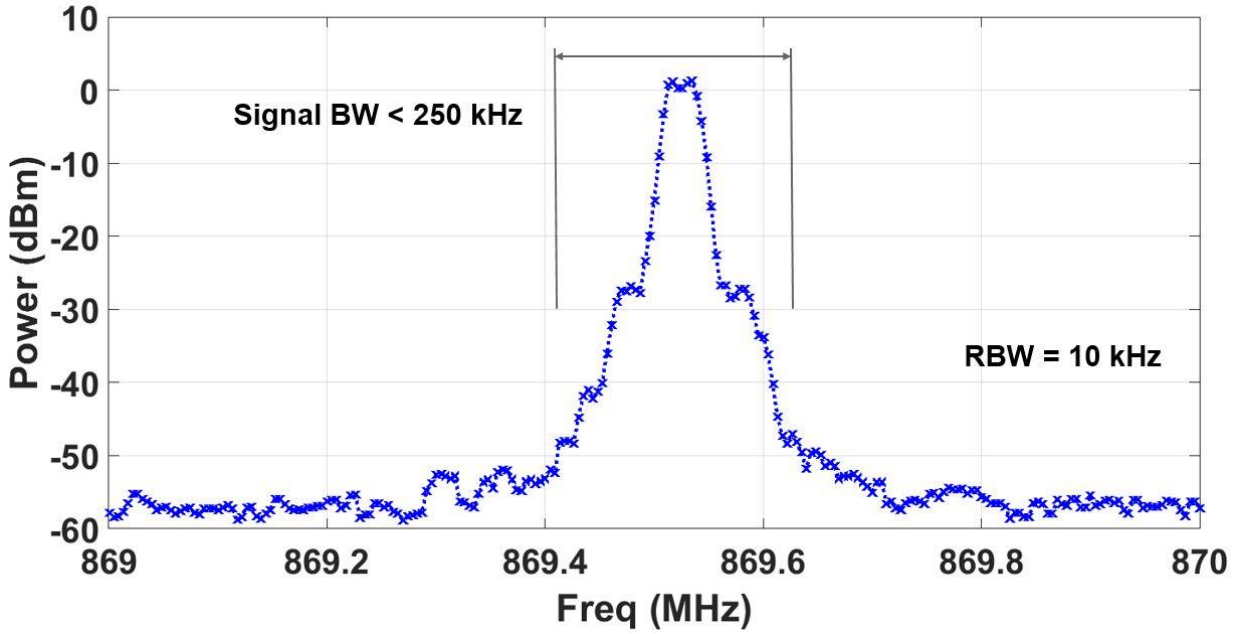

Figure 6.1: Measured output power spectrum of an off-the-shelf 868 MHz ZigBee module.

fidelity. The appropriate ZigBee module must be selected taking into account the low-VHF antenna specifications. We utilize the XBee-PRO 868 operating at 869.5 MHz, whose bandwidth is within that of our miniature low-VHF antenna. As described in the datasheet, this module has a receiver sensitivity of -112 dBm, data rate of 24 Kbps, and a transmit power ranging from 1 mW to 315 mW depending on the power setting [82]. In Fig. 6.1, the measured signal source power spectrum is plotted and is utilized for analysis of the frequency conversion system.

When designing the frequency converter architecture, we primarily consider power dissipation, complexity, and cost. Fig. 6.2 shows a simplified schematic of our design. It is composed of a power splitter/combiner, voltage-controlled crystal oscillator (VCXO), low-power low-noise amplifier, a double-balanced passive mixer with high port-to-port isolation ($>$ 50 dB), and customized band-pass filter. As a duplexer, the power splitter/combiner must be chosen to offer a very high isolation because this limits the gain that can be introduced by the amplifiers. For

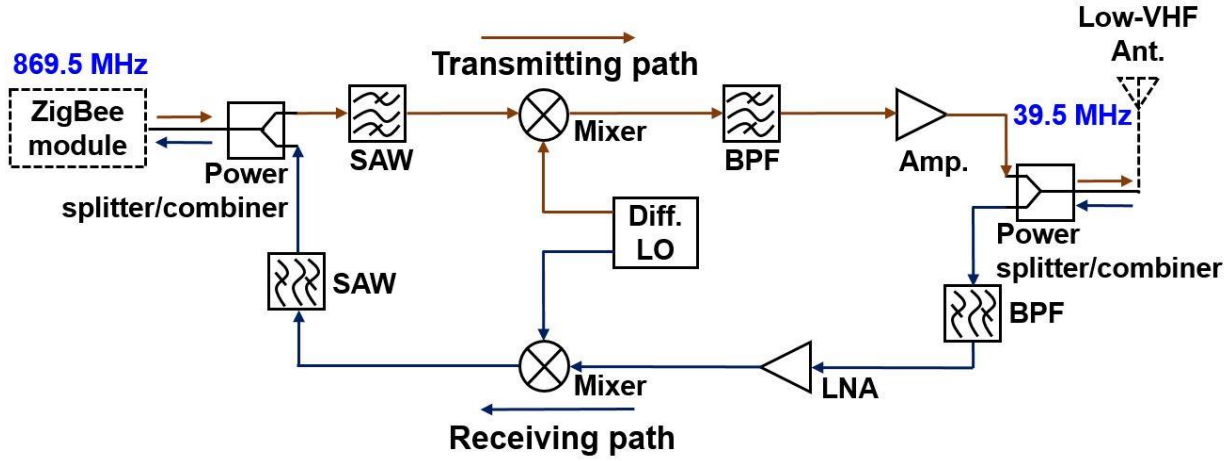

Figure 6.2: Simplified schematic diagram of the bi-directional frequency converter.

this reason, a power splitter/combiner with isolation of better than 40 dB is selected to reduce the transmission leakage through the duplexer which degrades signal to noise ratio (SNR). In addition, an ultra-low phase noise VCXO with a center frequency of 830 MHz is chosen to produce two symmetrical output signals that are 180-degree out of phase with each other [83]. This allows the use of a common local oscillator (LO) and eliminates the need for a power splitter for a single LO driving both the up and down conversion mixers.

Next, we report on a circuit analysis of the frequency converter. System sensitivity, defined as the minimum detectable signal (MDS) level to achieve a certain bit error rate, is a critical parameter of a radio receiver because a higher sensitivity correlates with longer transmission range. As described in [84], the MDS level at the input of the receiving system can be calculated for a given minimum SNR at the output and the system noise characteristics, using:

$$MDS = kB[T_A + (NF - 1)T_0]SNR_{min}, \tag{6.1}$$

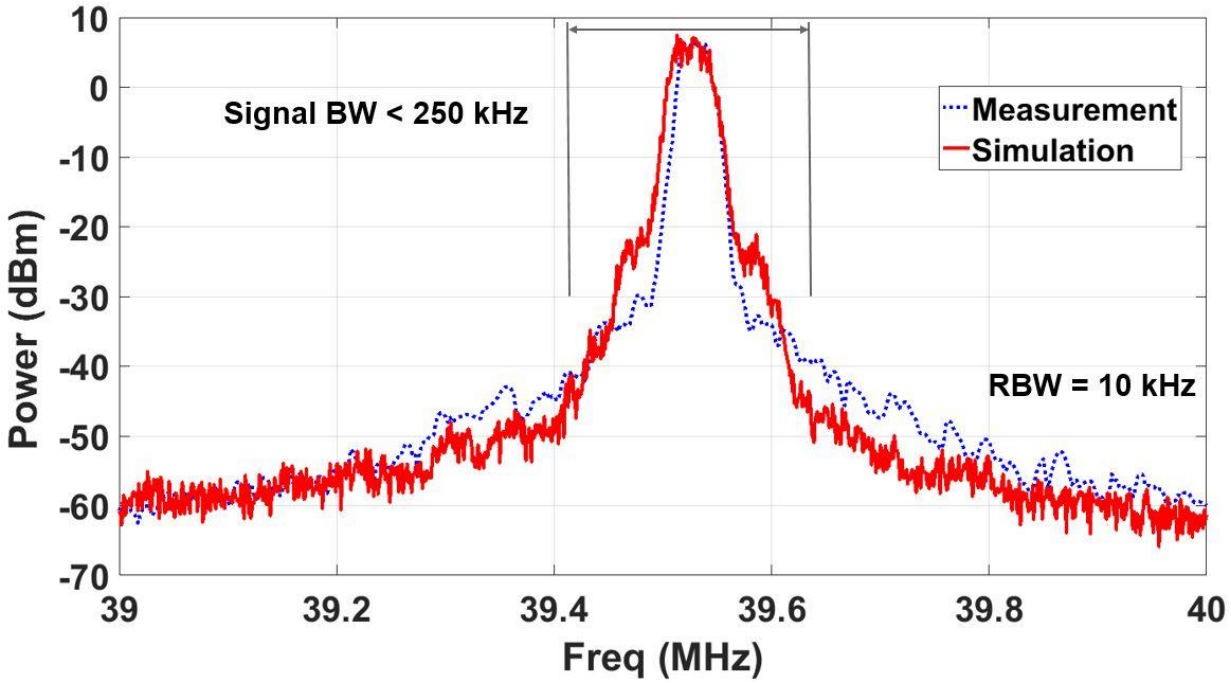

Figure 6.3: Signal power spectrum of the 868 MHz ZigBee source after down-converted to low VHF.

where k is Boltzmann's constant, B is the bandwidth of the receiving system, NF is the receiver noise figure, T_A is the antenna noise temperature, and T_0 is 290 Kelvin.

It is also important to track power levels through the RF stages of the receiving system to avoid harmonic and intermodulation distortion. The linear dynamic range, which is the difference between the maximum allowable and minimum detectable signal power that can be processed, is quantified based on a single-tone analysis. The overall performance of the frequency converter was characterized via circuit simulation (Agilent SystemVue 2015). The system sensitivity (-98 dBm) is obtained by assuming T_A is equal to T_0 and that the antenna is matched to the system. Furthermore, with fixed 1 mW transmit output power, the system meets the isolation requirement for full-duplex operation [85]. This is essential to prevent intermodulation distortion in the receiver, generated by transmit leakage and the leaked noise from the transmitting system, from hampering

detection of weak received signals. Insertion gain of the system for both transmission and reception is maintained at 7 dB within the linear dynamic range (75 dB). The signal power spectrum of the frequency conversion system, when the modulated signal from the ZigBee source is input, is illustrated in Fig. 6.3. Based on the simulation modeling and analysis, the frequency converter was fabricated and integrated with the ZigBee module and antenna. Details of the complete radio system are discussed in the following section.

6.3 Antenna Miniaturization and Compact Mobile Radio System

6.3.1 Miniaturized Low-VHF Antennas

As alluded to earlier, the large size of conventional antennas at the lower VHF band imposes a practical limitation on the development of compact systems for wireless communications. Electrically small low-VHF antennas have been designed to overcome this [40], [86]. However, these designs still have relatively large dimensions and mass such that they are not appropriate for integration onto small mobile platforms. In Chapter III, we proposed a very small-form-factor, lightweight antenna operating at this band to enable very compact communication systems. The antenna miniaturization is realized by applying a 180-degree phase shifter that is composed of series inductors and an open stub [19], [20]. By connecting two main radiating elements to each end of the phase shifter, in-phase vertically polarized fields is produced from the elements at resonant frequency. This results in an increase in the effective height of the antenna, and consequently, enhances the gain without physically increasing the height. In an effort to further increase antenna efficiency and reduce mass, optimized rectangular air-core coils with high quality

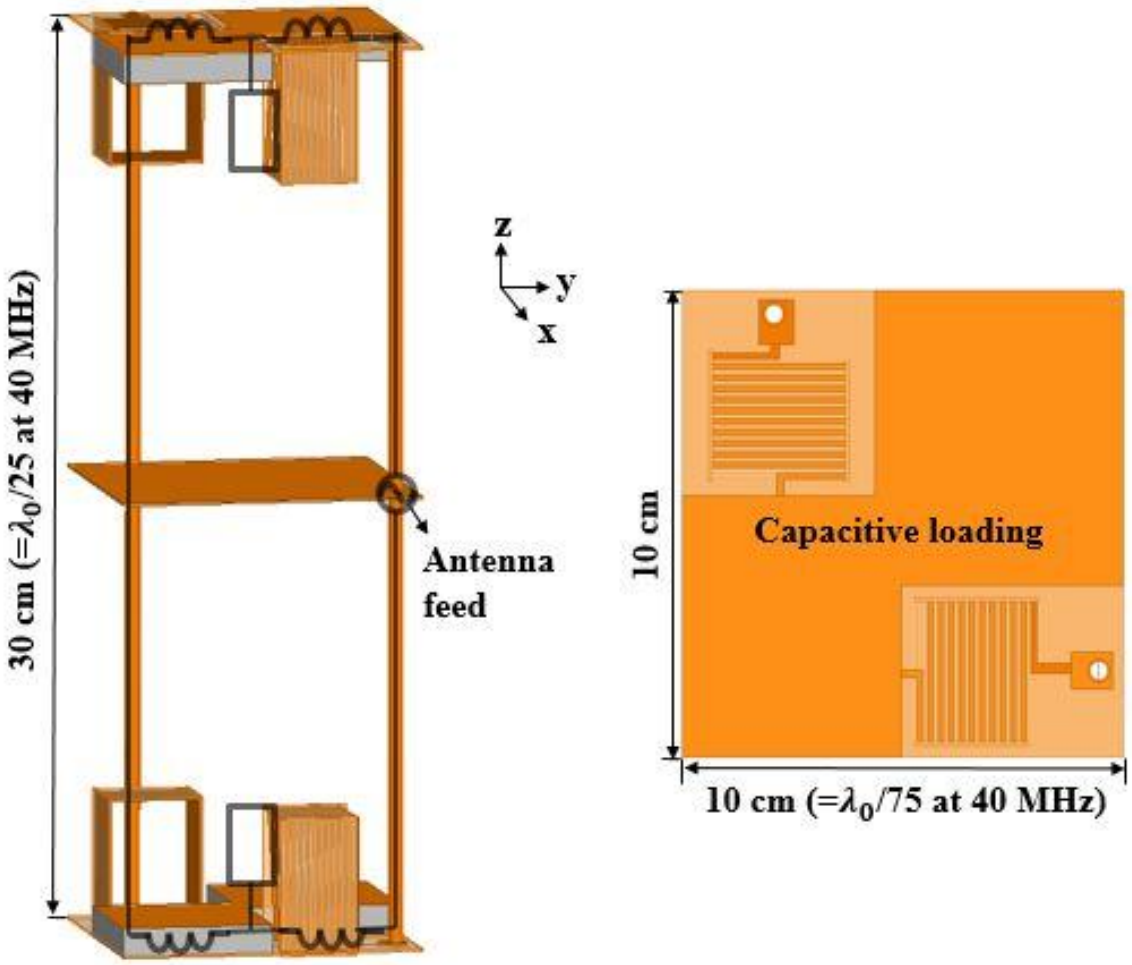

(a) (b)

Figure 6.4: Geometry of the miniature low-VHF antenna: (a) Side view with the 180-degree phase shifters circuit model superimposed and (b) top view.

factors, and capacitive loadings without dielectric materials to form the open stub, are used in the antenna design.

To facilitate experiments in highly cluttered environments, we further modify the antenna to enhance its bandwidth. The improved bandwidth enables the system to work even if there is slight resonant frequency shift due to coupling with nearby scatterers, which is an important practical consideration. Fig. 6.4 depicts the side and top views of the modified antenna with its equivalent circuit model superimposed over the side view. The lateral dimension and height are

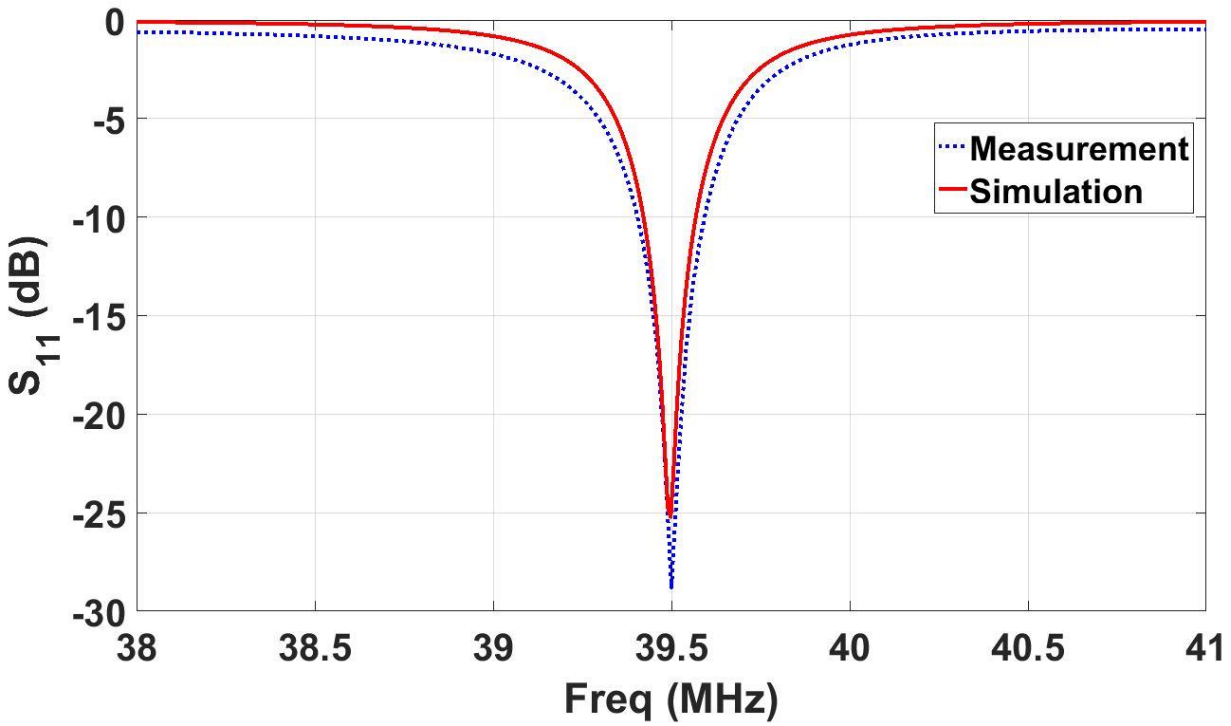

Figure 6.5: Simulated and measured input impedance of the miniature low-VHF antenna.

10 cm ($0.013\lambda_0$) and 30 cm ($0.04\lambda_0$), respectively. Additional metallic plates consisting of polyethylene sheets with a dielectric constant $\varepsilon_r = 2.5$ are inserted between the top and bottom plates to support capacitive plates in the antenna enabling in-phase radiation from the poles at resonance. Despite its small size, impedance matching of the antenna can easily be achieved without using an additional matching network simply by controlling the distance between the vertical posts of the dipole.

Fig. 6.5 shows the measured input reflection coefficient of the antenna using a calibrated vector network analyzer, together with the simulated one. The antenna has a fractional bandwidth of 0.56 % for a voltage standing wave ratio of 2:1. The antenna produces an omni-directional radiation pattern with a peak gain of -10 dBi, as shown in Fig. 6.6. In the fabrication of the antenna,

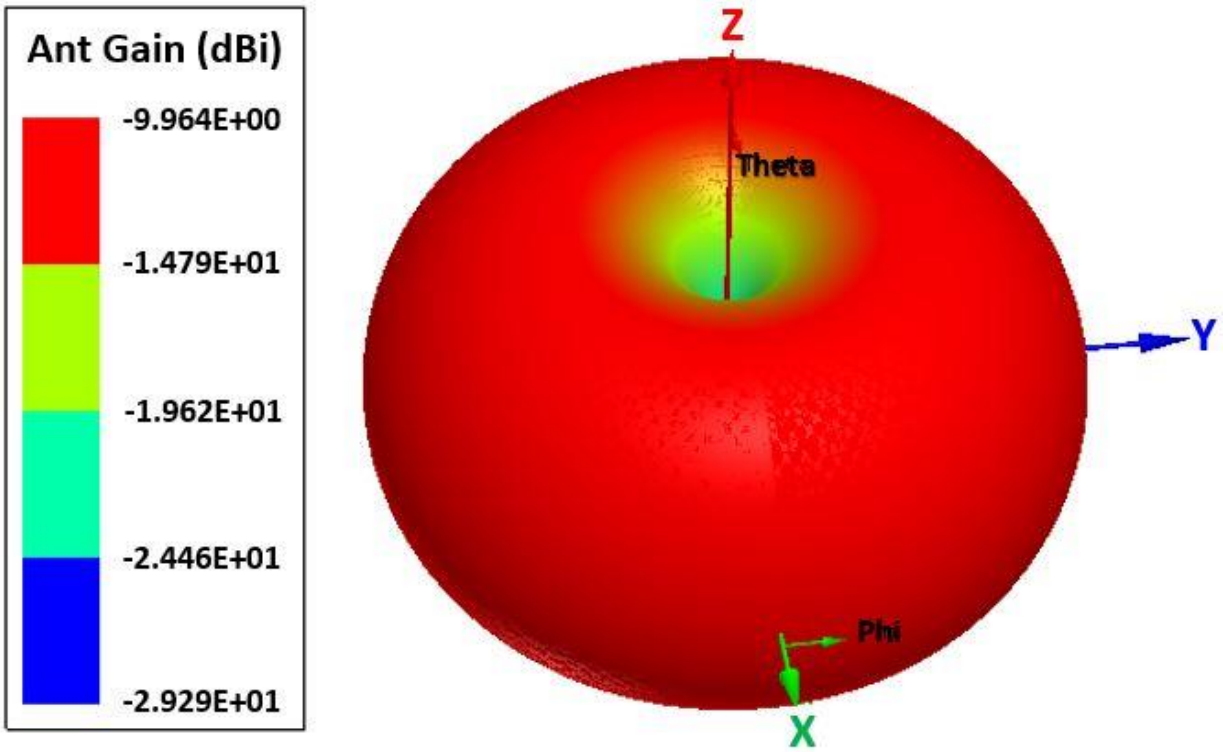

Figure 6.6: Simulated 3D antenna radiation pattern showing omni-directional response.

adjustable telescoping metal poles (the main radiating elements) are utilized to fine-tune the resonance frequency.

6.3.2 Radio System Fabrication and Integration

The antenna and frequency translation circuit were used to seamlessly operate a ZigBee radio in the lower VHF. In order to achieve compact size, a circuit layout of the RF converter is optimally designed and fabricated on a Rogers RO4003C substrate, with 0.812 mm thickness and size of 45 mm × 35 mm. The XBee-PRO 868 module is integrated with the circuit via a tailored semi-rigid coaxial cable and is positioned underneath the circuit. In order to minimize the effect of RF interference caused by signal leakage from the ZigBee module itself, as well as other

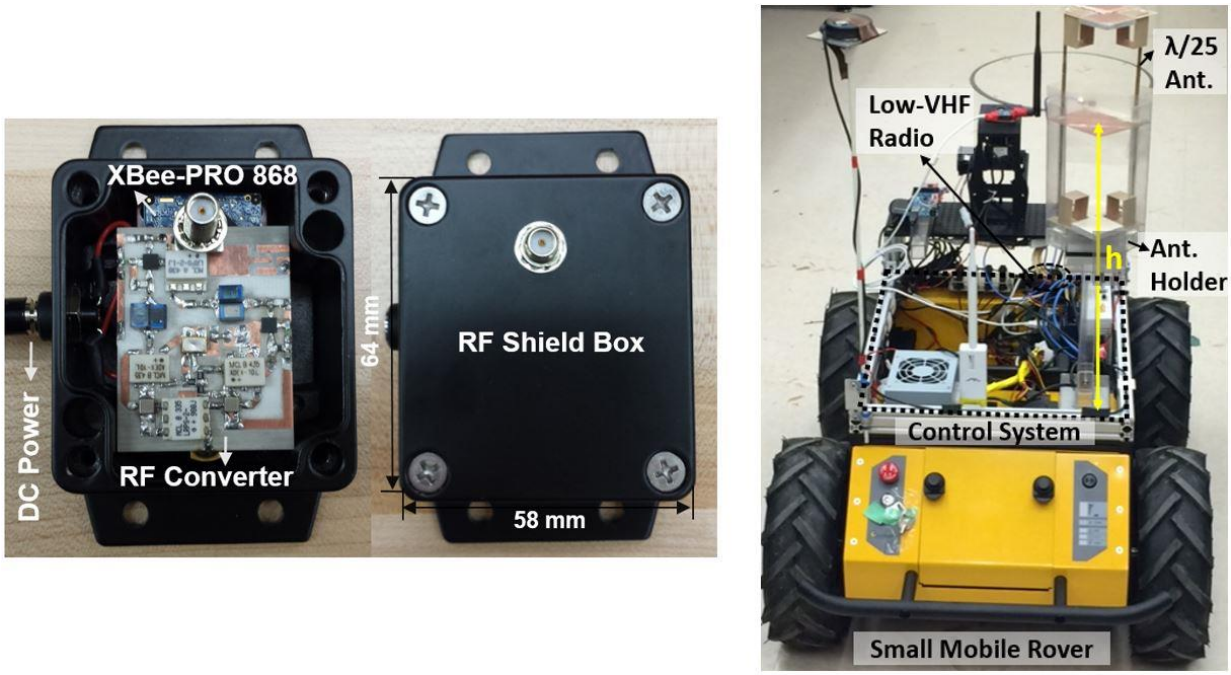

(a) (b)

Figure 6.7: (a) The frequency-shifted ZigBee radio package and (b) the autonomous robotic platform with the radio and antenna integrated for mobile experiments.

external noise sources, the assembled radio is enclosed in an RF shield box. Fig. 6.7(a) illustrates the fabricated low-VHF radios having overall dimensions of 64 mm × 58 mm × 35 mm and weight of about 270 grams. DC power for the radio operation is supplied by a high capacity battery via panel mount connectors.

Since the experimental radio with the miniaturized antenna is to be integrated onto a small mobile platform (see Fig. 6.7(b)), the subsequent electromagnetic coupling effect on the antenna performance must be examined. It should also be noted that ground losses increase as the height of the antenna decreases. To minimize the overall profile of the mobile system as well as the coupling effect, the optimal antenna height should be determined. This is done by measuring the reflection coefficient of the antenna as a function of height h above the platform (see Appendix E). The smallest height (measured from the top of the platform to the phase center of the antenna)

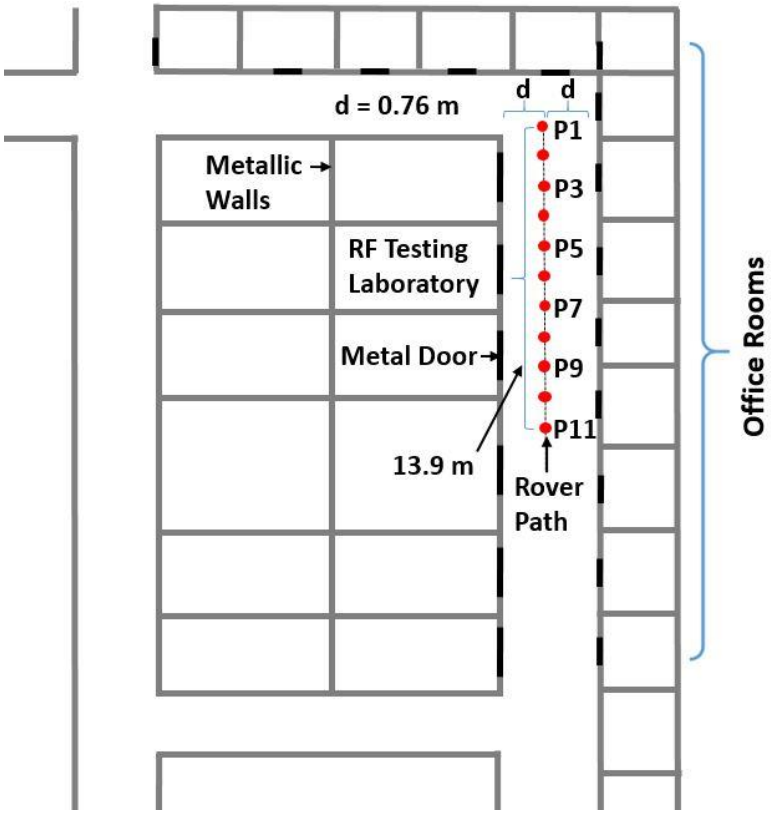

Figure 6.8: Office-building test scenario where the effect of nearby scatterers is investigated. The robotic rover platform shown in Fig. 6.7(b) is moved along the indicated path.

where the performance of the antenna is not affected by the mobile platform is found to be 46 cm ($0.06\lambda_0$).

As stated earlier, the proximity effect of nearby materials and structures in the environments may bring about a shift in resonant frequency, which in turn results in significant degradation of the wireless communication quality due to the frequency misalignment of the signal spectrum and antenna response. To examine this effect, the input impedance of the antenna as a function of frequency was measured on the mobile robotic system in a complex indoor environment consisting of metallic partitions, walls, and doors. The mobile system was positioned close to large metallic walls and moved along the marked points in a narrow corridor (see Fig. 6.8). As shown in Fig. 6.9, we observed at most 0.25 % shift in the center frequency in this environment.

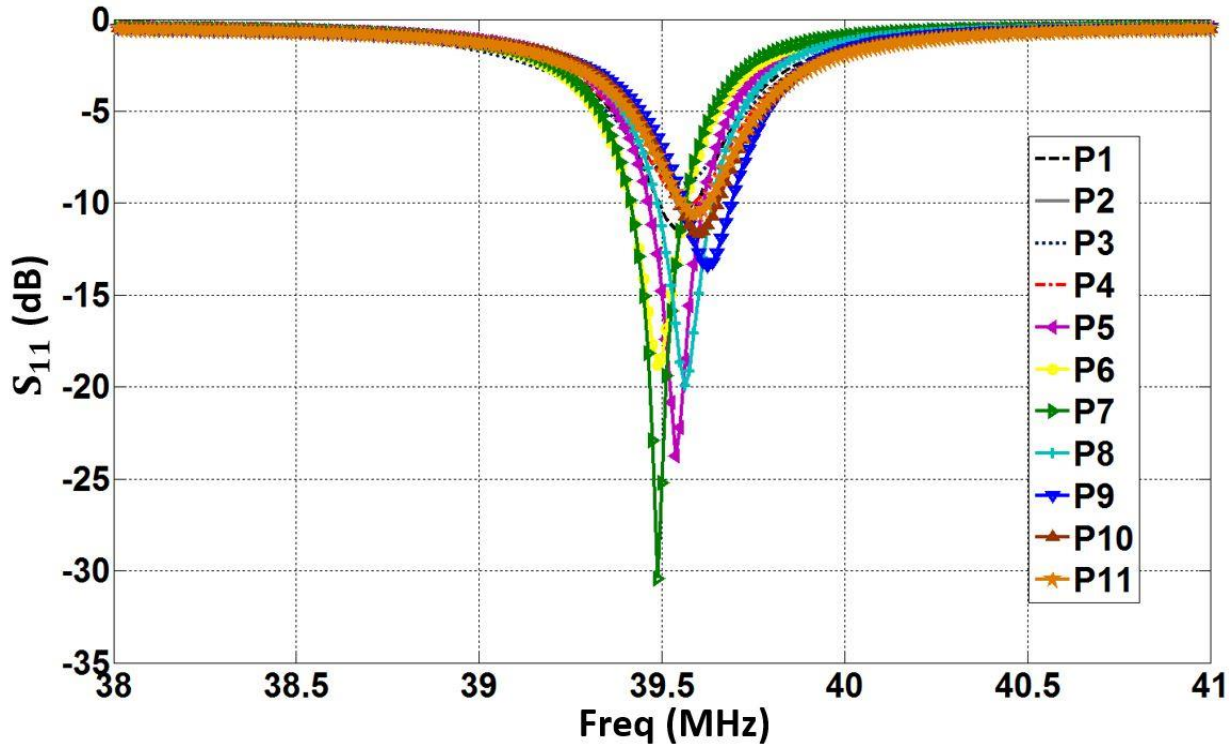

Figure 6.9: Measured resonant frequency of the miniature low-VHF antenna on the robotic platform at points indicated in Fig. 6.8.

This is representative of other indoor and outdoor environments tested, indicating that only small shifts are likely in cases of interest.

6.4 Performance Characterization

6.4.1 Measurement Setup and Scenarios

Performance for point-to-point low-VHF near-ground communication is fully characterized in two different scenarios: 1) complex outdoor channel and 2) multi-floor indoor-to-outdoor channel. In Scenario 1 (see Fig. 6.10), the measurement site is surrounded by large and tall university buildings that are composed of bricks, a steel frame structure with metallic

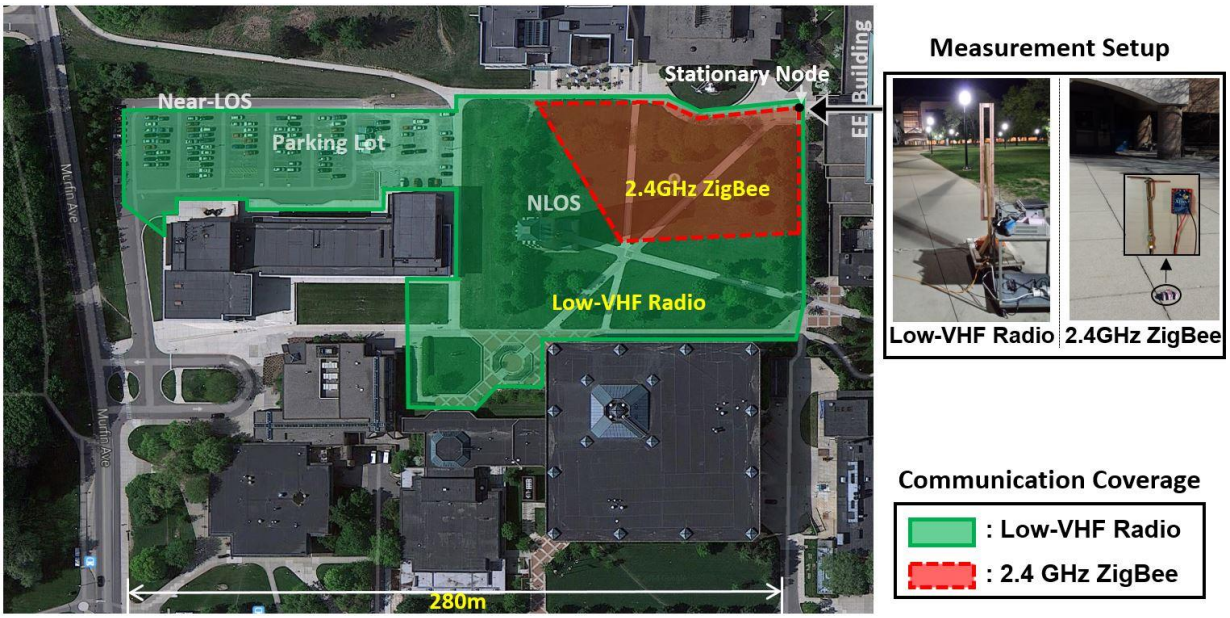

Figure 6.10: Coverage maps of point-to-point wireless communications (proposed low-VHF radio vs. 2.4 GHz ZigBee radio) in the near-LOS and NLOS outdoor case (Scenario 1).

reinforcement, and the propagation channel is blocked by multiple trees and obstructions (tall clock tower, metallic sculptures, lampposts, and a large number of vehicles in the university parking lot). A stationary node is located near the entrance of the electrical engineering building at the University of Michigan and a mobile node is moved away from the stationary node to map communication coverage in the area. This scenario also includes near-line of sight (LOS) as well as non-line of sight (NLOS) to investigate the performance in the presence of different near-ground wave propagation effects.

In Scenario 2 (see Fig. 6.11), a stationary node is located on the second floor of a three-story building composed of various research equipment (radar measurement system, large overhead crane, beacon positioning system on the large metal frame structure, etc.). This building is surrounded by dense vegetation and wire mesh fence as well as a few other nearby buildings. A mobile node is maneuvered from the inside toward the outside of the building. With this scenario,

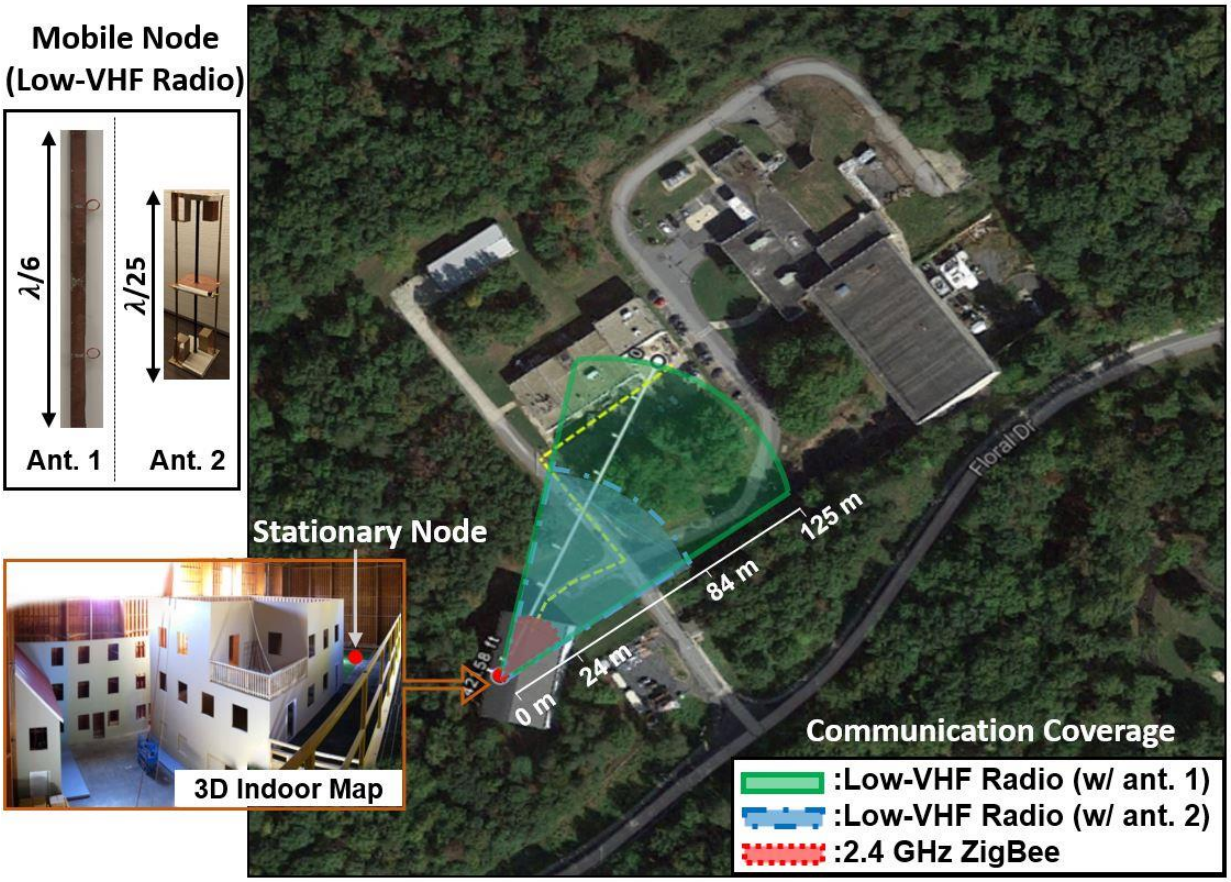

Figure 6.11: Coverage maps of point-to-point wireless communications (proposed low-VHF radio with two different antennas at the mobile node vs. 2.4 GHz ZigBee radio) in the NLOS multi-floor indoor to outdoor case (Scenario 2).

the impact of different antenna positions can be observed. Also, additional tests utilizing ZigBee module (XBP24) operating at 2.4 GHz under the same measurement conditions were conducted for performance comparison.

The radio at the stationary node is connected to a laptop through a USB port for control. The radio at the mobile node is powered by a portable battery with a DC-DC converter (12 V to 3.3 V) and integrated onto the mobile platform as shown in Fig. 6.7(b). Measurement parameters of the frequency translated low-VHF ZigBee and the ZigBee operating at 2.4 GHz were carefully determined for a fair comparison of communication coverage, and are listed in Table 6.1.

Table 6.1
Radio specifications and measurement settings

Radio Type	Low-VHF		ZigBee		
Carrier Frequency	39.5 MHz		2.4 GHz		
Supply Voltage	3.3 V		3.3 V		
Current Drain	235 mA (Tx), 215 mA (Rx)		155 mA (Tx), 153 mA (Rx)		
RF Data Rate	24 Kbps		250 Kbps		
Receiver Sensitivity	-98 dBm		-100 dBm		
Number of Channels	1		12		
Modulation Type	FSK		QPSK		
Dimension	64 mm × 58 mm × 35 mm		27 mm × 33 mm × 10 mm		
Approx. Weight	270 g		15 g		
Transmit Power	7 dBm		0 dBm	12 dBm	10 dBm
Attenuator Loss	·		·	20 dB	·
Antenna	Scenario 1	Scenario 2	Scenario 1	Scenario 2	
$G_{stationary}$	0 dBi (λ_0/5 ant)	0 dBi (λ_0/5 ant)	2.15 dBi (λ_0/2 ant)	3.0 dBi (HG2403RD)	
G_{mobile}	-1 dBi (λ_0/6 ant)		2.15 dBi (λ_0/2 ant)	3.0 dBi (HG2403RD)	
	·	-10 dBi (λ_0/25 ant)			
Height	1.65 m ($0.22\lambda_0$)	1.73 m ($0.23\lambda_0$)	0.035 m ($0.28\lambda_0$)	1.73 m ($13.84\lambda_0$)	

Considering the relevant parameters of the antennas utilized for measurements, the transmit power (which is internally fixed in the off-the-shelf modules) and system gain were carefully adjusted using an external attenuator so that path loss due to propagation is carefully measured via the RSSI, ensuring a fair comparison between bands. In Scenario 1, the antenna heights in terms of wavelength were kept the same. This ensures that the near-ground propagation effects including Norton surface waves are similar at the two frequency bands [32], [35]. In Scenario 2, the same physical antenna heights were considered. This is more relevant if one is interested in choosing the better system at a given antenna height of interest.

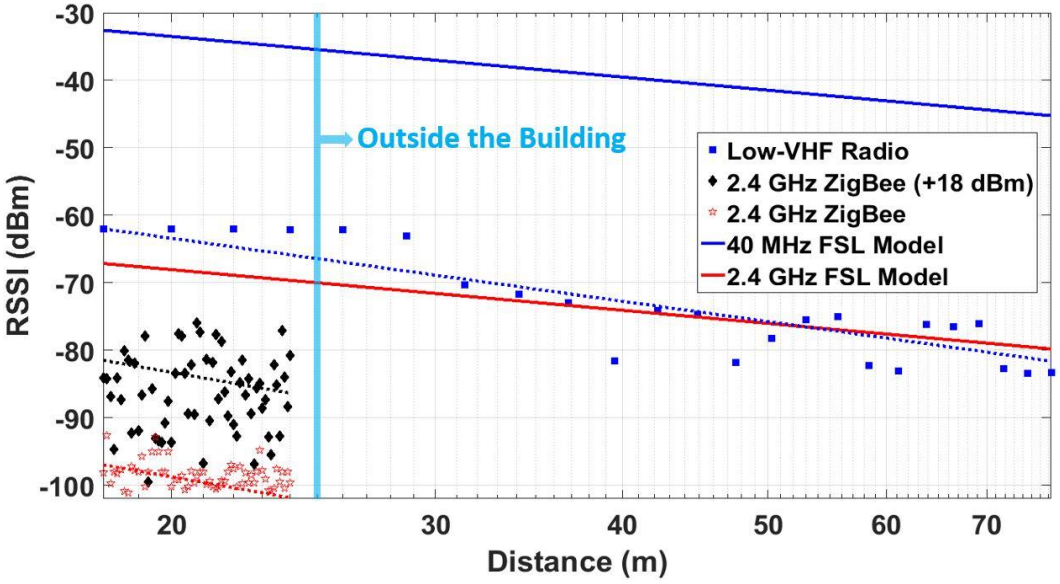

(a)

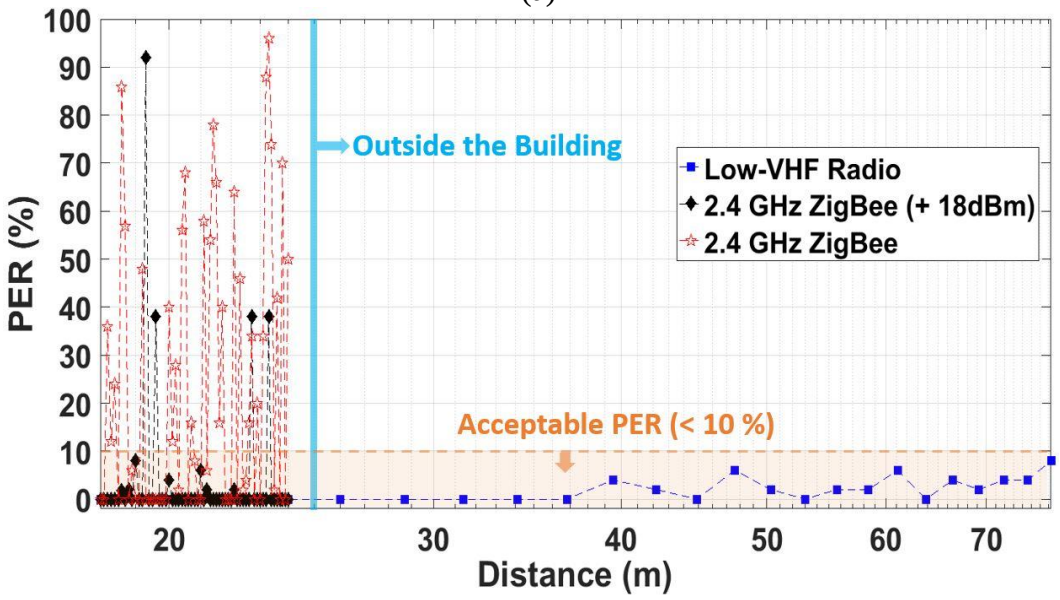

(b)

Figure 6.12: (a) Average RSSI and (b) PER vs. distance with antenna 2 in Scenario 2, compared with FSL models at 40 MHz and 2.4 GHz. To better observe small-scale fading, an additional measurement for the 2.4 GHz ZigBee with higher transmit power is also shown.

6.4.2 Measurement Results and Discussion

Point-to-point wireless communication coverages are mapped by monitoring successful data packet transmissions and received signal strength indicator (RSSI) values using X-CTU radio

testing software [87]. This captures both the RSSI per packet and the packet success rate. Fig. 6.10 shows the measured wireless coverage map of the low-VHF radio, along with that of the 2.4 GHz ZigBee module in Scenario 1. The shaded regions indicate where the packet error rate (PER) is below 10 % for low-VHF experiments as well as the boundary within which the communication links are maintained for the 2.4 GHz ZigBee. Note that we use two different definitions of coverage to highlight the significantly better performance at low-VHF with the measurement parameters selected for a fair comparison. Longer-range tests were not possible in this scenario due to physical access constraints. The low-VHF radio shows much longer communication range ($>$ 280 m) and wider coverage than the XBP24 module. In addition, frequent data packet losses were observed with the 2.4 GHz ZigBee module (approximately 80 % higher) while they were far less for the low-VHF radio, within the overlapped coverage area.

Similar results are found in Scenario 2, as shown in Fig. 6.11. In this scenario, measurement with the miniature low-VHF antenna was additionally carried out to demonstrate the performance of the very compact low-VHF radio system in this complex propagation environment. Lower VHF operation establishes a longer-distance communication link with high reliability, whereas the network link from the stationary node of the XBP24 module fails immediately after the mobile node leaves the building.

To better understand these phenomena, the received signal strengths as a function of range for the two radio systems were characterized in both test scenarios. Fig. 6.12(a) is an example of the measured average RSSI as a function of distance (the mobile node with the miniature low-VHF antenna traversed along the dashed yellow line shown in Fig. 6.11), compared with a free space loss (FSL) model. Also, a classic empirical model [88] for path-loss estimation as a function of distance d is plotted, given by

$$PL\ (dB) = PL_0 + 10\gamma \times \log\left(\frac{d}{d_0}\right), \tag{6.2}$$

where d_0 is an arbitrary reference distance, PL_0 is the path loss at d_0, and γ is a path-loss exponent. This result indicates that path loss difference is on average more than 30 dB in this environment (we computed $\gamma = 3.1$ at 40 MHz, and 3.9 at 2.4 GHz). Fig. 6.12(b) depicts average PER measured with the two different radio systems as a function of range. Both the RSSI and PER are collected at 24 points for the low-VHF radio with a step size of $0.33\lambda_0$, and 61 points for the 2.4 GHz ZigBee with a step size of $0.5\lambda_0$. Averages were obtained by stopping the mobile node at each sample point, and transmitting 50 packets. A separate experiment, not shown, revealed that 50 samples were sufficient to achieve reliable PER estimates with small standard deviation of a few percent. In order to observe distinct fading effects in this propagation channel, an additional measurement for the 2.4 GHz ZigBee is also performed with higher transmit power (18 dB higher than the level corresponding to a fair comparison).

Comparing the two systems, the size of most scatterers in the propagation channel are only a small fraction of the wavelength at low VHF, and thus signal penetration is significantly better compared to microwave frequencies. In Scenario 2, the channel path loss is also influenced by the height and location (the difference between the stationary and mobile nodes is 3.5 m) of the antennas. As stated before, the physical antenna heights above the ground level for both radios are set to be the same by mounting the radios on identical mobile platforms. Hence, the 2.4 GHz ZigBee module has an advantageous operating condition to reduce the effect of ground reflections that would diminish the radiation performance. Furthermore, signal fluctuations are much more significant at 2.4 GHz due to multi-path effects caused by reflection, scattering, and diffraction

from the large number of scatterers in the environment. As expected, the induced small-scale fading at 2.4 GHz results in significant RSSI fluctuation and corresponding dropped packets. In contrast, fading effects are minimal at 40 MHz, resulting in a much more consistent and stable performance.

6.5 Summary

We have demonstrated seamless compact, low-power ($<$ 10 mW), low-VHF communications utilizing a bi-directional frequency converter and an off-the-shelf ZigBee module in various complex indoor/outdoor scenarios (also see Appendix E). The frequency conversion system was carefully designed for minimal power usage and maximal insertion gain and system sensitivity. A small-form-factor antenna was developed and tested. Because this antenna has a much higher efficiency compared to similar-sized antennas, low-power operation at longer range is possible. Extensive measurements for performance evaluation were conducted in highly cluttered environments. Comparison tests using a commercial ZigBee module operating at 2.4 GHz were also carried out. The measurement results demonstrate that low-VHF operation can provide highly reliable point-to-point communications in complex propagation environments.

CHAPTER VII

Conclusion and Future Work

7.1 Conclusion

Low frequency bands have both pros and cons when employed in wireless mobile communications applications: they have LOS-like propagation properties in complex propagation environments, but confront problems with limited system bandwidth and the design of compact systems because of the required antennas for the systems. To overcome such problems, we have introduced technology innovations enabling compact, low-power, mobile low frequency networking with high reliability in cluttered environments by virtue of favorable propagation properties. To find the optimal frequency range considering antenna size for compact mobile systems and propagation characteristics, we have performed physics-based simulations and extensive measurements in various scenarios with the NLOS setup. From the studies, optimal frequencies have been chosen within the low-VHF band where small-scale fading is minimal and phase distortion of transmit signals is small in such complex scenarios.

In order to achieve very compact mobile systems at the low-VHF band, we have developed a highly miniaturized antenna. This antenna is designed based on a modified T-type 180-degree phase shifter to enhance its radiation efficiency. To minimize power losses from the antenna structure, optimized high Q air-core inductors and an air-filled parallel-plate capacitor in the phase shifter are utilized. This antenna has a much higher radiation efficiency with the largest dimension

of $0.02\lambda_0$ at 40 MHz compared to those of similar-sized antennas. The antenna also provides a vertically polarized, nearly omnidirectional radiation pattern that is suitable for near-ground communications.

At the expense of size reduction and enhanced efficiency, this antenna has a relatively narrow bandwidth (0.35 %), which limits its practical applications. To overcome this limit, we have presented a new approach for antenna impedance matching with non-Foster elements, which is free from the gain-bandwidth-size constraint of a small passive antenna. Challenging issues with respect to the design of the non-Foster matched antenna, such as antenna impedance modeling and system stability, are fully addressed in Chapter IV. With the proposed approach, 3 dB power bandwidth is improved more than two times with a power efficiency advantage ($1.3 < \eta_{adv} < 5.9$ in the bandwidth). Thus, the miniature low-VHF antenna with the non-Foster matching solving practical limits is very effective for compact, low-power, short-range, wireless transmission systems.

To surmount difficulties in accurate characterization of low frequency antennas resulting from their long wavelengths, we have developed a powerful approach based on very-near-field measurements with electro-optical systems, which can be performed without a costly large anechoic chamber facility. To compute far-field quantities of the antenna, a new near-field to far-field transformation formula has also been introduced. The reciprocity theorem along with the induced surface current excited by a plane wave on a metallic box in place of the scanned surfaces enclosing the antenna for very-near-field measurements is applied in the formula. Measurement results with the miniature low-VHF antenna presented in Chapter III validate the forcefulness of the proposed characterization technique that greatly contributes to the ease of low-frequency antenna measurements.

We have demonstrated compact, low-power, short-range, mobile networking at low VHF with small, off-the-shelf ZigBee radio incorporating the developed frequency conversion circuit. Allowing for low-power operation and compactness of the mobile radio system, the frequency converter is optimally designed and the aforementioned miniature antenna is also used. The results from performance characterization, along with a comparison test using a commercial 2.4 GHz radio in complex propagation scenarios, show that the proposed radio provides exceptionally reliable communication links in a much longer range, in contrast with the 2.4 GHz radio. Hence, the compact, low-power, low-VHF radio is a good candidate for wireless mobile ad-hoc networks requiring consistent and persistent reliable communications in harsh propagation environments.

7.2 Future Work

7.2.1 Electrically Tunable Miniature Low-VHF Antenna

As an alternative way to cover a broader bandwidth with the miniature low-VHF antenna, an electrically tunable scheme with respect to the antenna resonant frequency can be considered. As described in Chapter III, the miniature antenna is designed to operate at resonance that is dependent upon the values of the rectangular air-core inductors and the dimension of the capacitive loading in the antenna structure; in other words, the resonant frequency of the antenna can simply be tuned by modifying the coils or the capacitive loading in the structure. Fig. 7.1 shows an example of the frequency tuning as a function of the number of turns N of the coil (N varies from 9 to 12, which corresponds to the range of inductance values from 3.5 μH to 5.2 μH), obtained from full-wave EM simulation. One of the applicable methods to electrically tune the resonant

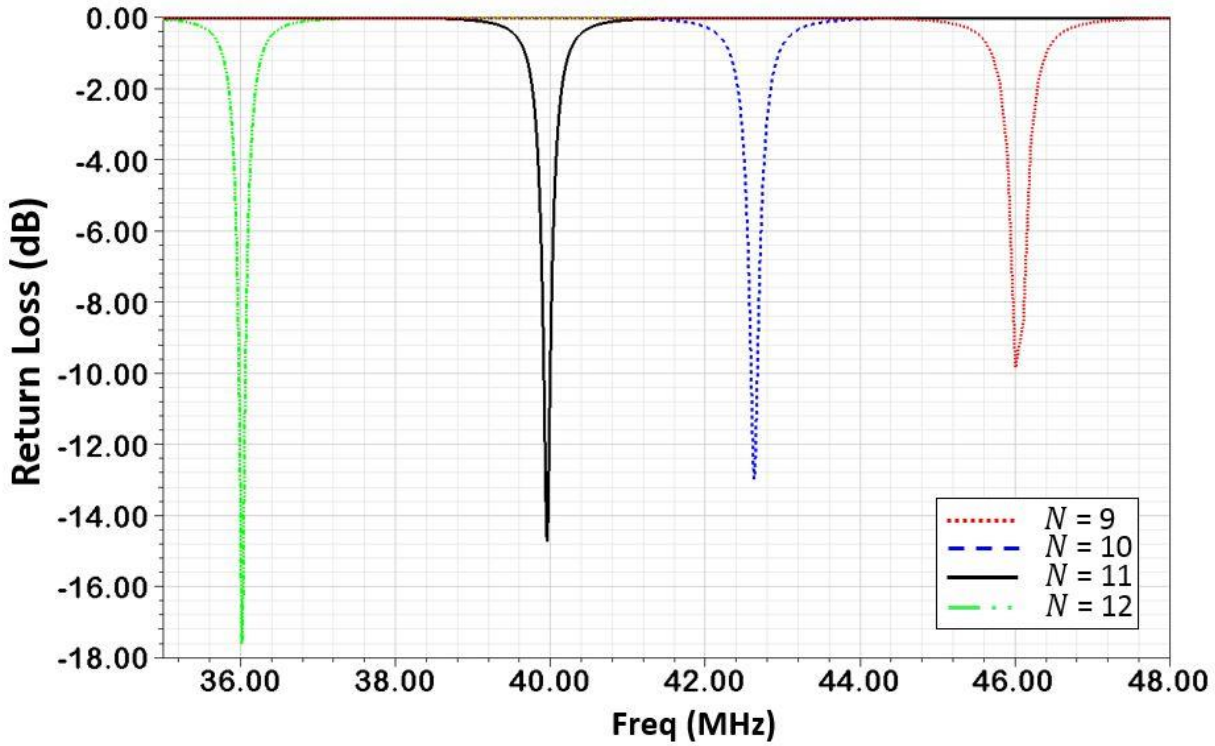

Figure 7.1: Variations of the antenna resonant frequency as a function of the number of turns of the coils.

frequency without increasing antenna size is the use of ferromagnetic materials whose permeability is highly dependent on external magnetic fields inside or outside the coils to change their inductances, resulting in the resonance shift [89]. Another way to control the coil inductance is the use of multiple P-N junction diodes acting as a switch to electrically adjust N of the coils. In consideration of frequency agility, tuning range, design complexity, and losses added by a method for practical applications, an electrically tunable miniature low-VHF antenna should be carefully designed to cover a wider frequency range with low return loss.

7.2.2 Improvement of an Electro-Optical Very-Near-Field Measurement System

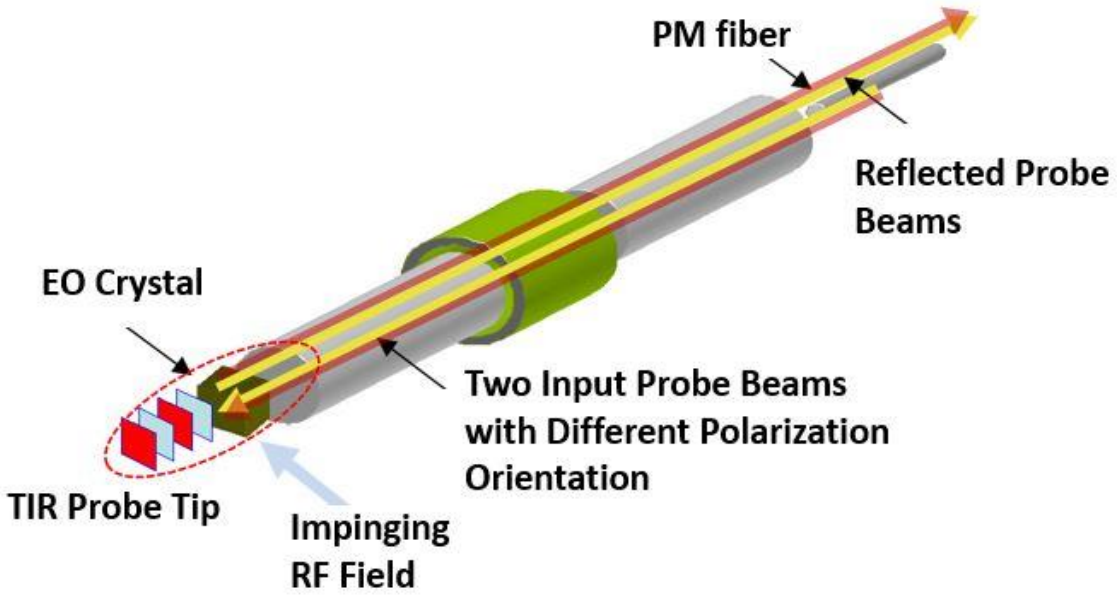

Figure 7.2: Simplified concept for simultaneously sensing two orthogonal components of the tangential electric field using a total internal reflection (TIR) probe tip with two probe beams having the same propagation path but different input polarization orientation.

In Chapter V, very-near-field measurements using EO systems have been presented to effectively characterize low frequency antennas. For near-field to far-field transformation, two orthogonal components of the tangential electric field are measured using an EO probe made of an EO crystal mounted at the tip of an optical fiber. This step involves repetitive measuring each tangential component on each scanned surface (see Fig. 5. 2) by manual rotation of the principal axis of the EO crystal, which results in increased measurement time. To simplify this step, a rotation modulation scheme on the principal axis can be introduced [90]. As shown in Fig. 7.2, by using two probe beams with the same propagation path, but different input polarization orientation for the total internal reflection (TIR) probe tip, the two orthogonal components of the tangential electric field can be measured simultaneously.

Figure 7.3: Possible application using multiple low-VHF radios proposed in Chapter VI: Incorporating the radios onto autonomous agents, corroborative sensing and mapping can be performed for challenging complex environments.

7.2.3 RF-Based Localization with the Compact Low-VHF Radios

As demonstrated in Chapter VI, the compact ZigBee-based radio seamlessly operating at low-VHF band provides high reliability in wireless link for challenging complex propagation environments. This low-VHF radio can therefore be utilized for RF-based tracking and localization, as well as empirical propagation modeling in such environments (e.g., obstacle-rich indoor scenes, dense forests, underground tunnels). Employing the RSSI values provided by the radio as a function of the distance from beacons to a mobile node, the RSS spatial gradient can be obtained and used as a direction of arrival (DOA) estimator [91]. Furthermore, autonomous multi-user and multi-node mobile networking can be applied with multiple low-VHF radios along with autonomous mobile robotic platforms (see Fig. 7.3) for corroborative sensing and mapping.

7.3 List of Publications

The contributions of this thesis have been published in the following peer-reviewed journal articles and conference proceedings. Some works are currently under review or will be submitted for publication.

Referred Journal Articles

- J. Choi, F. T. Dagefu, B. M. Sadler, and K. Sarabandi, "A Highly Miniaturized, Non-Foster Matched Low-VHF Antenna for Low-Power, Short-Range, Wireless Transmission Systems," *IEEE Antennas and Wireless Propagation Letters*, to be submitted.
- J. Choi, F. T. Dagefu, B. M. Sadler, and K. Sarabandi, "ZigBee-Based Low-VHF Enhanced Networking in Complex Environments," *IEEE Transactions on Antennas and Propagation*, under review.
- K. Sarabandi, J. Choi, A. Sabet, K. Sabet, "Pattern and Gain Characterization Using Non-Intrusive Very-Near-Field Electro-Optical Measurements over Arbitrary Closed Surfaces," *IEEE Transactions on Antennas and Propagation*, vol. 65, no. 2, pp. 489-497, Feb. 2017.
- F. T. Dagefu, G. Verma, J. Choi, B. M. Sadler, and K. Sarabandi, "Low-Power Low-Frequency Communications in Complex Environments with Miniature Antennas," *IEEE Antennas and Propagation Magazine*, to be submitted.
- J. Choi, F. T. Dagefu, B. M. Sadler, and K. Sarabandi, "Electrically Small Folded Dipole Antenna for HF and Low-VHF Bands," *IEEE Antennas and Wireless Propagation Letters*, vol. 15, pp. 718-721, Mar. 2016.

- F. T. Dagefu, J. Choi, M. Sheikhsofla, B. M. Sadler, and K. Sarabandi, "Performance Assessment of Lower VHF Band for Short Range Communication and Geolocation Applications," *Radio Science*, vol. 50, pp. 443-452, May 2015.
- J. Oh, J. Choi, F. T. Dagefu, and K. Sarabandi, "Extremely Small Two-Element Monopole Antenna for HF Band Applications," *IEEE Transactions on Antennas and Propagation*, vol. 61, pp. 2991-2999, Jun. 2013.
- F. T. Dagefu, J. Oh, J. Choi, and K. Sarabandi, "Measurements and Physics-based Analysis of Co-located Antenna Pattern Diversity System," *IEEE Transactions on Antennas and Propagation*, vol. 61, pp. 5724-5734, Nov. 2013.

Conference Proceedings

- J. Choi and F. T. Dagefu, B. M. Sadler, and K. Sarabandi, "A Non-Foster Matched Dipole for A Low-VHF Mobile Transmitter System," *2017 IEEE AP-S/URSI*, San Diego, California, July 2017.
- J. Choi and F. T. Dagefu, B. M. Sadler, and K. Sarabandi, "A Compact, Low-Power, Low-VHF Radio for Mobile and Wireless Communication Applications," *2016 IEEE AP-S/URSI*, Fajardo, Puerto Rico, June 2016.
- J. Choi and K. Sarabandi, "Non-Foster Impedance Matching of an Extremely Small Folded-Dipole Antenna at Low-VHF Band," *2016 IEEE AP-S/URSI*, Fajardo, Puerto Rico, June 2016.
- J. Choi and K. Sarabandi, "Full-Spherical Radiation Pattern Evaluation of Low Frequency Antennas Using a Novel Very-Near-Field Electro-Optical System," *2016 IEEE AP-S/URSI*, Fajardo, Puerto Rico, June 2016.

- F. T. Dagefu, G. Verma, J. Choi, B. M. Sadler, and K. Sarabandi, "Empirical and Simulation based Analysis of Propagation Mechanisms at Low Frequencies," *2016 IEEE AP-S/URSI*, Fajardo, Puerto Rico, June 2016.
- J. Choi and K. Sarabandi, "HF/VHF Antenna Characterization from Very-Near-Field Measurements over Arbitrary Closed Surfaces," *USNC-URSI National Radio Science Meeting*, Boulder, CO, USA, January 2016.
- J. Choi, A. Sabet, K. Sabet, and K. Sarabandi, "Near-Field Characterizations of a Miniaturized Low-VHF Omni-directional Antenna Using an Electro-Optical System," *2015 IEEE AP-S/URSI*, Vancouver, BC, Canada, July 2015.
- J. Choi and K. Sarabandi, "Highly Miniaturized Low-VHF Folded Dipole Antenna for Compact, Mobile Communication Applications," *2014 IEEE AP-S/URSI*, Memphis, TN, USA, July 2014.
- J. Choi and K. Sarabandi, "An extremely low-profile MF monopole antenna design and measurement," *2013 IEEE AP-S/URSI*, Orlando, FL, USA, July 2013.
- J. Choi, M. Sheikhsofla, and K. Sarabandi, "Near-ground wave propagation measurements at VHF ISM band," *2013 IEEE AP-S/URSI*, Orlando, FL, USA, July 2013.
- F. T. Dagefu, J. Oh, J. Choi, and K. Sarabandi, "Performance analysis of a common aperture antenna diversity system," *2013 IEEE AP-S/URSI*, Orlando, FL, USA, July 2013.

APPENDICES

Appendix A

Wave Propagation Measurement Setup and Results

Figure A.1: Near-ground wave propagation measurement setup for each transmitting (left) and receiving (right) systems.

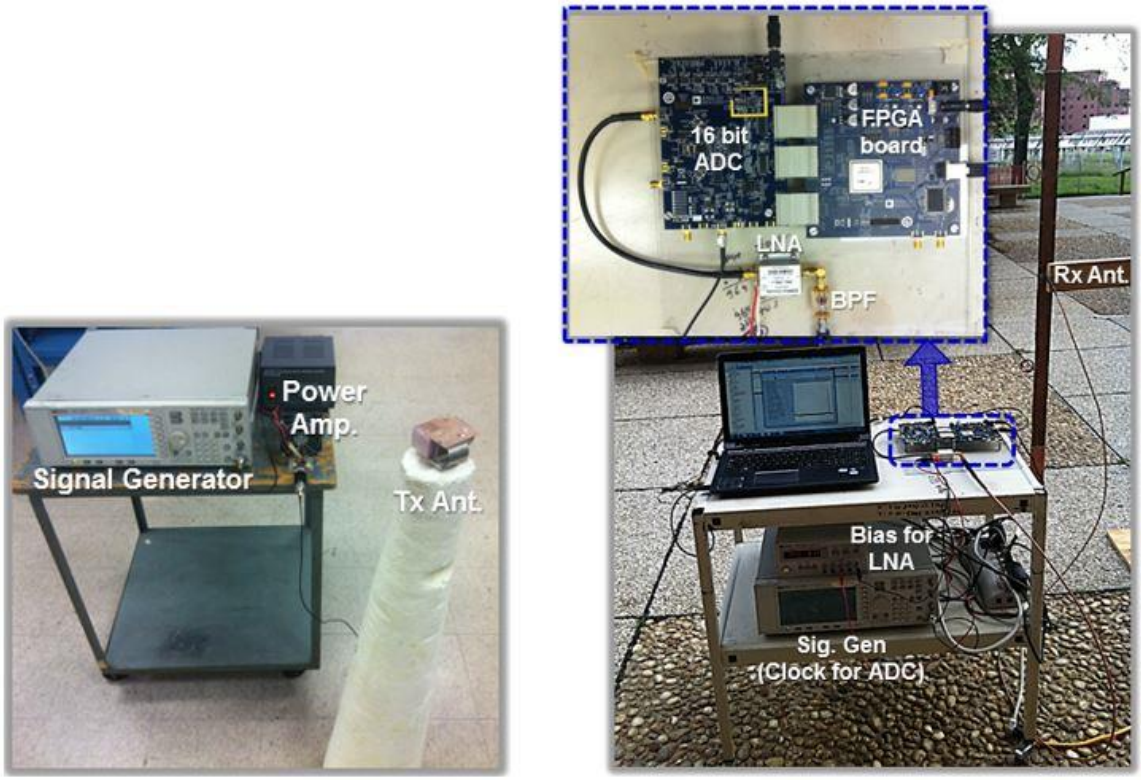

Figure A.2: Measurement results performed on the third floor of the EECS building at the University of Michigan: A set of antennas polarized differently (VV or HH) are utilized to investigate effects of metallic objects (e.g., steel studs) on the wave propagation at low VHF.

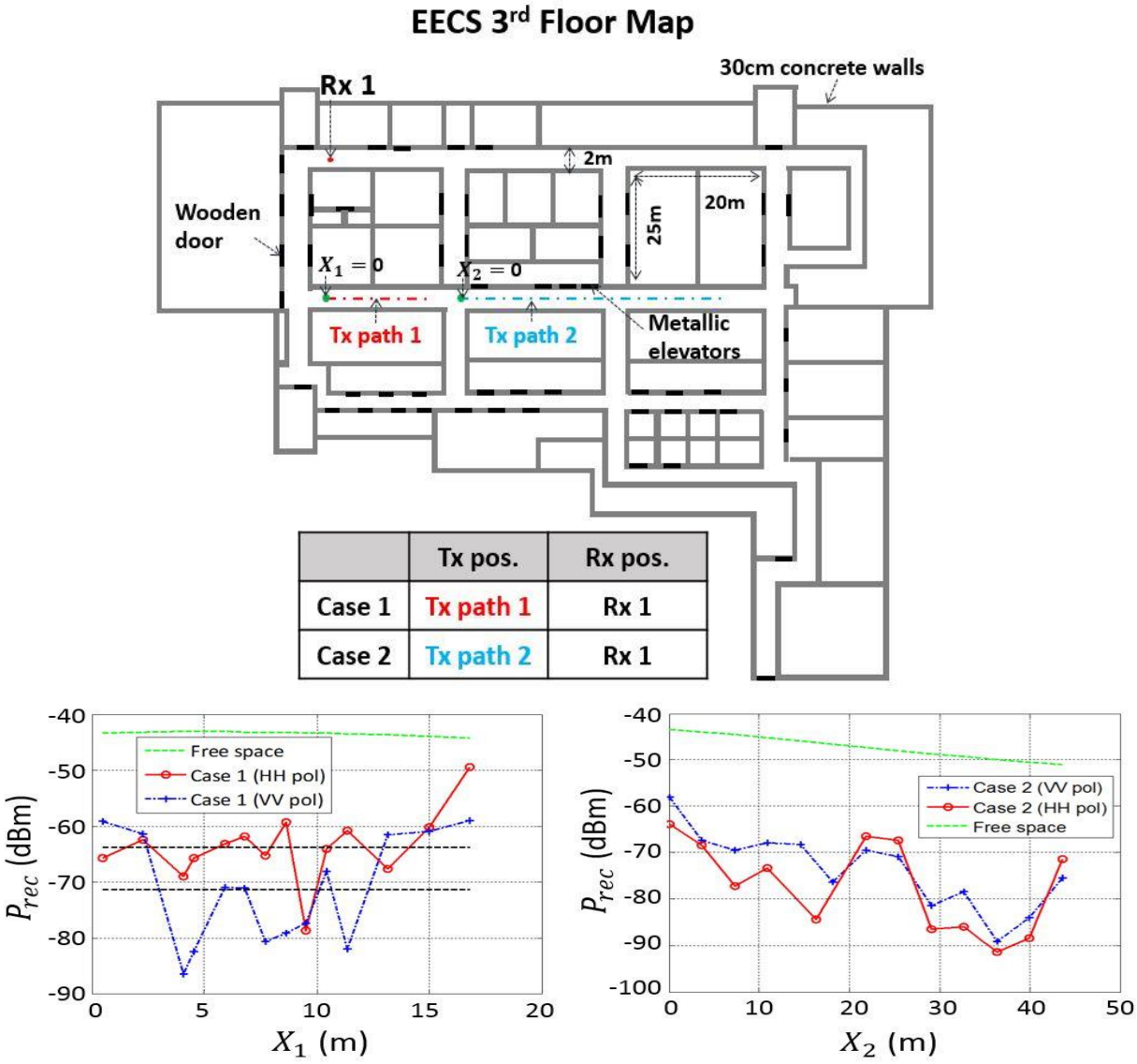

	Tx pos.	Rx pos.
Case 1	Tx path 1	Rx 1
Case 2	Tx path 2	Rx 1

Appendix B

Actual Setup for a Far-Field Measurement in an Elevated Outdoor Range

Figure B.1: Actual measurement setup for applying substitution method in order to characterize the miniature low-VHF antenna.

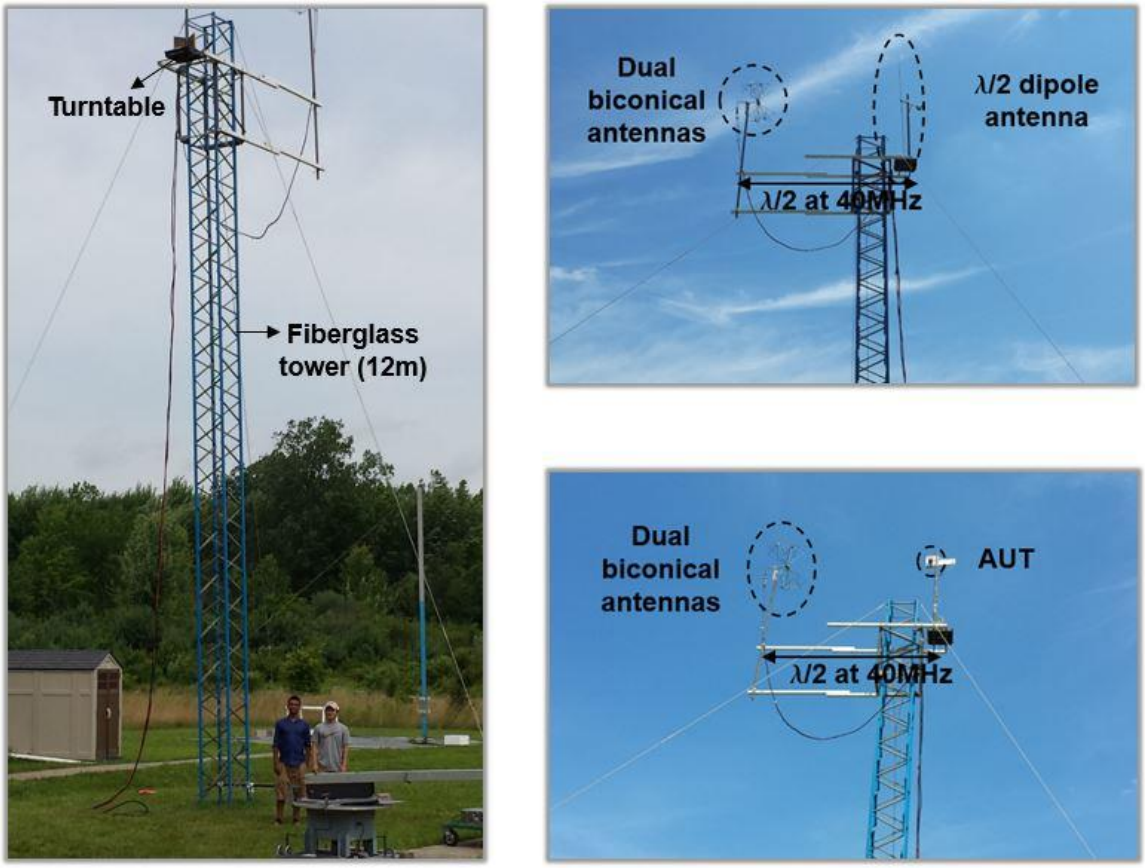

Figure B.2: A fabricated small source module generating 11 dBm at 40 MHz to examine effects of a feed cable on the antenna under test.

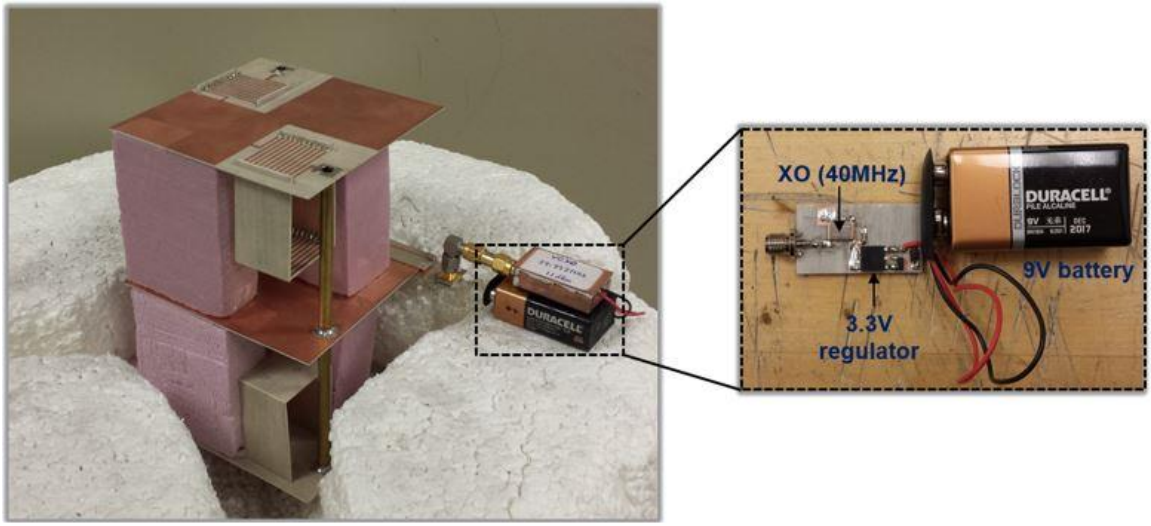

Appendix C

A Non-Foster Matched Dipole ($0.167\lambda_0$ in height at 40 MHz) for a Low-VHF Mobile Transmitter System

Figure C.1: (a) A fabricated miniature dipole and (b) its impedance circuit model.

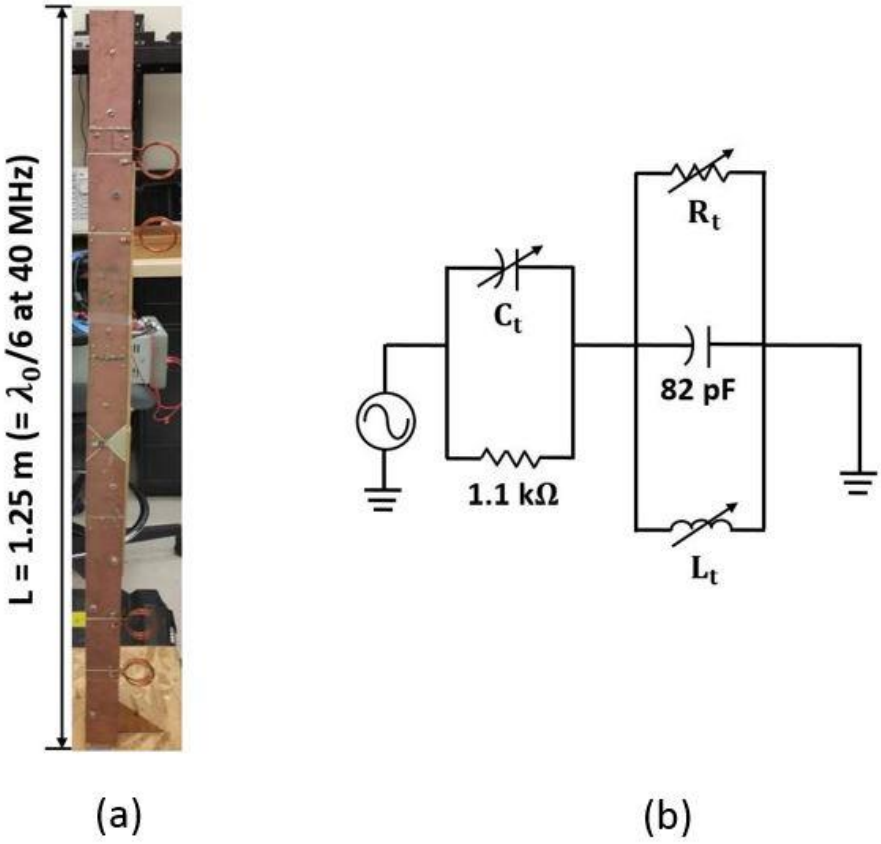

Figure C.2: Comparison of return losses (passive matching vs. active matching).

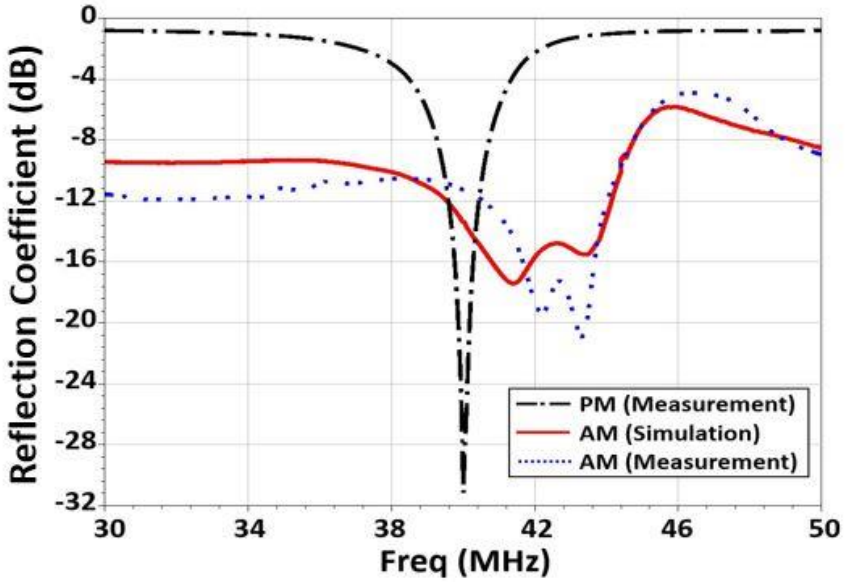

Figure C.3: Comparison of transmission coefficients (passive matching vs. active matching as a function of DC biasing for the negative impedance converter).

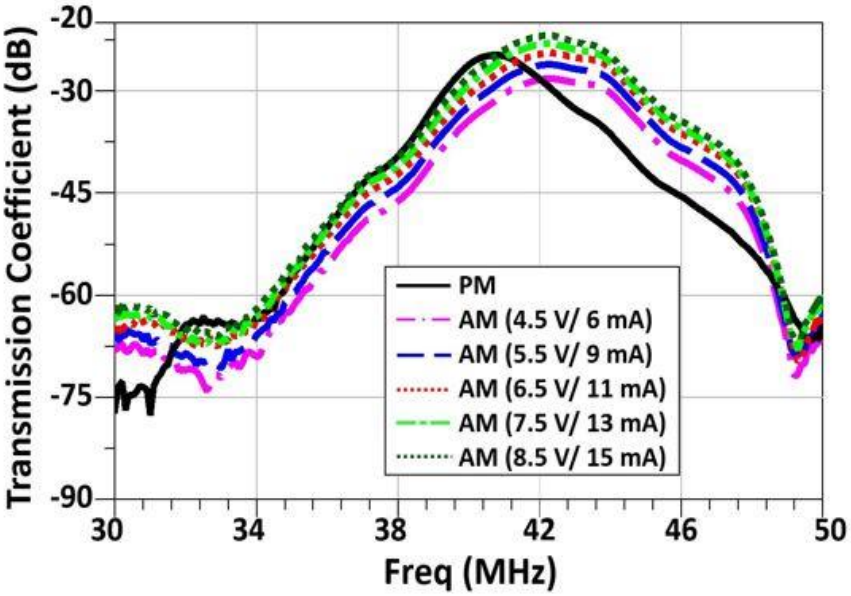

Appendix D

Very-Near-Field Measurements Using an Electro-Optical System

Figure D.1: Optimization process of the EO system monitoring the fluctuations of the total power detected by photodetectors (PD) and the EO signal.

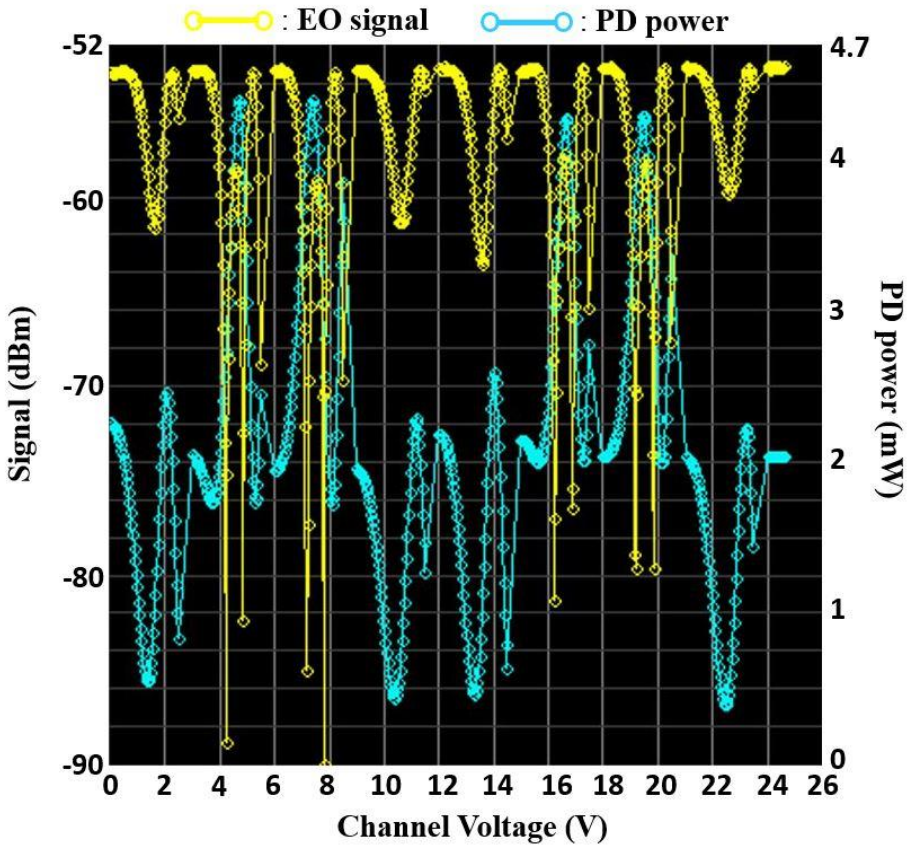

Figure D.2: Simulated and measured very-near-field maps showing the tangential components (magnitudes and phases) of the electric fields on the back, bottom, and right of the imaginary box shown in Fig. 5.2.

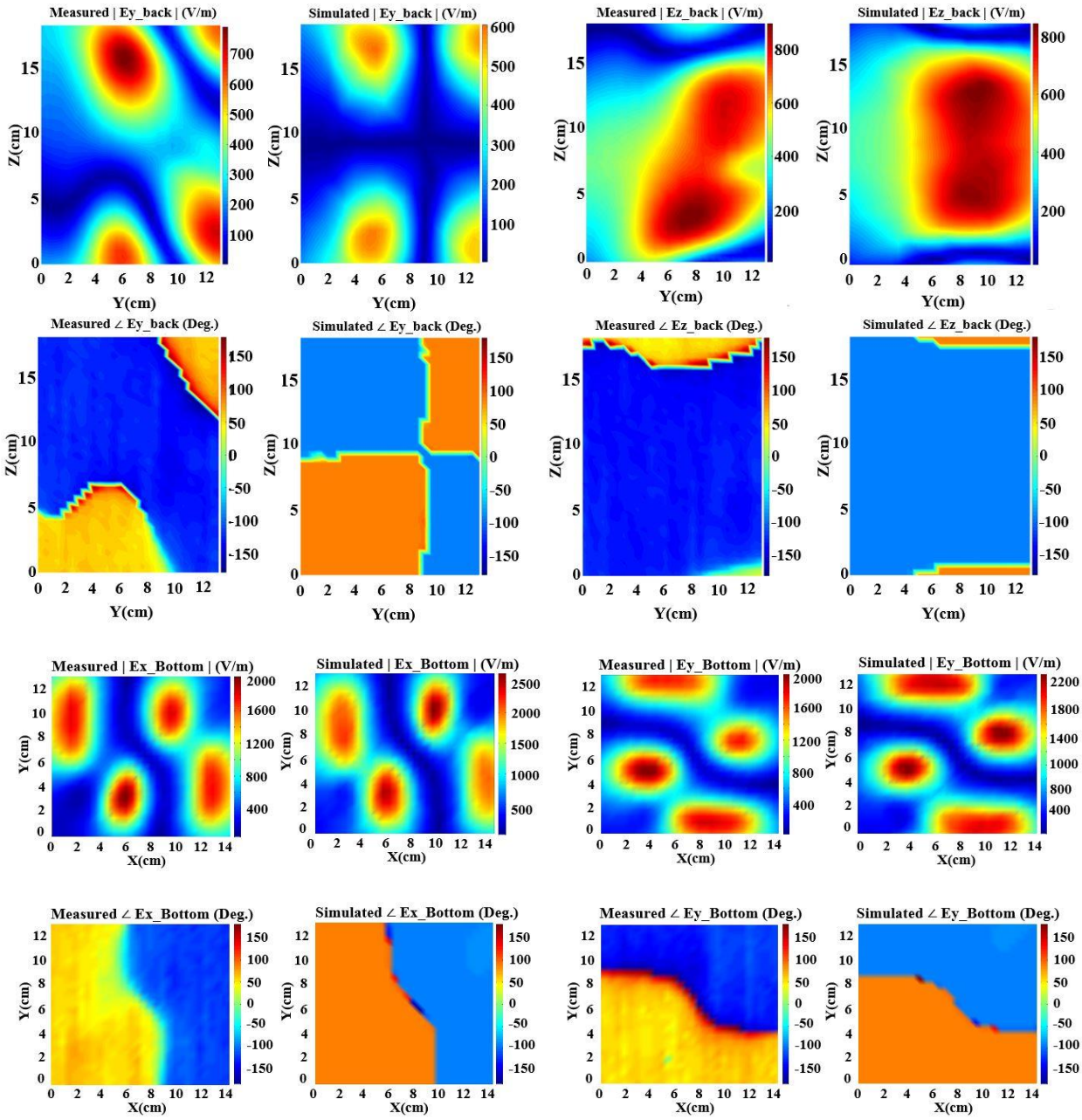

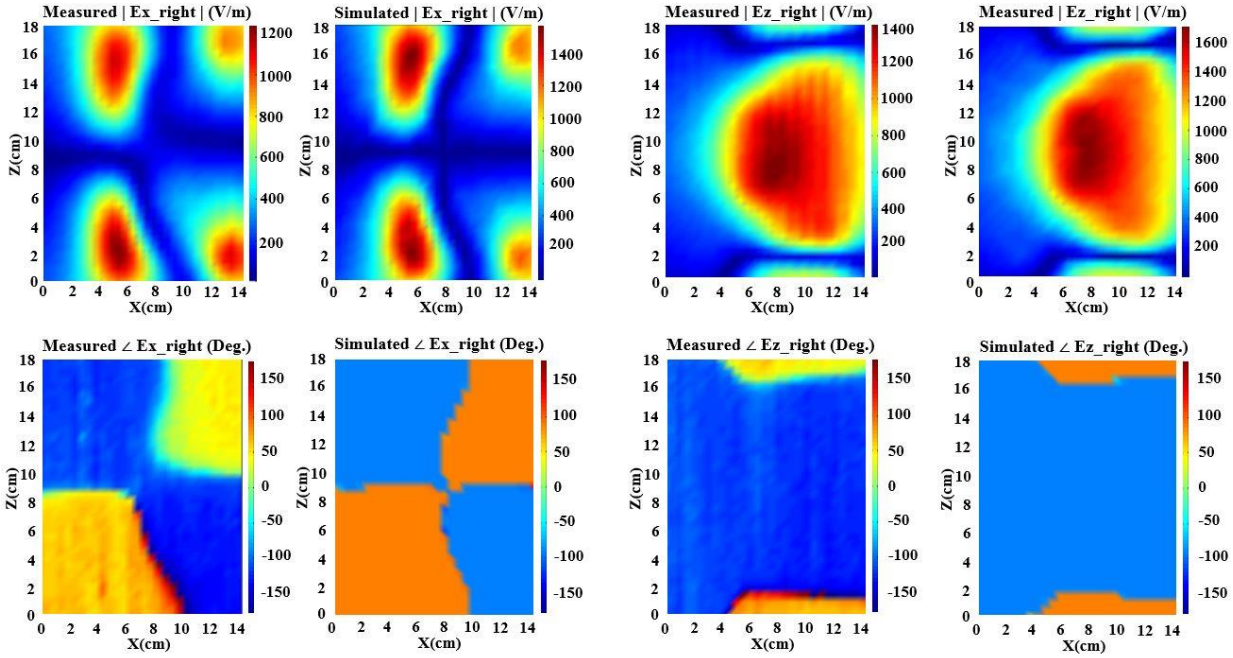
Measured | Ex_right | (V/m)
Simulated | Ex_right | (V/m)
Measured | Ez_right | (V/m)
Measured | Ez_right | (V/m)
Measured ∠ Ex_right (Deg.)
Simulated ∠ Ex_right (Deg.)
Measured ∠ Ez_right (Deg.)
Simulated ∠ Ez_right (Deg.)
Z(cm)
X(cm)

Appendix E

Performance Test of a Compact, Low-Power, Low-VHF Radio in a Complex Propagation Environment

Figure E.1: Measured antenna impedance as a function of height above the small autonomous platform shown in Fig. 6.7(b).

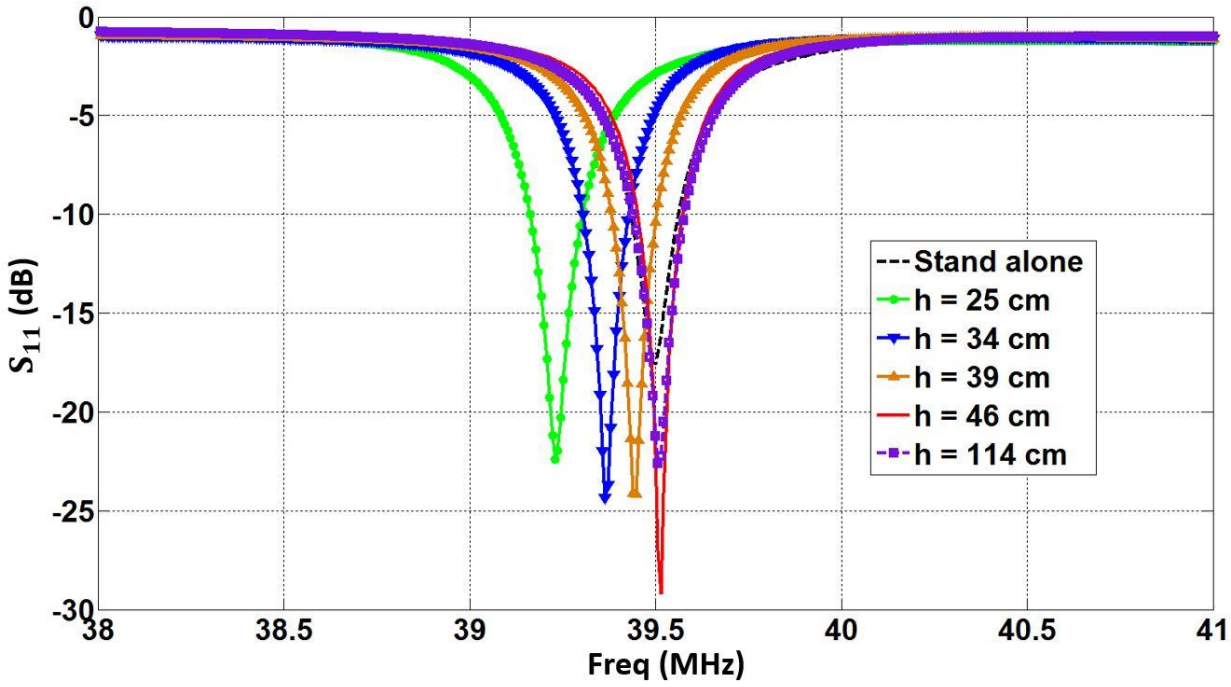

Figure E.2: Comparison results of the communication coverage (with (a) compact low-VHF radios and (b) 2.4 GHz ZigBee radios) conducted on the third floor of the EECS building at the University of Michigan.

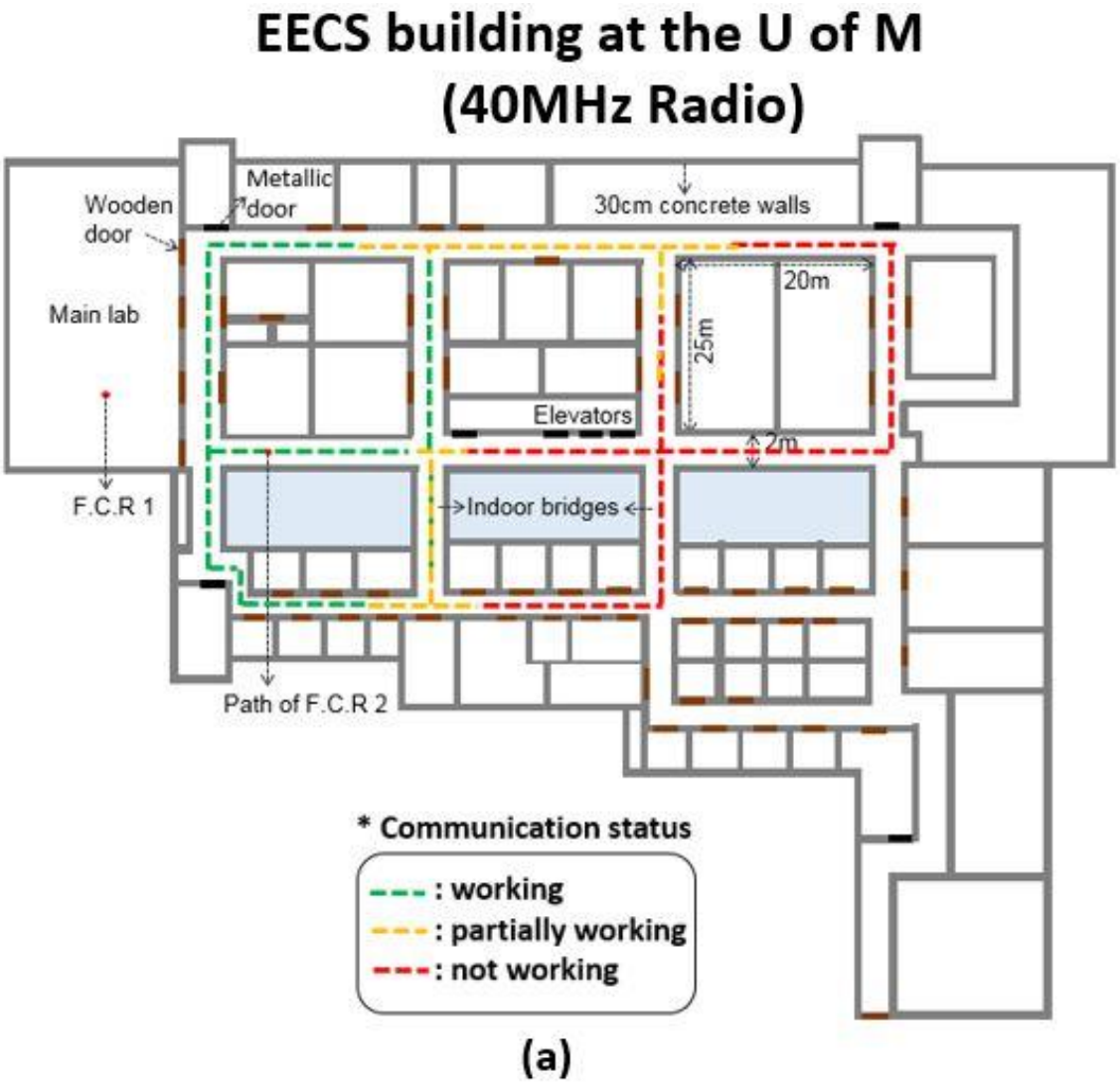

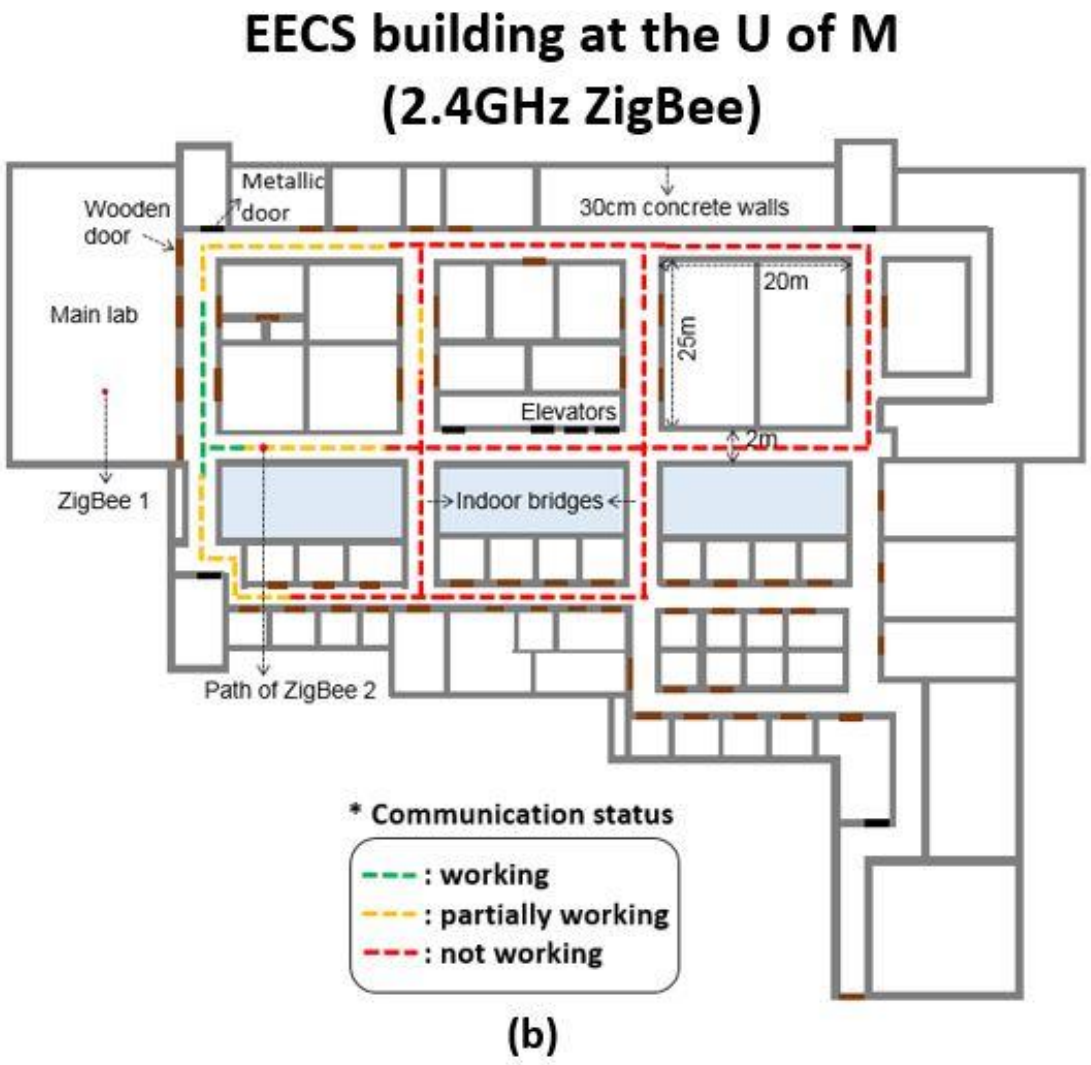

Stationary nodes are located inside the laboratory (Main lab in the figure) and mobile nodes are moved along the hallway on the third floor of the EECS building at the University of Michigan. The green dotted line indicates where the radios are successfully communicated each other (PER $<$ 10 %). The yellow dotted line denotes where the radios frequently fail to transmit and receive data packets due to signal fluctuations, and the red dotted line represents where the communication links between the radios are disconnected.

BIBLIOGRAPHY

BIBLIOGRAPHY

[1] K. Guan, Z. Zhong, J. Alonso, C. Briso-Rodriguez, "Measurement of distributed antenna systems at 2.4 GHz in a realistic subway tunnel environment," *IEEE Trans. Veh. Technol*., vol. 61, no. 2, pp. 834-837, Feb. 2012.

[2] A. Sheth, S. Nedevschi, R. Patra, S. Surana, E. Brewer, and L. Subramanian, "Packet loss characterization in WiFi-based long distance networks," *INFOCOM 2007. 26th IEEE Int. Conference on Comput. Commun.*, pp. 312-320, May 2007.

[3] G. J. Janssen, P. Stigter, and R. Prasad, "Wideband indoor channel measurements and BER analysis of frequency selective multipath channels at 2.4, 4.75, and 11.5 GHz," *IEEE Trans. Commun.*, vol. 44, no. 10, pp. 1272-1288, Oct. 1996.

[4] J.B. Andersen, T.S. Rappaport, and S. Yoshida, "Propagation measurements and models for wireless communications channels," *IEEE Communications Magazine*, vol. 33, no.1, pp.42-49, Jan. 1995.

[5] Z. Sheng, K. K. Leung, and Z. Ding, "Cooperative wireless networks: from radio to network protocol designs," *IEEE Commun. Mag.*, vol. 49, no. 5, pp. 64-69, May 2011.

[6] C. Oestges, and B. Clerckx, MIMO wireless communications: From real-world propagation to space-time code design. Academic Press, 2010.

[7] F. T. Dagefu, J. Oh, J. Choi, and K. Sarabandi, "Measurements and Physics-based Analysis of Co-located Antenna Pattern Diversity System," *IEEE Trans. Antennas Propag*., vol. 61, no. 11, pp. 5724-5734, Jun. 2015.

[8] H.T. Chattha, Y. Huang, S.J. Boyes, and X. Zhu, "Polarization and Pattern Diversity-Based Dual-Feed Planar Inverted-F Antenna," *IEEE Trans. Antennas Propag*., vol. 60, no. 3, pp. 1532-1539, Mar. 2012.

[9] C.B. Dietrich, K. Dietze, J.R. Nealy, and W.L. Stutzman, "Spatial, Polarization, and Pattern Diversity for Wireless Handheld Terminals," *IEEE Trans. Antennas Propag*., vol. 49, no. 9, pp.1271-1281, Sep. 2001.

[10] F. T. Dagefu, J. Choi, M. Sheikhsofla, B. M. Sadler, and K. Sarabandi, "Performance Assessment of Lower VHF Band for Short Range Communication and Geolocation

Applications," *Radio Science*, vol. 50, no. 5, pp. 443-452, May 2015.

[11] F. T. Dagefu, G. Verma, C. Rao, P. Yu, J. Fink, B. M. Sadler, and K. Sarabandi, "Short-Range Low-VHF Channel Characterization in Cluttered Environments," *IEEE Trans. Antennas Propag*., vol. 63, no. 6, pp. 2719-2727, Jun. 2015.

[12] F. T. Dagefu, J. Oh, and K. Sarabandi, "A sub-wavelength RF Source Tracking System for GPS-denied Environments," *IEEE Trans. Antennas Propag*., vol. 61, no. 4, pp. 2252-2262, Apr. 2013.

[13] Comrod Communication. [Online]. Available: http://www.comrod.com/getfile.php/13458/Datasheets/T%20Antennas%20-%20Military/VHF3088EF_50.pdf

[14] Alaris Antennas. [Online]. Available: http://www.alarisantennas.com/upload/brochure_files/20150827084557_OMNI-A0180-Version-1.9.pdf

[15] P. de Fornel, and H. Sizun, Radio Wave Propagation for Telecommunication Applications. Heidelberg: Springer, 2005.

[16] L.J. Ippolito, Radiowave Propagation in Satellite Communications. Springer Science & Business Media, 2012.

[17] C.F. Yang, B.C. Wu and C.J. Ko, "A ray-tracing method for modeling indoor wave propagation and penetration," *IEEE Trans. Antennas Propag*., vol. 46, no. 6, pp. 907-919, Jun. 1998.

[18] J. Walfisch and H.L. Bertoni, "A theoretical model of UHF propagation in urban environments," *IEEE Trans. Antennas Propag*., vol. 36, no. 12, pp.1788-1796, Dec. 1988.

[19] J. Oh, J. Choi, F. T. Dagefu, and K. Sarabandi, "Extremely Small Two-Element Monopole Antenna for HF Band Applications," *IEEE Trans. Antennas Propag*., vol. 61, no. 6, pp. 2991-2999, Jun. 2013.

[20] J. Choi, F. T. Dagefu, B. M. Sadler, and K. Sarabandi, "Electrically Small Folded Dipole Antenna for HF and Low-VHF Bands," *IEEE Antennas Wireless Propag. Lett*., vol. 15, pp. 718-721, Mar. 2016.

[21] J. Choi and F. T. Dagefu, B. M. Sadler, and K. Sarabandi, *"*A Non-Foster Matched Dipole for A Low-VHF Mobile Transmitter System*," 2017 IEEE AP-S/URSI,* San Diego, California, July 2017.

[22] J. Choi and F. T. Dagefu, B. M. Sadler, and K. Sarabandi, *"*A Highly Miniaturized, Non-Foster Matched Low-VHF Antenna for Low-Power, Short-Range, Wireless Transmission Systems,*" IEEE Antennas Wireless Propag. Lett*., to be submitted.

[23] K. Sarabandi, J. Choi, A. Sabet, K. Sabet, "Pattern and Gain Characterization Using Non-Intrusive Very-Near-Field Electro-Optical Measurements over Arbitrary Closed Surfaces," *IEEE Trans. Antennas Propag*., vol. 65, no. 2, pp. 489-497, Dec. 2016.

[24] J. Choi, F. T. Dagefu, B. M. Sadler, and K. Sarabandi, "ZigBee-Based Low-VHF Enhanced Networking in Complex Environments," *IEEE Trans. Antennas Propag*., under review.

[25] J. Choi, F. T. Dagefu, B. M. Sadler, and K. Sarabandi, "A Compact, Low-Power, Low-VHF Radio for Mobile and Wireless Communication Applications," *2016 IEEE AP-S/URSI*, Fajardo, Puerto Rico, June 2016.

[26] J. Choi and K. Sarabandi, "Highly miniaturized low-VHF folded dipole antenna for compact, mobile communication applications, *IEEE International Conference on Antennas Propagation*, pp. 2991–2999, Memphis, Tenn., doi:10.1109/TAP.2013.2249034.

[27] J. R. Hampton, N. Merheb, W. Lain, D. Paunil, R. Shuford, and W. Kasch, "Urban propagation measurements for ground based communication in the military UHF band," *IEEE Trans. Antennas Propag*., vol. 54, no. 2, pp. 644–654, 2006.

[28] J. Andrusenko, R. Miller, J. Abrahamson, N. Merheb Emanuelli, R. Pattay, and R. Shuford, "VHF general urban path loss model for short range ground-to-ground communications," *IEEE Trans. Antennas Propag*., vol. 56, no. 10, pp. 3302–3310, 2008.

[29] P. Ali-Rantala , L. Ukkonen, L. Sydanheimo, M. Keskilammi, and M. Kivikoski, "Different kinds of walls and their effect on the attenuation of radiowaves indoors," in *Antennas and Propagation Society International Symposium*, 2003, vol. 3, pp. 1020–1023, IEEE, Columbus, Ohio.

[30] C. Ruthroff, "Multiple-path fading on line-of-sight microwave Radio systems as a function of path length and frequency," *Bell System Tech. J*., vol. 50, no.7, pp. 2375–2398, 1971.

[31] J. A. Pugh, R. Bultitude, and P. J. Vigneron, "Path loss measurements with low antennas for segmented wideband communications at VHF," in *Military Communications Conference, 2006. MILCOM 2006*, pp. 1–5, IEEE, Washington, D. C.

[32] D. Liao, and K. Sarabandi, "Near-Earth wave propagation characteristics of electric dipole in presence of vegetation or snow layer," *IEEE Trans. Antennas Propag*., vol. 53, no. 11, pp. 3747–3756, 2005.

[33] C. Holloway, P. Perini, R. DeLyser, and K. Allen, "Analysis of composite walls and their effects on short-path propagation modeling," *IEEE Trans. Veh. Technol*., vol. 46, no. 3, pp.

730–738, 1997.

[34] J. F. LaFortune, and M. Lecours, “Measurement and modeling of propagation losses in a building at 900 MHz,” *IEEE Trans. Veh. Technol*., vol. 39, no. 2, pp. 101–108, 1990.

[35] F. Dagefu, and K. Sarabandi, “Analysis and modeling of near-ground wave propagation in the presence of building walls,” *IEEE Trans. Antennas Propag*.,” vol. 59, no. 6, pp. 2368–2378, 2011.

[36] X. Zhang, T. Burress, K. Albers, and W. Kuhn, “Propagation comparisons at VHF and UHF frequencies,” *in Radio and Wireless Symposium*, 2009. RWS ’09, pp. 244–247, IEEE.

[37] H. Moon, G.-Y. Lee, C.-C. Chen, and J. L. Volakis, “An extremely low-profile ferrite-loaded wideband VHF antenna design,” *IEEE Antennas Wirel. Propag. Lett.*, vol. 11, pp. 322–325, 2012.

[38] Liao, D., and K. Sarabandi, “Terminal-to-terminal hybrid full-wave simulation of low-profile, electrically-small, near-ground antennas,” *IEEE Trans. Antennas Propag*., vol. 56, no. 3, pp. 806–814, 2008.

[39] F. T. Dagefu, G. Verma, C. R. Rao, P. L. Yu, J. R. Fink, B. M. Sadler, and K. Sarabandi (2015), Short-range Low-VHF channel characterization in cluttered environments, *IEEE Trans. Antennas Propag*., 63(6), 1, doi:10.1109/TAP.2015.2418346.

[40] S-M. Moon, H-K. Ryu, J-M. Woo, and H. Ling, "Miniaturisation of λ/4 microstrip antenna using perturbation effect and plate loading for low-VHF-band applications," *Electronics Letters*, vol. 47, no. 3, pp. 162-164, Feb. 2011.

[41] M. Murugan and V. K. Kokate , "Low profile VHF antenna for mobile communication," India Annual Conference, 2004. *Proceedings of the IEEE INDICON 2004. First*, pp. 392-394.

[42] K. Sarabandi and R. Azadegan, “Design of an Efficient Miniaturized UHF Planar Antenna,” *IEEE Trans. On Ant. & Prop*., vol. 51, no. 6, pp. 1270-1276, Jun. 2003.

[43] R. Azadegan and K. Sarabandi, “A Novel Approach for Miniaturization of Slot Antennas,” *IEEE Trans. On Ant. & Prop*., vol. 51, no. 3, pp. 421-429, Mar. 2003.

[44] C. A. Balanis, Antenna theory: analysis and design. John Wiley & Sons, 2012, pp. 515-521.

[45] M. K. Mills, "Self inductance formulas for multi-turn rectangular loops used with vehicle detectors," *Vehicular Technology Conference, 33rd IEEE*, 1983, vol. 33, pp. 65-73.

[46] S. C. Snowdon, "AC resistance of rectangular coil," *Fermi National Accelerator Laboratory*

(FNAL), Batavia, IL, No. FERMILAB-FN-0111, Jan. 1968.

[47] IEEE standard test procedures for antennas, ANSI/IEEE Std 149-1979.

[48] T. Zwick, W. Wiesbeck, J. Timmermann, and G. Adamiuk, Ultra-wideband RF System Engineering. Cambridge University Press, 2013, pp. 36-43.

[49] L. J. Chu, "Physical limitations of omni-directional antennas," *J. Appl. Phys*., vol. 19, no. 12, pp. 1163-1175, Dec. 1948.

[50] H. A. Wheeler, "Fundamental limitations of small antennas," *Proc. IRE*, vol. 35, no. 12, pp. 1479–1484, Dec. 1947.

[51] S. E. Sussman-Fort and R. M. Rudish, "Non-Foster impedance matching of electrically-small antennas," *IEEE Trans. Antennas Propag*., vol. 57, no. 8, pp. 2230–2241, Aug. 2009.

[52] M. M. Jacob and D. F. Sievenpiper, "Gain and Noise Analysis of Non-Foster Matched Antennas," *IEEE Trans. Antennas Propag*., vol. 64, no. 12, pp. 4993-5004, Dec. 2016.

[53] C. R. White, J. S. Colburn, R. G. Nagele, "A non-Foster VHF monopole antenna," *IEEE Antennas Wireless Propag. Lett.*, vol. 11, pp. 584-587, Jun. 2012.

[54] J. G. Linvill, "Transistor negative-impedance converters," *Proc. IRE*, vol. 41, no. 6, pp. 725–729, Jun. 1953.

[55] B. Razavi, "The Cross-Coupled Pair-Part III," *IEEE Solid State Circuits Mag*., vol. 7, no. 1, pp. 10-13, 2015.

[56] G. Gonzalez, Microwave Transistor Amplifiers: Analysis and Design. Upper Saddle River, NJ, USA: Prentice hall, 1997.

[57] L. Mattioni and G. Marrocco, "Design of a Broadband HF Antenna for Multimode Naval Communications," *IEEE Antennas Wireless Propag. Lett*., vol. 4, pp. 179-182, 2005.

[58] G. Virone, A. M. Lingua, M. Piras, A. Cina, F. Perini, J. Monari, F. Paonessa, O. A. Peverini, G. Addamo, and R. Tascone, "Antenna Pattern Verification System Based on a Micro Unmanned Aerial Vehicle," *IEEE Antennas Wireless Propag. Lett*., vol. 13, pp. 169-172, 2014.

[59] G. E. Baker, "Measurement of the Radiation Patterns of Full-scale HF and VHF Antennas," *IEEE Trans. Antennas Propag*., vol. 21, no. 4, pp. 538-544, Jul. 1973.

[60] G. L. Fur, L. Duchesne, L. Durand, A. Bellion, and D. Belot, "Feasibility of indoor spherical near field antenna measurement facility in VHF range," *Antenna Technology and Applied*

Electromagnetics (ANTEM), 15th Int. Symp., pp. 1-7, Jun. 2012.

[61] S. Villers, and A. Malhage, "VHF probes for antenna measurement in a near field range," *Antenna Measurements & Applications (CAMA), IEEE Conference*, pp. 1-4, Nov. 2014.

[62] D. Serafin, J. L. Lasserre, J. Bolomey, G. Cottard, P. Garreau, F. Lucas, and F. Therond, "Spherical near-field facility for microwave coupling assessments in the 100 MHz-6 GHz frequency range", *IEEE Trans. on Electromagn. Compat*., vol. 40, no. 3, pp. 225 – 234, Aug. 1998.

[63] Emag Technologies, Inc. [Online]. Available: http://www.emagtech.com

[64] E. B. Joy, W. Leach Jr, G. Rodrigue, and D. T. Paris, "Applications of probe-compensated near-field measurements." *IEEE Trans. Antennas Propag*., vol. 26, no. 3, pp. 379-389, Jul. 1978.

[65] J. Shi, M. Cracraft, K. P. Slattery, M. Yamaguchi, and R. E. DuBroff, "Calibration and compensation of near-field scan measurements," *IEEE Trans. Electromagn. Compat*. , vol. 47, no. 3, pp. 642-650, Aug. 2005.

[66] M. S. Narasimhan and S. Ravishankar, "Probe Uncompensated Near-Field to Far-Field Transformation for Scanning Over an Arbitrary Surface," *IEEE Trans. Antennas Propag*., vol. 33, no. 4, pp. 467-472, Apr. 1985.

[67] A. Taaghol and T. K. Sarkar, "Near-Field to Near/Far-Field Transformation for Arbitrary Near-Field Geometry, Utilizing an Equivalent Magnetic Approach," *IEEE Trans. Electromagn. Compat*., vol. 38, no. 3, pp. 536-542, Aug. 1996.

[68] A. Capozzoli, C. Curcio, G. D'Elia, A. Liseno, P. Vinetti, M. Ameya, M. Hirose, S. Kurokawa, and K. Komiyama, "Dielectric Field Probes for Very-Near-Field and Compact-Near-Field Antenna Characterization," *IEEE Antennas Propag. Mag*., vol. 51, no. 5, pp. 118-125, Oct. 2009.

[69] T. Pfeifer, T. Loffler, H. G. Roskos, H. Kurz, M. Singer, and E. M. Biebl, "Electro-Optic Near-Field Mapping of Planar Resonators," *IEEE Trans. Antennas. Propag*., vol. 46, no. 2, pp. 284-291, Feb. 1998.

[70] D. Lee, N. Kang, J. Choi, J. Kim, and J. F. Whitaker, "Recent Advances in the Design of Electro-optic Sensors for Minimally Destructive Microwave Field Probing," *Sensors*, vol. 11, no. 1, pp. 806-824, Jan. 2011.

[71] F. L. Pedrotti and L. S. Pedrotti, Introduction to Optics. Prentice Hall, New Jersey, 1993.

[72] R. F. Harrington, Time-harmonic electromagnetic fields. Wiley-IEEE Press, New York,

2001.

[73] A. D. Yaghjian, "An overview of near-field antenna measurements," *IEEE Trans. Antennas Propag.*, vol. 34, no.1, pp. 30-45, Jan. 1986.

[74] V. H. Rumsey, "Reaction concept in electromagnetic theory," *Phys. Rev.*, vol. 94, no. 6, pp. 1483-1491, Jun. 1954.

[75] S.C. Chapra, and R.P. Canale, Numerical Methods for Engineers. McGraw-Hill, New York, 2012.

[76] D. J. Lee, J. Y. Kwon, N. W. Kang, J. F. Whitaker, "Calibrated 100-dB-dynamic-range electro-optic probe for high-power microwave applications," *Optics express*, vol. 19, no. 15, pp. 14437-14450, Jul. 2011.

[77] M. L. Crawford, "Generation of standard EM fields using TEM transmission cells," IEEE Trans. Electromagn. Compat., vol. 16, no. 4, pp. 189-195, Nov. 1974.

[78] Instruments for Industry [Online]. Available: http://www.ifi.com/images/stories/pdfs/TEM_Cells_IFI_CC_series.pdf.

[79] A. V. Oppenheim, and R. W. Schafer, Digital signal processing. Prentice Hall, Englewood Cliffs, New Jersey, 1975.

[80] "ZigBee Alliance." [Online], Available: http://www.zigbee.org/

[81] J. Blumenthal, R. Grossmann, F. Golatowski, and D. Timmermann, "Weight Centroid Localization in Zigbee-based Sensor Networks," IEEE Int. Symp. on Intell. Signal Process. (WISP '07), Oct, pp. 1-6.

[82] "Digi International." [Online], Available: http://ftp1.digi.com/support/documentation/90001020_F.pdf.

[83] "Fox Electronics." [Online], Available: http://www.foxonline.com/pdfs/FVXO_PC53.pdf.

[84] D. M. Pozar, Microwave and RF design of wireless systems. John Wiley & Sons, Inc., 2000.

[85] R. Gilmore and L. Besser. Practical RF circuit design for modern wireless systems. Vol. 2. Artech House, 2003.

[86] S. Lim, R. L. Rogers, and H. Ling, "A tunable electrically small antenna for ground wave transmission," *IEEE Trans. Antennas Propag.*, vol. 54, no. 2, pp. 417-421, Feb. 2006.

[87] X-CTU: Next generation configuration platform for XBee, Digi International Inc. [Online],

Available: http://www.digi.com/products/xbee-rf-solutions/xctu-software/xctu.

[88] A. Goldsmith, Wireless Communications. Cambridge University Press, 2005.

[89] M Vroubel, Y Zhuang, B Rejaei, J. N. Burghartz, "Integrated Tunable Magnetic RF Inductor," *IEEE Electron Device Letters*, vol. 25, no. 12, pp. 782-789, Dec. 2004.

[90] W. K. Kuo, W. H. Chen, Y. T. Huang, S. L. Huang, "Two-Dimensional Electric-Field Vector Measurement by a$LiTaO_3$ Electro-Optic Probe Tip," *Applied Optics*, vol. 39, no. 27, pp. 4985-4993, Sep. 2000.

[91] G. Verma, F. Dagefu, B. M. Sadler, K. Sarabandi, "Direction of Arrival Estimation with the Received Signal Strength Gradient at the Lower VHF Band," *Antennas and Propagation (APS/URSI), 2016 IEEE International Symposium*, pp. 1695-1696, Jun. 2016.